

Electronic Theses and Dissertations, 2004-2019

2012

Fire Retardant Polymer Nanocomposites: Materials Design And Thermal Degradation Modeling

Jinfeng Zhuge
University of Central Florida

 Part of the [Mechanical Engineering Commons](#)
Find similar works at: <https://stars.library.ucf.edu/etd>
University of Central Florida Libraries <http://library.ucf.edu>

This Doctoral Dissertation (Open Access) is brought to you for free and open access by STARS. It has been accepted for inclusion in Electronic Theses and Dissertations, 2004-2019 by an authorized administrator of STARS. For more information, please contact STARS@ucf.edu.

STARS Citation

Zhuge, Jinfeng, "Fire Retardant Polymer Nanocomposites: Materials Design And Thermal Degradation Modeling" (2012). *Electronic Theses and Dissertations, 2004-2019*. 2174.
<https://stars.library.ucf.edu/etd/2174>

FIRE RETARDANT NANOCOMPOSITES: MATERIALS DESIGN AND THERMAL DEGRADATION MODELING

by

JINFENG ZHUGE

B.S. Northwestern Polytechnical University, 2008

M.S. University of Central Florida, 2010

A dissertation submitted in partial fulfillment of the requirements
for the degree of Doctor of Philosophy
in the Department of Mechanical, Materials, and Aerospace Engineering
in the College of Engineering and Computer Sciences
at the University of Central Florida
Orlando, Florida

Spring Term
2012

Major Professor: Jihua Gou

©2012 Jinfeng Zhuge

ABSTRACT

Compared to conventional materials, polymer matrix composites (PMCs) have a number of attractive properties, including light weight, easiness of installation, potential to lower system-level cost, high overall durability, and less susceptibility to environmental deterioration. However, PMCs are vulnerable to fire such that they degrade, decompose, and sometimes yield toxic gases at high temperature. The degradation and decomposition of composites lead to loss in mass, resulting in loss in mechanical strength.

This research aims to improve the structural integrity of the PMCs under fire conditions by designing and optimizing a fire retardant nanopaper coating, and to fundamentally understand the thermal response and post-fire mechanical behavior the PMCs through numerical modeling. Specifically, a novel paper-making process that combined carbon nanofiber, nanoclay, exfoliated graphite nanoplatelet, and ammonium polyphosphate into a self-standing nanopaper was developed. The nanopaper was then coated onto the surface of the PMCs to improve the fire retardant performance of the material. The morphology, thermal stability, flammability, and post-fire flexural modulus of the nanopaper coated-PMCs were characterized. The fire retardant mechanism of the nanopaper coating was studied.

Upon successfully improving the structure integrity of the PMCs by the nanopaper coatings, a thermal degradation model that captured the decomposition reaction of the

polymer matrix with a second kind boundary condition (constant heat flux) was solved using Finite Element (FE) method. The weak form of the model was constructed by the weighted residual method. The model quantified the thermal and post-fire flexural responses of the composites subject to continuously applied heat fluxes. A temperature dependent post-fire residual modulus was assigned to each element in the FE domain. The bulk residual modulus was computed by assembling the modulus of each element. Based on the FE model, a refined Finite Difference (FD) model was developed to predict the fire response of the PMCs coated with the nanopapers. The FD model adopted the same post-fire mechanical evaluation method. However, unlike the FE model, the flow of the decomposed gas, and permeability and porosity of the composites were taken into account in the refined FD model. The numerical analysis indicated that the thickness and porosity of the composites had a profound impact on the thermal response of the composites.

The research funding from the Office of Naval Research (ONR) and Federal Aviation Administration Center of Excellence for Commercial Space Transportation (FAA COE AST) is acknowledged.

To my family

ACKNOWLEDGMENTS

Dr. Jihua Gou, the director of the Composite Materials and Structures Laboratory (CMSL) at UCF and my research advisor, provided me this great opportunity to access the world of nanocomposite materials. I am grateful for his guidance and support. I had received many insightful comments and suggestions from the other professors on my dissertation committee, Dr. Ruey-Hung Chen, Dr. Jayanta Kapat, and Dr. Lei Zhai. My special thanks to Dr. Chen, who is not only a thoughtful and erudite instructor, but also an honest and pleasant friend. I enjoyed many discussions with him. Dr. Yong Tang, the postdoc at CMSL from 2008 to 2011, is an indispensable friend. He helped me, a college graduate without any sense of scientific research, start my research career. My appreciation also extends to Dr. Yuanli Bai, my Finite Element instructor, and Dr. Alain Kassab, my Applied Math and Conduction Heat Transfer instructor. Without them, the modeling part of this dissertation could have been impossible. I admire their profound knowledge and passion in mathematics and numerical analysis. Mr. James McKee, the lab manager and research assistant at CMSL, has an enthusiasm for scientific research. In addition to taking care of the experimental issues I had encountered, he helped me check the language of my every journal paper, and I appreciate his support. Mr. Jeremy Lawrence, an undergraduate research assistant at CMSL, Mr. Dustin Hart, a research assistant at Pittsburg State University, Mr. Ziqing Yu and Mr. Chunlin Liu, research assistants at the University of North Carolina at Charlotte had helped me a great deal

with my experiments. I am also grateful for Mr. Peter Denis III, Mr. Robert Lovelady, and many other advisors at the Writing Center of UCF, assisting me in the dissertation writings. No matter how often this dissertation is revised, there are flaws and mistakes, and those are my fault.

Above all, I would like to thank my beloved Jing, for being there, always supportive, gentle, and kind; my wonderful parents, Zhenhua Zhuge and Gennü Hong, my wise and dependable uncle and aunt, Ronghua Zhuge and Yi Chen, for their endless patience and countless acts of support for my study and life in the USA. To them I humbly dedicate this work.

TABLE OF CONTENTS

LIST OF FIGURES	xii
LIST OF TABLES	xviii
CHAPTER 1 INTRODUCTION	1
1.1. Motivation.....	1
1.2. Research Methods	2
1.2.1. Phenomenon of combustion and flame retardancy strategy	2
1.2.2. Objectives	5
1.3. Structure of the Dissertation	8
CHAPTER 2 LITERATURE REVIEW.....	10
2.1. Fire Retardant Nanocomposites	10
2.1.1. Processing of polymer nanocomposites.....	11
2.1.2. Flammability and safety evaluations	23
2.1.3. Overview of the research in fire retardant nanocomposites.....	26
2.1.4. Intumescent fire retardant coating	36
2.2. Numerical Modeling of PMCs Subject to Heat Flux.....	39
CHAPTER 3 SYNTHESIS AND PROCESSING OF NANOCOMPOSITES AND HYBRID NANOPAPER.....	44
3.1. Processing of Hybrid Nanopaper	44

3.2. Processing of Nanocomposites Coated with Nanopapers.....	48
CHAPTER 4 FIRE RETARDANT PERFORMANCE EVALUATION OF THE NANOCOMPOSITES	53
4.1. Introduction.....	53
4.2. Fire Retardant Performance Evaluation of the xGnP/APP Nanocomposites	55
4.2.1. Results and discussion	60
4.2.2. Conclusions.....	75
4.3. Fire Retardant Performance Evaluation of the Glass Fiber Reinforced Polyester Coated with the xGnP/CNF/APP and Nanoclay/CNF/APP Nanopaper	76
4.3.1. Results and Discussion	80
4.3.2. Conclusions.....	95
4.4. Fire Retardant Performance Evaluation of the Glass Fiber Reinforced Polyester Coated with the xGnP/CNF/APP Nanopaper Subject to Various Heat Fluxes.....	96
4.4.1. Results and discussion	99
4.4.2. Flame retardancy mechanism	116
4.4.3. Conclusions.....	118
CHAPTER 5 FINITE ELEMENT MODELING OF THERMAL RESPONSE AND POST-FIRE FLEXURAL DEGRADATION OF GLASS FIBER REINFORCED POLYESTER	120
5.1. Introduction.....	120

7.2.1. Improving the expansion rate of hybrid nanopaper	171
7.2.2. Optimizing the heat transfer property of hybrid nanopaper.....	173
7.3. Thermo-mechanical Degradation Model Improvement.....	176
7.3.1. Improving the accuracy of the input material parameters	176
7.3.2. Refining the thermal response model	178
REFERENCES	179

LIST OF FIGURES

Figure 1 Schematic of the solution processing.	11
Figure 2 Structural variations of the clay/polymer composites.	14
Figure 3 Schematic of the in-situ polymerization process.....	16
Figure 4 Schematic of the melting processing.....	18
Figure 5 The schematic representation of the ASTM E1345-10 cone calorimeter test method (left, source from internet) and the vertical orientation exploded view of the apparatus (right, source from ASTM E1345-10).	24
Figure 6 High pressure filtration system.....	46
Figure 7 Vacuum assisted filtration system.	47
Figure 8 SEM image of a hybrid nanopaper.	48
Figure 9 Final appearance of the nanopapers before the RTM process.	49
Figure 10 Compressed air VARTM system.	50
Figure 11 High pressure VARTM system.	51
Figure 12 Heat release rate of the samples with different weight ratios of APP and xGnP.	60
Figure 13 Air bubbles that had been trapped in the char structure of the xGnP-APP-17-laminates after the cone calorimeter test.	61
Figure 14 The presence of the xGnP nanoparticles inhibits the diffusion of the	

decomposed gases.....	62
Figure 15 Mass loss rate of the samples.	63
Figure 16 Heat release rate of the samples coated with the xGnP/CNF hybrid nanopapers. (a) 0~800s; (b) 0~100s.....	65
Figure 17 Heat release rate between 100s~350s.....	66
Figure 18 Smoke production rate of the samples coated with the nanopapers. (a)0~700s; (b)0~350s.....	67
Figure 19 Mass percentage of the remaining matrices during the cone calorimeter tests. (a) mixing samples; (b) paper coated samples.....	70
Figure 20 XRD results of the samples with different concentrations of APP and xGnP.	71
Figure 21 SEM images of the hybrid nanopapers. (a) C1G3; (b) C3G1; (c) C0G1; (d) C1G0.....	73
Figure 22 Char SEM image of the samples C1G3-GA-L and C0G1-GA-L.....	74
Figure 23 Char SEM image of the sample C1G0-GA-L.	75
Figure 24 Experimental setup of a composites sample for the three-point bending test.	79
Figure 25 Heat release rate of the samples.	81
Figure 26 (a) The built-up pressure beneath a nanopaper results in the delamination and (b) the mechanism of permeability-related ignition (arrows indicate the decomposed fuel).....	82
Figure 27 Flame patterns on the surfaces of the samples immediately after ignition. (a)	

control sample and (b) nanopaper-coated sample.....	83
Figure 28 Char materials after the cone calorimeter test (first layer is more close to the heat flux than successive layers). (a) control sample; (b) CXA sample; and (c) CCA sample.	85
Figure 29 Mass loss rate of the samples.	85
Figure 30 Remaining mass of the samples during the cone calorimeter test.....	86
Figure 31 TGA results of the samples.....	87
Figure 32 Residual elastic modulus of the samples with different exposure times.	89
Figure 33 Comparison of the self weight-sustaining ability.	90
Figure 34 Hybrid nanopapers. (a) morphology of nanofibers; (b) nanoparticles within the nanofiber networks; (c) CNF/Clay/APP hybrid nanopaper; (d) CNF/Clay/xGnP hybrid nanopaper.....	91
Figure 35 Morphologies of different types of char. (a) top surface char structure of all samples; (b) back surface char structure of both types of nanopapers; (c) and (d) back surface char structure of CCA nanopaper.....	92
Figure 36 Morphologies of the glass fibers of the samples coated with hybrid nanopapers. (a) 2 μ m, (b) 200nm.....	93
Figure 37 Morphologies of the resin. (a) back of the sample with the exposure time of 150s and scale bar of 200 μ m; (b) back of the sample with the exposure time of 150s and scale bar of 200nm; (c) virgin resin with the scale bar of 200nm; (d) front	

surface of the control sample with an ignition time of less than 5s.....	94
Figure 38 (a) Temperature measurement setup and (b) actual samples.....	98
Figure 39 Heat release rate curves of the control samples subjected to various heat fluxes.	99
Figure 40 Residues of the control samples after the cone calorimeter test.....	101
Figure 41 Heat release rate curves of the paper-coated samples subjected to various heat fluxes.....	101
Figure 42 (a) Heat release rate and (b) mass loss rate of the two groups of samples subjected to low heat flux (25kw/m ²).	103
Figure 43 (a) Heat release rate and (b) mass loss rate of the two groups of samples subjected to high heat flux (100kw/m ²).	103
Figure 44 Mass remains of the samples during the cone calorimeter test.	106
Figure 45 Temperature profiles of the samples subjected to various heat fluxes. (a) 25kw/m ² ; (b) 35kw/m ² ; (c) 50kw/m ² ; (d) 75kw/m ² ; (e) 100kw/m ²	109
Figure 46 (a) Morphologies of the dry nanopaper and (b) the paper structure after resin transfer molding.....	113
Figure 47 Morphologies of the residues of the samples that had been exposed to 100kw/m ² heat flux.....	114
Figure 48 Char materials on the back surface of the hybrid nanopaper.....	115
Figure 49 Char materials attached to the glass fibers of the control sample.	115

Figure 50 Flame retardancy mechanism.	116
Figure 51 Residues of the composites after cone calorimeter tests.	124
Figure 52 Geometric discretization of the solution domain.....	126
Figure 53 Computational algorithm of the FE model.....	133
Figure 54 TGA data of the composites with curve fitting.....	136
Figure 55 Temperature at different locations for different exposure times.....	137
Figure 56 3-D plot of the thermal degradation model with applied heat flux of 50kW/m ²	138
Figure 57 Convergence study. (a) mass loss rate; (b) mass loss rate with different discretizations (75kW/m ²); (c) back side temperature with different discretizations (75kW/m ²); (d) remaining mass with different discretizations (75kW/m ²).....	139
Figure 58 Comparison of experimentally measured temperatures with numerical predictions.....	140
Figure 59 Comparison of experimentally measured ratio of remaining mass with numerical predictions.....	142
Figure 60 Remaining glass fiber mats after the sample was exposed to 100kW/m ² heat flux (the surface layer is in the most left).	143
Figure 61 Model verification by normalized residual flexural moduli.....	144
Figure 62 Material design. (a) model predictions of temperatures; (b) model predictions of residual moduli.	145

Figure 63 Schematic of the energy and mass flow within a finite volume of the composites.....	149
Figure 64 Computational algorithm of the FD model.	154
Figure 65 Fourth Order polynomial fitting of the surface boundary conditions.....	157
Figure 66 Convergence study of the FD model. (a) cold side temperature prediction; (b) remaining mass prediction.	159
Figure 67 Model results. (a) 3-D Temperature profile as a function of thickness and exposure time; (b) temperature evolution as a function of thickness; (c) porosity evolution as a function of exposure time.	160
Figure 68 Comparison of experimentally measured ratio of remaining mass with numerical predictions.....	161
Figure 69 Comparison of experimentally measured temperature with numerical predictions.....	163
Figure 70 Comparison of experimentally measured flexural moduli with numerical predictions.....	165
Figure 71 Model results of solid phase density.....	166
Figure 72 Model results of mass flux rate.	167
Figure 73 Impact of the input parameters on the residual moduli predictions.	168

LIST OF TABLES

Table 1 Properties of typical solvents.	12
Table 2 Composition of the xGnP-based nanocomposites.	57
Table 3 Composition of the hybrid nanopapers and nanocomposites.....	58
Table 4 Summary of cone calorimeter test results of the mixing group.	64
Table 5 Summary of cone calorimeter test results of the paper-coated group.	68
Table 6 Composition of the hybrid nanopapers and nanocomposites.....	77
Table 7 Summary of cone calorimeter test results.	80
Table 8 Summary of thermal stability of the samples.....	88
Table 9 Composition of the hybrid nanopapers and nanocomposites.....	97
Table 10 Heat treatment for the post-fire three-point bending test.	97
Table 11 Summary of cone calorimeter test results for the control samples.	100
Table 12 Summary of cone calorimeter test results for the 3xGnP/1CNF/9APP samples.	104
Table 13 Time (seconds) to reach the critical temperatures for the samples.	110
Table 14 Normalized flexural moduli of the samples subjected to various heat fluxes with different exposure times.....	112
Table 15 Input parameters of the materials.....	134
Table 16 Input parameters of the materials.....	156

Table 17 Curve fitting parameters of the surface boundary conditions.158

CHAPTER 1

INTRODUCTION

1.1. Motivation

Polymer-matrix composites (PMCs) are composed of high strength fibers and polymer matrix. Within the PMCs structure, both the fibers and matrix retain their individual properties. Yet, the combination shows a unique property that cannot be achieved with either of the fibers or matrix acting alone. In the resulting PMCs, the matrix works as a medium that keeps the fibers in a desirable direction and location. The fibers serve as the principal load-carrying members. The matrix transfers applied force between the fibers and also protects the fibers from environmental damages such as humidity and chemical corrosion [1]. Compared to metallic materials, the weight of a component that is made of PMCs materials could be substantially reduced due to their high specific strength (σ_{ult}/ρ) and high specific stiffness (E/ρ).

Because of these unique mechanical advantages, PMCs materials are considered to replace traditional metallic materials and are commonly applied in aircraft, military, space, automotive, sporting goods, marine, infrastructure, and biomedical sectors. For example, the materials used in the body of a Boeing 777 aircraft are 50 percent aluminum and 12 percent composites by weight, while in the newly developed Boeing 787 Dreamliner, the percentages by weight for aluminum and composite materials have changed to 20 percent and 50 percent, respectively [2]. According to a commercial report, the worldwide annual composites market

grows at a rate of 4 percent, from about \$80 billion USD in 2008 to almost \$110 billion in 2013. Globally, the market shared by the so-called BRIC (Brazil, Russia, India and China) is expected to grow from around 22 percent 2008 to 29 percent in 2013, with China alone representing 23 percent of the worldwide market that year. The major contribution to the growth comes from wind energy market, aerospace sectors, and building, construction, automotive industries (especially in China) [3].

However, one shortcoming for PMCs materials that limits their implementation is their vulnerability to fire. Resulting from their organic nature, PMCs will degrade, decompose, and sometimes yield toxic gases when subject to radiant heat or fire. The degradation and decomposition of composites will lead to losses in mass: that leads to losses in mechanical strength of the structure. It is possible that the application of PMCs has contributed to the more than \$12 billion in property loss and 3000 deaths in fire during 2009 [4]. *Therefore, the motivation of this study is to understand the fire response of polymer composites both experimentally and mathematically, and eventually to improve the flame resistance and structural integrity of the material by optimizing the material design.*

1.2. Research Methods

1.2.1. Phenomenon of combustion and flame retardancy strategy

In order to design effective flame retardant systems, it is imperative to understand the process of combustion reactions, or more specifically, the burning process of polymer. Generally speaking, there are two kinds of flames: premixed flame where gas and fuel source

are kept constant, such as that produce by an oxygen acetylene torch, and diffusion flame, where the oxygen diffuses into the fuel mixture from the surrounding atmosphere, such as the burning of PMCs [5]. During the evolving of the diffusion flame, which is the combustion phenomenon that will be discussed throughout this dissertation, three steps will be occurring in the following order: the heating of the fuel source, the decomposition of the fuel source into combustible and non-combustible materials, and finally the ignition of the combustible fuel and air mixture to produce a flame [6]. The decomposition of the polymer matrix (fuel source) essentially is the breaking of chemical bonds, transforming the fuel into high energy free radicals. This process is initiated by an external heat source. As long as the combustion process has begun and the fuel/air mixture remains at a certain level, the heat generated by exothermic combustion of the fuel is enough to keep the flame propagating. The mass transfer of the fuel/air mixture into the pyrolysis zone and energy transfer back to the fuel source are crucial to sustain the combustion process, during which the oxygen, heating rate, and pressure of environment are playing significant roles [6-8].

Once the combustion process is understood, it is possible to design the strategies to stop the propagation of fire. When polymer is under external heat flux, the material can decompose, to form the high energy free radicals and evaporate. If the concentration of volatile products is sufficient (within the flammability limits and the temperature is above the ignition temperature), the combustion proceeds [9]. Accordingly, one can extinguish the fire chemically and physically in both the vapor phase and condensed phase by reducing the heat

or fuel below critical levels [10]. In the condensed phase, there are two approaches to stop the combustion cycle. Firstly, one can dilute the solid fuel with inorganic fillers (*e.g.* talc or calcium carbonate), lowering the combustible portion of the material, and ultimately lowering the amount of heat per volume of material it can produce while burning. Alternatively, there are additives that would create an endothermic environment when reacting, such as magnesium and aluminum hydroxides, as well as various hydrates such as hydromagnesite. Secondly, one can carbonize the polymer, during the decomposition process to form foaming char (*e.g.* intumescent additives), which acts as a protective layer from both mass and heat transfer. In the vapor phase, the combustion cycle can be stopped by physically diluting the flame with inert gases (such as carbon dioxide and water), which are the result of the thermal degradation of the flame retardants, or by chemically removing fire-propagating radicals such as $H\cdot$ and $OH\cdot$ with halogenated gases (*e.g.* hydrogen chloride and hydrogen bromide) [6]. These chemicals can be permanently bonded into the polymer molecules to form intrinsically fire-resistant polymers, or added into the polymer as fire-retardant fillers.

Even though halogenated fire retardants are effective, they will be abandoned sooner or later because of the growing environmental and health concerns [11-14]. The intrinsic flame resistant polymers, however, are so expensive that it is difficult to extend their applications unless break-through technologies appeared that dramatically reduced the cost of synthesizing this type of polymer. Other flame retardants, such as intumescent flame retardants, aluminum trihydrate (ATH), and magnesium hydroxide have their own

shortcomings: their expensive price and the high loading requirement in order to pass fire safety tests, which causes problems such as high density, lack of flexibility, low mechanical properties, and difficulty in processing [15]. The endeavor of seeking an effective flame retardant system in this dissertation is focused on nanomaterials and coating technologies. This is because the large aspect ratio of nanomaterials could provide desirable features to lower the loading of additives. The coating technology could potentially eliminate the difficulty of obtaining PMCs with the flame retardants homogeneously dispersed in their matrices.

1.2.2. Objectives

Many researchers had reported that a high quality and compact carbonaceous protective char layer being formed under fire condition when the nanocomposites showed excellent flame resistance. The pioneering research had done by Kashiwagi *et al* have inspired a promising idea to achieve fire retardancy [19-23]. That is: instead of forming the char layer gradually during the combustion process, why not impose a pre-existing char layer directly onto the surface of PMCs! Therefore, one of the objectives of this work is to enhance the flame resistance of PMCs by seeking an effective yet practical coating system, or the “pre-existing protective char layer”, which is expected to serve as a mass and heat barrier for PMCs under fire scenario. First of all, the thermal stability of such a “char” should be high as it will experience the highest temperature, which automatically leads one to seek carbon-based material. Initially, carbon nanotube (CNT) was used to fabricate buckypaper.

Although it was possible to make a self-standing CNT paper without adding additional bonding agent or blender (because the bonding agent or blender might decrease the thermal stability of the nanopaper), the as-made buckypaper was extremely brittle as the short CNTs were hardly entangled with each other. This, unfortunately, resulted in the difficulty of further processing. Carbon nanofiber (CNF), on the other hand, does not exhibit such a shortcoming. Since CNFs can tangle with each other tightly, it is relatively easy to fabricate a CNF paper with high processability. Moreover, the cost of CNF is much lower than that of CNT, yet sometimes possesses similar physical properties. As a result, CNF is the ideal choice to form the scaffold for such a pre-existing “char layer”. Secondly, it is difficult to achieve flame resistance by coating the pure CNF paper onto the surface of composite materials. In fact, Zhao *et al* reported that when using pure CNF paper alone, the flammability of PMCs was increased instead of decreased. The PHRR of the sample was increased and the time to ignition was shortened. In other words, the sample coated with pure CNF paper ended up not only easy to catch fire but also releasing a large amount of heat, which could provide the heat source for the sustainable combustion. In such a case, the CNF paper was not a “fire retardant”, but only a “fire catalyst”. Therefore, as a second step, it is important to modify the CNF nanopaper by incorporating other types of particles so that a synergistic effect between nanofiber and other particles should be revealed. These types of nanopapers are called the “hybrid nanopapers”.

When hybrid nanopaper is coated onto the surface of composite laminates, the

polymer matrix serves as the medium to tightly hold those nanoparticles together. For example, when designing the clay-CNF hybrid paper, multiple effects could be expected. The CNF scaffolding should hold the clay particles, which are very promising fire retardants. The well-dispersed clay in the polymer matrix will increase the viscosity of the polymer, which is important to form compact char during the combustion process. Furthermore, the planar structure of clay compensates for the relatively high permeability of the CNF paper: the permeability should play a significant role in preventing the mass flow of fuels originating from the decomposition of resin. Consequently, the conditions for sustainable flame propagation will be disturbed and fire resistance should be achieved.

As a rule of thumb, desirable char layer that could able to protect the underlying structure should simultaneously possess the following characteristics: low thermal conductivity in thickness direction (to prevent heat transfer), high in-planar thermal conductivity (to dissipate heat as soon as possible), high stability, low heat absorption, high heat capacity, and a compact structure to prevent mass loss.

The second objective of this work is to fundamentally understand the fire response and post-fire mechanical behavior of the polymer composites by means of numerical modeling. First, a classic PMCs thermal degradation model with a second kind boundary condition (constant heat flux) will be solved using the Finite Element Method (FEM), with the weak form being constructed by the weighted residue method (or, more specifically, Galerkin's method). The predicted results should include the temperature and density profile

of the material at different locations and times, as well as the mass loss rate. Then a temperature dependent post-fire residual modulus will be assigned to each element within the FE Model. The bulk residual moduli will be calculated by assembling the modulus of each element. Base on the FE model, a refined Finite Difference (FD) model will be developed. This model is expected to predict the fire response of the composites coated with nanopaper. The FD model will adopt the same post-fire mechanical evaluation method. However, unlike the previous one, the permeability and porosity of the composites will be taken into account.

1.3. Structure of the Dissertation

The main body of the dissertation from Chapter 2 to Chapter 6 is organized by the following sequence. Chapter 2 reviews the typical nanocomposites processing approaches, and the research and development of the application of various shapes of nanoparticles as fire retardants. The topic of intumescent coatings is also discussed in the chapter. In Chapter 3, the discussion focuses on the processing of nanocomposites, namely, how to fabricate hybrid nanopapers with homemade equipment and how to manufacture PMCs coated with nanopapers by means of the Resin Transfer Molding (RTM) process. The reduction in flammability of PMCs by means of directly mixing nanoparticles with the polymer matrix and by fabricating nanoparticles into hybrid nanopaper coatings are compared and discussed in Chapter 4. Specifically, different types of nanoparticles are used to fabricate nanopapers under different weight ratios. The optimized hybrid system is selected as a result of the

comparison between these nanopapers in terms of flame retardancy and bonding with the underlying structure. Further discussions on temperature profiles and post-fire flexural degradation are carried out to estimate the effectiveness of the nanopaper protection. Chapters 5 and 6 are focused on the computational modeling of the thermal degradation of the composite laminates with/without nanopaper coating. Two numerical models have been developed in these chapters. Chapter 5 focuses on the thermo-mechanical study of the PMCs where no nanopaper coatings are applied, while the Chapter 6 discusses the fire response of the PMCs coating with nanopapers. In addition, based on the numerical analysis, the impact of different material parameters on the thermal and post-fire flexural response of the composite structure are compared and evaluated. The results could provide important information for future material design. The dissertation ends in Chapter 7, where future improvement in material design and model development are proposed.

CHAPTER 2 LITERATURE REVIEW

2.1. Fire Retardant Nanocomposites

It is widely acknowledged that nanotechnology deals with structures sized between 1 to 100 nanometer in at least one dimension. Nanocomposites can be made from a wide variety of starting materials such as gases, metals and minerals, giving a range of enhanced properties, including electrical conductivity, superparamagnetism, and fire retardancy [16]. The geometry of nanoparticles that been mixed with polymers to improve their fire resistance can be lamella structure: clays, graphite, layered double hydroxides (LDHs) to list a few examples; or two-dimensional linear structure such as carbon nanotubes and carbon nanofibers; or three dimensional structure such as polyhedral oligomeric silsesquioxane (POSS). Many scientists and groups have done pioneering work regarding to fire retarded nanocomposites such as Takashi Kashiwagi, Charles A. Wilkie, Jeffrey W. Gilman, NIST, Cornell University, *etc.* Various types of nanoparticles, such as nanoclay, TiO₂, silica, layered double hydroxides (LDH), carbon nanotubes (CNT), and polyhedral silsesquioxanes (POSS), have been investigated and showed promising flame retardant effect, as even very small amount is mixed into polymer [17]. Many companies, including Nanocor and Albemarle Corporation, have already transferred the laboratorial achievements into real life application: nanoclay-based flame retardants have been used in electronics, wires, cables, and decorative wall papers [18].

2.1.1. Processing of polymer nanocomposites

Nanoparticles have been incorporated into polymers to develop high quality nanocomposites with unique properties. Although the techniques are inherently different, all of them are trying to address the fundamental issues: incorporating nanoparticles into the polymer matrix in a homogenous dispersion manner. Common approaches include: (a) Solution Processing; (b) In-situ Polymerization; (c) Melting mixing.

(a) Solution processing

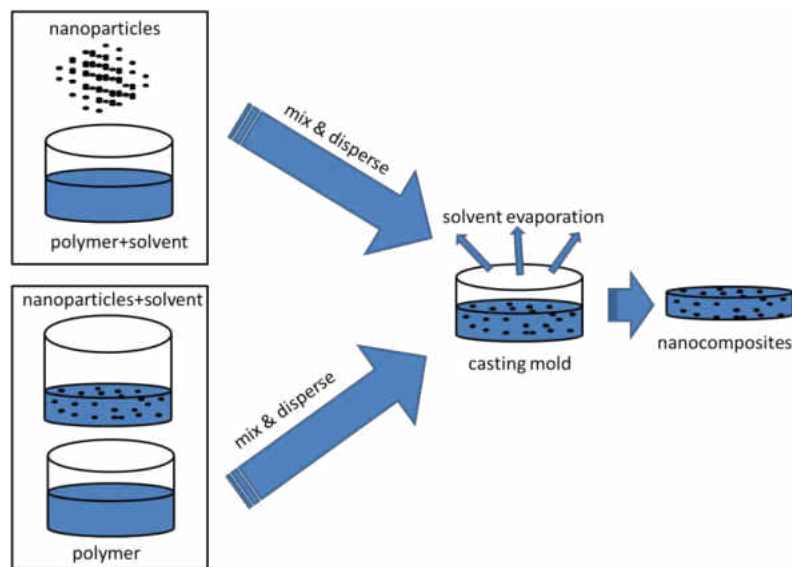


Figure 1 Schematic of the solution processing.

Figure 1 shows the sketch of the solution processing. Nanoparticles are first dispersed in a solvent or polymer solution. The nanoparticle/polymer/solvent solution is mixed by energetic agitation such as magnetic stirring, high shear mixing, reflux, or sonication. For the sonication process, there are two types of equipment: high-power sonication that uses a tip or

horn to disperse particles, and mild sonication during which particles are dispersed in a water bath. It is important to note that carbon nanotubes cannot be dispersed well in most of the solvents due to their exceptionally high aspect ratios. The quality of the dispersion can be improved by treating the nanoparticles with surfactants, such as the derivatives of sodium dodecylsulfate [24]. After the nanoparticles are homogeneously dispersed, the solution is poured into a mold and the solvent is allowed to evaporate, leaving a composite film or sheet upon the completion of the evaporation [25].

The solution processing is the most commonly used method to prepare the nanocomposites with a film or sheet like structure. The choice of solvent is made based on the solubility of polymer matrices. Table 1 shows the properties of different types of solvents.

Table 1 Properties of typical solvents.

Solvent	Boiling Point(°C)	Dielectric Constant	Density(g/ml)
Non-polar solvents			
Pentane	36	1.84	0.626
Toluene	111	2.38	0.867
Benzene	80	2.3	0.879
Polar aprotic solvents			
Acetone	56	21	0.786
Dimethylformamide	153	38	0.944
Dichloromethane	40	9.1	1.3266
Polar protic solvent			
Water	100	80	1
Methanol	65	33	0.791
Ethanol	79	24.55	0.789

One of the successful experiments to disperse high concentration of multi-walled carbon nanotubes (MWCNT) into polymer by solution processing was achieved by Jin *et al*

[26]. In their study, MWCNT produced by arc discharge were dispersed in chloroform by sonication. The polymer matrix, polyhydroxyaminoether (PHAE), was dissolved into the MWCNT-chloroform solution during sonication process. The well-dispersed suspension was poured into a Teflon mold and allowed to dry overnight in a fume-hood. The solution processing enabled them to prepare the nanocomposites containing 50wt% of MWCNT with a good quality. Another research group compared the quality of dispersion and mechanical properties of the nanocomposites (expanded graphite/epoxy) prepared by different types of processing methods [27]. During the direct mixing, expanded graphite (EG) was dispersed in the hardener of the epoxy by magnetic stirrer at room temperature. The epoxy matrix (DGEBA) was then added into the EG/hardener solution and the mixture was stirred on a hot plate. In addition, an accelerator was added into the mixture and was stirred with slow agitation followed by overnight degassing. The nanocomposite was made by casting the solution into a Teflon mold, being cured at 148°C. During the solution processing, EG was first dispersed into acetone by sonication. The DGEBA epoxy matrix was introduced into the suspension and sonicated. The solution was stirred on a hot plate until acetone was completely evaporated. Then the hardener and accelerator were added, followed by degassing, casting, and curing process. The samples prepared by the two different processes were examined by optical microscopy. The results indicated that the quality of nanocomposites prepared by solution processing was much better than that of the nanocomposites prepared by direct mixing.

The solution processing is extensively used to prepare clay nanocomposites. By using an adequate amount of polymer soluble solvent (or a thermosetting reactive pre-polymer, in the case of insoluble polymers such as polyimide), nanoclays can be dispersed into single layers, due to the fact that the forces that stack the layers together are weak. The polymer matrix is then added into the solution, being absorbed into the gaps between the layered silicates. After the solvent is evaporated or the mixture is precipitated, the layered silicates will sandwich the polymer to form an ordered, multi-layered structure. As a result, two types of structures can be achieved, namely, intercalated and exfoliated (Figure 2).

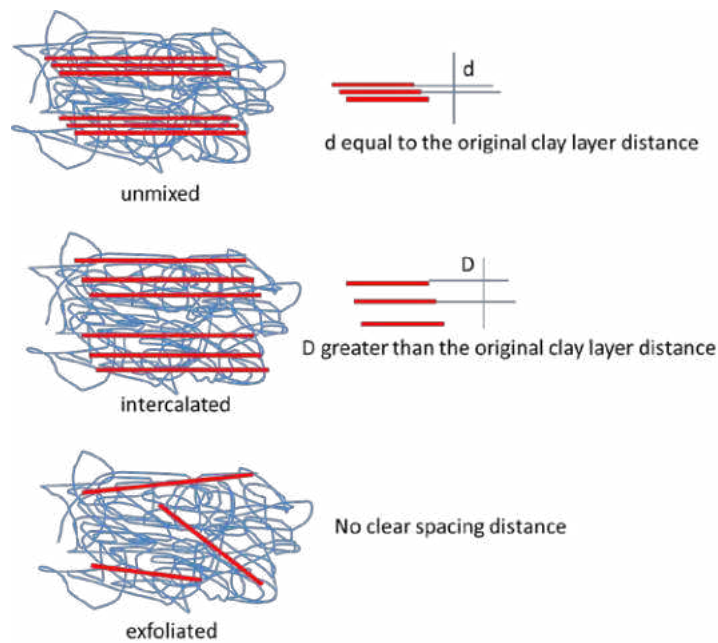


Figure 2 Structural variations of the clay/polymer composites.

The intercalated structure is obtained by self-assembled, well-ordered multilayered structures. Between gallery spaces (2-3nm) of those parallel individual silicate layers,

extended polymer chains are inserted. When the spaces between individual silicates are large enough so that the interactions between gallery cations of the adjacent layers could not be kept any more, exfoliated or delaminated nanocomposites are formed. In this case, the interlayer spacing can be of the order of the gyration radius of the polymer [28]. The unmixed, intercalated, and exfoliated structures can be confirmed by the X-ray diffraction (XRD) analysis. The unmixed structure has the same peak with original nanoparticles. However, the peaks for an intercalated structure appear earlier than original nanoparticles. And there is no peak for an exfoliated structure. Rao and Pochan studied polymer-clay nanocomposites prepared by solution processing. 3wt% of montmorillonite clay (Cloisite Na⁺) was dispersed in water by vigorous mixing and centrifuging [29]. This process was also expected to remove impurities. The colloidal aqueous remained without settlement for several months. Copolymer latex (PBSMaSO₃), which was synthesized by emulsion polymerization, was mixed with the clay aqueous. After the well-dispersed solution was obtained, it was poured into a Teflon cast overlaid by Kapton film and dried at ambient temperature. After the nanocomposite film was formed, it was peeled off and dried in a vacuum oven. The quality of PBSMaSO₃-clay nanocomposite was evaluated by XRD, which suggested that if the loading of nanoclay was less than 4wt%, an exfoliated structure was achieved. However, the increase of clay loading (> 4wt%) could result in an intercalated structure.

(b) In-situ polymerization process

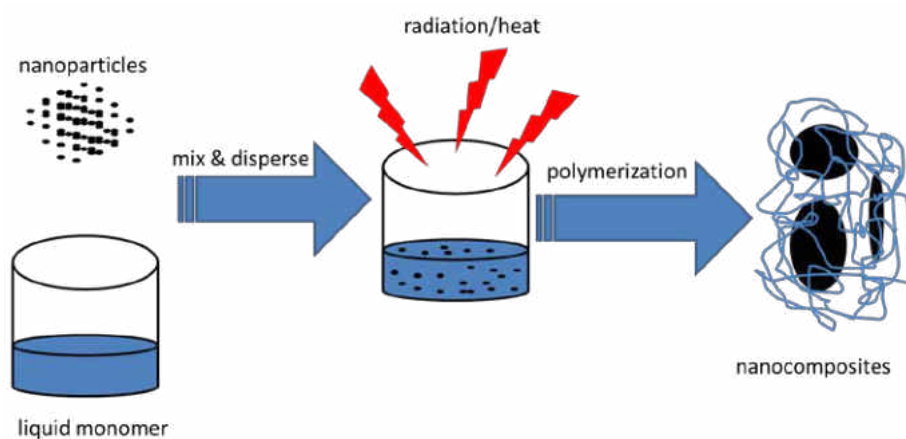


Figure 3 Schematic of the in-situ polymerization process.

Figure 3 schematically shows the in-situ polymerization process. During the in-situ polymerization process, nanoparticles such as CNTs and layered silicates are first dispersed in the liquid monomer. The polymerization reaction is initiated by heat, radiation, the diffusion of a suitable initiator, or by catalyst fixed on the surface of nanoparticles [24]. At the completion of polymerization, polymer molecules are either wrapped around or covalently bonded to nanoparticles depending on the surface functionality of the nanoparticles and the polymer being formed [25].

The in-situ polymerization process can be used to prepare the nanocomposites containing insoluble and thermally unstable polymer, which cannot be processed by solution or melting process. Ring-opening, radical, anionic, and chain transfer metathesis polymerizations are used, depending on the required molecular weight and molecular weight

distribution of the polymers. The advantages of the in-situ polymerization process include enabling the grafting of polymer macromolecules onto the surface of nanoparticles, allowing the preparation of the nanocomposites with high nanoparticle loading, and good miscibility with the polymer [30]. The first commercial application of the nanocomposites (clay/polyamide-6) prepared by this process was developed by Toyota Motor Corp in the early 90's of the 20th century [31]. Zeng and Lee prepared poly (methyl methacrylate) and polystyrene/clay nanocomposites by in-situ polymerization [32]. They found that the compatibility of the initiator and monomer with the surface of clay was a critical factor to affect the dispersion of the clay. They claimed that a combination of more polar, less hydrophobic monomer and initiator was preferred in order to obtain high quality dispersion. Additionally, by introducing polymerizable groups onto the surface of the clay, the dispersion quality was further improved. Exfoliated PMMA and PS/clay nanocomposites were successfully synthesized with a clay concentration of 5wt%. Kim *et al* used this process to prepare multi-walled carbon nanotubes and high density polyethylene (HDPE) nanocomposites [33]. They first attached a metallocene catalyst complex onto the wall of multi-walled carbon nanotubes. The polymer branches were then generated on the walls by surface-initiated polymerization. Through transmission electron microscopy and scanning electron microscopy analysis, they found that the nanotubes were uniformly dispersed and were wrapped by PE molecules. Yang *et al* studied the dispersion of silica into polyamide 6 by in-situ polymerization [34]. The silica nanoparticles were modified with aminobutyric acid.

They were dispersed in ϵ -caproamide by stirring. The mixture was polymerized at a high temperature under a nitrogen atmosphere. Their study showed that modified silica was dispersed more homogenous than pristine silica. The process was very useful in preparing inorganic/organic nanocomposites, which can avoid the agglomeration of inorganic particles and improve the interfacial interactions between inorganic components and the polymer.

(c) Melting process

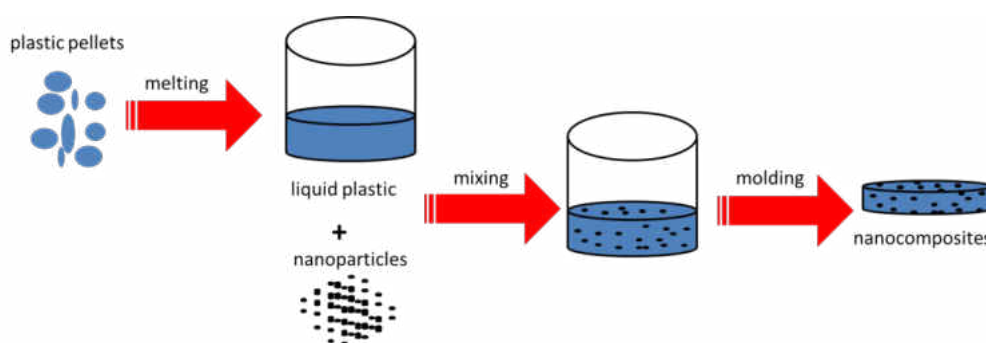


Figure 4 Schematic of the melting processing.

Melting process is an approach to deal with the polymer matrix that is insoluble. It is particularly useful in preparing the nanocomposites composed by thermoplastic polymers such as high-density polyethylene, polyamide-6, polycarbonate, polypropylene, polystyrene, *etc.* In addition, this process allows a high volume of nanoparticles to be mixed into polymer matrix. The process is based on the fact that thermoplastic polymers become soft when being heated up, while the properties of the polymers remain the same after they are cooled down. In other words, the amorphous polymers and semi-crystalline polymers can be processed above their glass transition temperature and melting temperature, respectively. Figure 4

shows the schematic of the melting process. During the process, polymer pellets are melted to form a viscous liquid. The nanoparticles are then blended into the liquid polymer by a high shear mixer or in an extruder. The final bulk samples can be obtained by using injection molding, compression molding, or extrusion.

The addition of nanoparticles into the melting polymer will affect its viscosity, which probably lead to the unexpected polymer degradation under high shear condition. Therefore, processing conditions should be optimized for the whole range of polymer/nanoparticle combinations [24]. Due to its simplicity and speed, this process has been widely applied for large-scale industry production. When preparing the clay nanocomposites using this method, the polymer molecules can enter into the interlayer space between the clay particles. The diffusion process tends to peel the clay layers away. Depending on the compatibility between clay and polymer matrix, and the processing conditions, either an intercalated or an exfoliated structure can be achieved [25]. Cho & Paul prepared Nylon 6/clay nanocomposites using two different types of extruders: single and twin screw extruders [35]. The Killion single screw extruder has a diameter of 25.4mm. The compounding process was carried out at 240°C using a screw speed of 40rpm and a residence of 2.35min. The Haake intermeshing co-rotating twin screw extruder has a diameter of 30mm and centerline spacing of 26mm. The barrel temperature during compounding process was 240°C but the screw speed was 180rpm with a residence time of 5.3min. The extruded pellets were then injected into an 80°C mold under an injection pressure of 70bar and a holding pressure of 35bar. The microstructures of the

nanocomposites were examined by XRD. The result indicated that the interlayer spacing of the clay used in the experiment was 18Å. The exfoliated structure nanocomposite was achieved by using twin screw extruder. The relatively poor dispersion of the nanocomposite using single screw extruder probably was due to the insufficient shear and residence time. Thostenson & Chou prepared CVD-grown multi-walled carbon nanotubes/polystyrene nanocomposites [36]. Since the nanotubes tended to stick to the walls of the mixer, it was difficult to disperse them into the polymer through melting process only. A technique that combined both solution method and melting process was developed. They first dispersed the nanotubes into polystyrene/tetrahydrofuran solution. The solution was then cast into a petri dish and sonicated until the solvent was evaporated. The purpose of the sonication was to assure that the nanotubes were dispersed at the micro-scale rather than the nano-scale, so that they should be encapsulated in the polymer after the solvent was evaporated. The dried nanotubes/polystyrene composites were processed by melting compound with a screw speed of 100rpm. By drawing the sample direct from the extruder, the nanotubes could be aligned. The dispersion of nanotubes was examined by TEM, indicating an excellent dispersion quality.

(d) Special dispersion process for mixing CNTs/CNFs

(1) Ultrasonication

One of the widely used approaches to disperse CNTs into polymers is the ultrasonication process. The process utilizes ultrasound energy to agitate nanoparticles. This

process is usually carried out by an ultrasonic bath or a horn/probe which also known as the sonicator. During the process, the ultrasound propagates by a series of compression. When it passes through the polymer medium, attenuated waves are induced, promoting the “peeling off” of CNTs that located at the outer parts of the CNT bundles/agglomerates. As a result, the individual nanoparticles are separated and high quality dispersion is achieved [37]. Nevertheless, the ultrasonication process is only suitable for dispersing CNTs in solutions that have very low viscosity, such as water, acetone and ethanol. But most polymers are viscous and it is necessary to dissolve or dilute the polymer prior to the dispersion process. While it seems reasonable that when the duration of the process is longer and the intensity of the input energy is higher, better dispersion quality might be obtained, such aggressive treatment could also seriously damage the structure of CNTs, especially when a probe sonicator is employed. In some extreme cases, the graphene layers of CNTs were completely destroyed and the particles were converted into amorphous carbon nanofibers [38]. Obviously, such induced damage would deteriorate the electrical, mechanical, and thermal properties of the CNT-based nanocomposites.

(2) Ball milling

Ball milling is a grinding method that grinds CNTs into extremely fine powders. During the process, the collision between the tiny rigid balls in a concealed container will generate localized high pressure. In many cases, ceramic, flint pebbles and stainless steel are used [39]. In order to further improve the dispersion quality and introduce functional groups

onto the CNT surface, selected chemicals can be included within the container during the process. The factors that affect the quality of dispersion include the milling time, rotation speed, size of balls, and balls/CNT ratio. In some condition, this process can grind the particles to as small as 100nm, and has been employed to transform CNTs into smaller nanoparticles, generate highly curved or closed shell carbon nanostructures from graphite, enhance the saturation of lithium composition in SWCNTs, modify the morphologies of cup-stacked CNTs, and generate different carbon nanoparticles from graphitic carbon for hydrogen storage application [40]. Even though ball milling is easy to operate and suitable for powder polymers or monomers, similar to the ultrasonication process, the potential of induced damages exists.

(3) Non-destructive process: shear mixing, extrusion, and calendaring

While the ultrasonication and ball milling may occasionally introduce damages to the CNT structure, there are alternatives to disperse CNTs without damaging them. Such approaches include shear mixing, extrusion, and calendaring which also known as the three-roll mills. Shear mixing is commonly used in labs to disperse CNTs in a polymer matrix. It is well known that the size and shape of the propeller and its rotation speed determine the dispersion quality. However, it was observed that for some thermosetting polymers, obvious CNTs re-agglomerations become spontaneous under static condition [41]. In such case, much higher mixing speed is required. As discussed previously, extrusion process which usually carried out by a twin screw is available in industry field for large-scale production. The

process is only suitable for mixing CNTs into thermoplastics. Factors that influence the dispersion of CNTs includes the environmental temperature, and the configuration and rotation speed of the screw. The calendaring process, also known as the three-roll mills, is a machine tool that utilizes the shear force created by rollers to mix, disperse, and homogenize CNTs within liquid polymers, oligomers, or monomers. The factors such as rotation speed of the rollers and distance between adjacent rollers greatly affect the dispersion quality. In some conditions, aligned CNTs within polymer matrix could be observed [39].

It should be noted that in order to achieve high quality CNT dispersion, these techniques discussed above, in many cases, are not used alone. Free combinations such as ultrasonication plus ball milling, or ultrasonication plus extrusion are always adopted when fabricating CNT/polymer nanocomposites. Besides these procedures, there are some new techniques that have been developed recently which include: latex technology, densification, spinning of coagulant, layer by layer deposition, and pulverization [39].

2.1.2. Flammability and safety evaluations

Heat release rate (HRR) is one of the most important parameters to evaluate the flammability of polymer materials. It is obtained by conducting cone calorimeter test. A sketch of the instrument is shown in the Figure 5. Besides the HRR, other useful information can also be obtained from the test, such as the total heat released, peak heat release rate (PHRR), time to ignition, mass loss rate, and production of smoke, CO and CO₂.

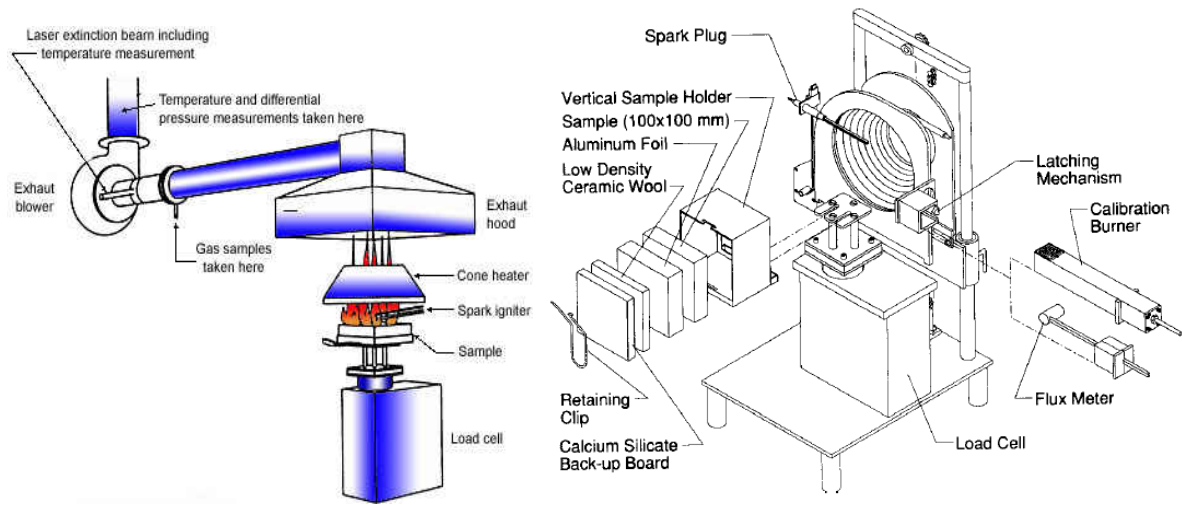


Figure 5 The schematic representation of the ASTM E1345-10 cone calorimeter test method (left, source from internet) and the vertical orientation exploded view of the apparatus (right, source from ASTM E1345-10).

The principle of estimating the HRR during cone calorimeter test is based on the empirical observation: almost all the types of fuel would generate 13.1MJ heat of combustion when 1kg of O₂ is consumed [42]. The rate of oxygen consumption is readily determined by measuring the concentration of oxygen in the exhaust duct and the volumetric flow of air. As a result, the HRR is given by the following equation:

$$\dot{q} = (13.1 \times 10^3) \cdot 1.10 \cdot c \cdot \sqrt{\frac{\Delta P}{T_e}} \cdot \frac{(0.2095 - X_{O_2})}{1.105 - 1.5 \cdot X_{O_2}} \quad (2-1)$$

where \dot{q} = Rate of heat release (kW); c = Orifice plate coefficient ($\text{kg}^{0.5} \cdot \text{m}^{0.5} \cdot \text{K}^{0.5}$); ΔP = Pressure drop across the orifice plate (Pa); T_e = Gas temperature at the orifice plate (K); X_{O_2} = Measured mole fraction of O₂ in the exhaust air (no units). In accordance with ASTM E1354-10, before conducting a cone test, a heat flux meter should be placed below the cone heater and right at the sample holder to ensure the right amount of heat flux will be applied to

the surface of a sample. During the test, as shown in Figure 5, under the cone heater a spark igniter will be used to initiate the flame and will be removed immediately after ignition.

Another important parameter to determine the flammability of PMCs is the thermal stability, which can be measured by thermal gravimetric analysis (TGA). The thermal stability of a polymer matrix not only directly tells how easy the matrix will undergoes decomposition when subject to heat, it also provide the estimation of the char yielding for the composites and the material parameters for the thermal decomposition modeling. The TGA equipment includes a high-precision balance with a platinum pan where the sample is loaded. The weight of the sample is usually in the order of milligram. Much smaller size can be measured if used a quartz crystal microbalance. The balance loaded with sample is placed in an electrically heated chamber, in which the temperature can be controlled and will be recorded against the residual weight of the sample. In many cases, the atmosphere of the chamber will be purged using an inert gas, such as nitrogen, before starting the heating process, in order to prevent oxidation or other undesired reactions. Besides the weight-temperature curve, the weight loss rate against temperature curve is also provided by the test, to evaluate the thermal stability of the sample.

Even though data obtained from cone calorimeter test and TGA is among the most reported data in literatures to evaluate the flammability of composites samples, this information is far from enough to make a final judgment about the safety of the materials. In United States, comprehensive flammability test methods are defined and issued by four

organizations: American Society for Testing and Materials (ASTM), Underwriters' Laboratories (UL), National Fire Protection Association (NFPA) and International Conference of Building Officials (ICBO). The types of flammability and safety tests include tests for smolder susceptibility, ignitability, flash-fire propensity, flame spread, heat release, fire endurance, ease of extinguishment, smoke evolution, toxic gas evolution, and corrosive gas evolution. Each of the tests also includes various types of sub-test. For example, tests for toxic gas evolution can be carried out by approaches such as infrared analysis, gas chromatography, mass spectrometry, chemiluminescence, polarographic methods, paramagnetic methods, ion-selective electrodes, titimetric methods, and colorimetric methods [43].

2.1.3. Overview of the research in fire retardant nanocomposites

The fire performance of nanoclay-polymer nanocomposites is among the most extensively studied. Natural clay, known as Bentonite, is originated from the alternation or deposition of volcanic ash. In some cases, natural clay can also be obtained by the hydrothermal alteration of volcanic rocks. The major content of natural clay is montmorillonite, which is mainly composed by silica. Montmorillonite has a layered structure, which is composed by tetrahedral silicate layer and octahedral alumina layer. In the silicate layer, a hexagonal network is formed by linking the SiO_4 groups, composing a repeating unit of Si_4O_{10} . In the octahedral alumina layer, aluminum atoms are imbedded into the center of the gallery formed by two layers of closely packed oxygen or hydroxyl. The

octahedral layer shares their apex oxygen with the tetrahedral silicate layer, and together they form a sandwich structure. In general the thickness of one sandwich layer is approximately 0.96nm. The chemical formula of montmorillonite clay is $\text{Na}_{1/3}(\text{Al}_{5/3}\text{Mg}_{1/3})\text{Si}_4\text{O}_{10}(\text{OH})_2$.

It is always desirable to modify them organically before disperse into polymer. Otherwise, it is difficult to obtain the intercalated or exfoliated dispersion (because of the hydrophilic property of the natural clay platelets), rendering the size of the clay particles no longer in a “nano” range, and their enhancement in the expected properties, such as mechanical properties and flame retardancy, will be compromised.

Organic modification is typically accomplished by exchanging the inorganic cations (such as Na^+) with the desired organic cations. Hundreds types of organically modified clay have been launched commercially. For instance, Cloisite 20A produced by Southern Clay Products (SCP) is the natural montmorillonite modified with a quaternary ammonium salt. The product is designed to improve the reinforcement, coefficient of linear thermal expansion (CLTE), heat deflection temperature (HDT), and barrier properties of plastics.

In the late 1940s, polymers that combined with nanoscale layered silicates appeared in a patent application [44]. During the early stage of the development, a large amount of clay loading (50% mass fraction) was required. The dramatically decrease in the clay loading (less than 10% mass fraction) were found in patents from General Motors (GM), Imperial Chemical Industries (ICI), and DuPont thirty years later [45]. As discussed previously, two types of morphologies of nanoclay can be achieved, namely, intercalated and delaminated (or

exfoliated) [46].

Zhu *et al* found that when only 0.1wt% of clay was incorporated into polystyrene, the PHRR was reduced by more than 40% and the onset degradation temperature was increased by 40°C, when compared to the pristine polymer [48]. The fire behavior of polystyrene polymer mixed with silicon-methoxide-modified clays was also studied by the same research group. They pointed out that also methoxide might react with clay hydroxyl group, to link the cation and the clay, the nanocomposites did not show any difference in terms of flammability when compared with other polystyrene nanocomposites [49]. Gilman *et al* compared the effectiveness of different kinds of layered silicates when they were added into polystyrene. In their research, they found that fluorohectorite had no impact on PHRR, whereas montmorillonite lead to a 60% decrease in PHRR. The study suggested that the “nanodispersion”, types of layered silicate, and processing conditions would influence the fire behavior of the nanocomposites [50]. Furthermore, research carried out by Morgan *et al* indicated that some other factors, including the clay loading and polymer viscosity would also affect the flammability of polystyrene-clay nanocomposites [51-52]. Other polymer-clay nanocomposites with various matrices such as polypropylene [53], polyethylene [54], PMMA [55], PVC [56-58], EVA [59-60], polyamide-6 [61], vinyl ester [62], unsaturated polyester, phenolic resins [63] *etc.*, were also found the improvement in fire performance in terms of PHRR and TGA, when compared to the pristine polymers. These studies indicated that the intrinsic properties of the parent matrix would influence the effectiveness of nanoscale

additives that aimed to enhance the fire performance of composites. Different mechanisms should be introduced to explain those phenomena. Gilman suggested that, depending on the polymer matrix, the clay may change the decomposition products. It may cause cross-linking and, ultimately, catalyze the formation of carbonaceous char [45].

Researchers reported that a graphite-type char layer had formed during the combustion of polymer-clay nanocomposites with improved flame retardancy, indicating that graphite was potentially a good flame retardant candidate [61]. In fact, expandable graphite and graphite oxide, been considered as another type of nanoparticles that possess layered structure, have already been studied as fire retardants for years. Nyden *et al* conducted molecular dynamic simulations of the thermal degradation of nano-confined polypropylene. The thermal degradation was performed as the gallery spaces between individual graphite sheets changed. The mass loss results of the polymer-graphite nanocomposites indicated that when the space was 3.0nm, there was a pronounced improvement in the thermal stability of the nanocomposites. Nyden *et al* suggested this was resulted from interaction between polymer molecules as well as polymer molecules with graphite. However, when the distance of gallery space was less than 2.5nm, the density of polymer between the graphite sheets was very high, which made the polymer relatively unstable due to the van der Waals repulsions between atoms. Nevertheless, when the space between graphite sheets was too large, the decomposed products tended to escape very easily. This was different to the applications that aimed to improve the mechanical properties of PMCs, where large gallery space (exfoliate)

was always preferred [64]. Motivated by their study, Uhl *et al* studied the fire resistant performance of graphite when it was incorporated into polystyrene. Two approaches were used for preparing nanocomposites: in situ polymerization and melt blending. Organically modified and as received graphite oxide were used. The loading of modified graphite oxide were varied from 1% to 5%. The XRD results showed that the exfoliated dispersion was obtained when 1% of modified graphite oxide was mixed into the polymer. And intercalated dispersion was achieved when a higher loading of modified additives were incorporated. Moreover, the polymer with modified graphite oxide had a much larger d-spacing than the nanocomposites containing non-modified graphite oxide. They observed that the PHRR were reduced by 27-54% depending on the loading of modified graphite oxide (higher loading led to greater reduction). Similar results were obtained when the nanocomposites were prepared by melt blending approach. The only difference was that the latter approach led to a narrower d-spacing [65-66]. When compared the PS-graphite nanocomposites to the PS-clay nanocomposites, the PHRR reduction of the PS-graphite system was roughly 50% of the latter case [67]. However, there was no significant increase in thermal stability for all the samples in their research. Xu *et al* reported more pronounced improvement in thermal stability when graphite was introduced in poly (vinyl alcohol) and epoxy system [68-69]. The fire performance of phenolic-graphite and epoxy-graphite systems was studied and compared. The reinforcements of the composites were fiberglass and aramid. The results showed that phenolic-graphite system had the best flame resistance whereas the epoxy-graphite

composites had the worst flame resistance [70]. However, it was unclear whether the graphite particles were dispersed in nanoscale, as the dispersion had significant impact on the fire retardant performance. By using emulsion polymerization technique, the effective of graphite oxide on the flame resistance of styrene-butyl acrylate copolymer and polystyrene was studied by Zhang *et al.* They found that there was a drastic reduction in PHRR [71-73]. However, it was suggested that due to the thermal degradation of its organic emulsifier, the time to ignition was shorter than that of the pristine sample [74]. In fact, Kashiwagi *et al* claimed that due to the difference of transmission property between pure polymer and polymer mixed with carbon-based nanofiller, the time to ignition should be shorter for the latter case [75]. Uhl *et al* examined the flame resistance property of polyamide-graphite and polystyrene-graphite nanocomposites, the reduction in PHRR were achieved at a level that similar to that of the clay-polymer nanocomposites [76-77].

Other types of famous carbon-based nanofillers are single-walled nanotubes (SWCNT), multi-walled nanotubes (MWCNT), and carbon nanofibers (CNF). Carbon nanotube (CNT), or more specifically MWCNT, was first synthesized in 1991 by Iijima [78]. Later in 1993, Bethune *et al* discovered SWCNT [79]. CNT, essentially, can be considered as rolling up a graphene sheet into a cylindrical structure [80]. It is necessary to stress that when the orientation of rolling up a graphene is different, various types of CNT could be obtained. The diameter of CNT can range from 0.3nm to around 10nm with the aspect ratios from 10^5 to 10^6 . While one layer of graphene sheet will form SWCNT, MWCNT can be obtained by

rolling up multiple layers of graphene sheets. In general, the gallery distance between the layers is about 0.36nm.

The research about CNT is abundant, reporting CNT possesses extraordinary mechanical, electrical, and thermal properties [81-84]. For example, the elastic modulus of a SWCNT is about 1TPa and its density is only around 1.2g/cm^3 , while iron, in general, has an E of 200Gpa and ρ of 7.8g/cm^3 .

Although CNF has a cylindrical nanostructure, unlike CNT, the arrangement of graphene layers of CNF can be varied diversely. The average diameter of CNF is larger than that of CNT, and is about 70-200nm. Its length is about 50-100 μm . The mechanical properties of CNF, in general, are at a lower grade than that of CNT. However, the price of CNF is far more attractive. Furthermore, CNF is welcomed by its scaled-up potential [85].

The flammability of nanocomposites that containing those two-dimensional carbon-based nanoscaled fillers had been intensively studied by Kashiwagi *et al.* Besides evaluating the samples with the well-established cone calorimeter in air, they also examined the flammability of nanocomposites with a gasification device in nitrogen atmosphere. The advantage of the gasification device is that it allows researchers to take video record of the gasification process, which help them to understand the mechanisms of flame retardancy in a vivid manner [86]. For completeness, Kashiwagi *et al* also studied the flammability of PMCs containing other tubular nanoparticles such as alumina silicate nanotube (ASNT), and non-tubular carbon-based particles such as carbon black. After years of research, they found

out that there were five factors related to the fire response of those nanocomposites: the type and concentration of nanotubes, dispersion of nanotubes in polymers, molecular weight of resin, viscoelastic characteristics of nanocomposites, and aspect ratio (length divided by outer diameter of tubes) of nanoparticles. Kashiwagi *et al* reported that well dispersed SWCNTs showed the best effectiveness in reducing the flammability of PMMA. For example, when only 0.5wt% of SWCNT was introduced into the PMMA, the nanocomposites exhibited more than 50% reduction in PHRR, comparing to the neat PMMA. However, when the mass fraction of SWCNTs was less than 2%, the flame retardancy of the nanocomposites was poor. They also observed the aggregation of CNTs within the polymer matrix. Thus, they concluded that the poorly dispersed SWCNTs in polymer led to a higher PHRR than those nanocomposites with well-dispersed SWCNTs. Kashiwagi *et al* explained that a composite sample with well dispersed SWCNTs would form a char layer that had continuous compact network structure. The char layer act as protective coating which resisted both heat convection and radiation as well as slowed down mass (been considered as the fuel to flame) flow. Additionally, they studied the rheological behavior of nanocomposites. They pointed out that the greatest increasing in viscosity of PMMA occurred when adding 0.5wt% of SWCNT, which resulted in a solid-like behavior nanocomposites during the degradation process. This phenomenon ultimately led to a formation of the high quality char layer. Furthermore, they suggested that the integrity of the network at high temperatures was influenced by the molecular weight of the polymer matrix.

In order to address the impact of the aspect ratio of CNTs on the flammability of nanocomposites, Kashiwagi *et al* studied two different MWCNTs with aspect ratios of 49 and 150, respectively. The results indicated that the aspect ratios had no influence in the thermal stability of the nanocomposites. However, the large aspect ratios of MWCNTs tended to increase the complex viscosity and storage modulus of the parent matrix. This led to the creation of compact char structure. As a result, the flammability of the polymers could be significantly reduced when containing MWCNTs with large aspect ratios [75] [19-23].

Besides those nanoparticles that have linear and planar structures, the three dimensional nanoscaled particles, such as polyhedral oligomeric silsesquioxane (POSS), have also been studied by researchers [75]. A POSS particle is composed by an inorganic silica like core and organic functional groups. POSS particles exhibit excellent oxidation stability due to its intermediate structure between silicone and silica. They also have excellent compatibility with polymer matrix because of their organic groups. The three dimensional nanoscaled structures enable their large interfacing area with the host polymer. As a result, the viscosity might be improved, which, as suggested by Kashiwagi *et al*, is desirable to enhance the quality of char during the degradation process of the nanocomposites. With these characteristics, POSS particles have been demonstrated as effective flame retardants [87-88]. If POSS particles contained functional groups that do not readily undergo cross-linking reactions, they would only evaporate at high temperatures. During the combustion process, instead of evaporating directly, they initially decompose by the partial loss of their organic

groups, which have no significant impact on the degradation of the parent polymers, following by the cross-linking reaction with polymer, which incorporates the polymer into the SiO_xC_y networks, namely, char [89-90]. The variations of POSS particles are abundant, depending on their organic substituents. Hybrid Plastics has launched more than 250 different types of POSS particles, making them become important molecular level reinforcements, multifunctional polymer additives, processing aids, and flame retardants.

After conducting thermal gravimetric analysis, Ni *et al* found that when increase the loading of POSS in polymer, the thermal stability and residue of the polymer matrix increases [89] [91-92]. Gupta *et al* studied the flame resistant property of epoxy vinyl ester resin containing POSS. The results showed a reduced heat release rate and smoke. Furthermore, unlike carbon base nanofiller, the ignition time of this nanocomposites was delayed. Therefore, they claimed that the mechanism of POSS to retard flame propagation was the reduction in fuel volatilization, the formation of stable and non-permeable surface chars [93]. Devaux *et al* found a simultaneous reduction in total heat release and heat release rate when 10wt% of POSS particles were introduced into polyurethane (PU), and which was coated onto PET knitted fabric. They explained that the reduction in flammability should be attributed to the high thermal stability of the nanocomposites and the formation of uniform and compact char residue during the combustion reaction [94]. Okoshi and Nishizawa also reported the high quality char formation, when POSS-based nanocomposites was coated onto the surface of polycarbonate [95]. However, the flame resistant efficiency of POSS-based

nanocomposites have not yet been extensively studied because of their high cost and sometimes failing to form strong residue when compared to clay or nanotubes-based nanocomposites [96]. Kashiwagi *et al* studied the flame retardancy of POSS in PTME-PA, SBS and PP. They found that even though the PHRR was decreased, the total heat release of the nanocomposites didn't show significant reduction. Moreover, the char analysis indicated that when POSS particles were incorporated into polymer, there was no great increase in carbonaceous char yielding, and the majority of the residue was composed by the inorganic component of the POSS [97]. Another study done by the same group examined the flammability of textiles containing. They found that there was no significant changes in PHRR, even though the time to ignition was delayed, indicating that POSS served only as thermal stabilizers rather than flame retardants [97]. Moreover, a recent study showed that when trisilanol phenyl POSS particles were incorporated into PMMA, no significant flammability reduction was observed during cone calorimeter tests [98]. General speaking, the flammability of nanocomposites containing POSS depends on three factors: the structure of POSS particles, the type of polymer matrix, and the dispersion quality. As long as a certain type of POSS could increase their cross-links with the parent polymer and form large amount of SiO_xC_y network, the flame retardancy of the nanocomposites would be improved [75].

2.1.4. Intumescent fire retardant coating

In addition to direct mixing flame retardants into polymer matrix to achieve the fire retardancy, coating intumescent layers onto the surfaces of PMCs is another popular and

effective approach. There are two types of intumescent coatings: the traditional chemical intumescent fire retardant coating and the physical intumescent coatings containing expandable graphite [99].

The traditional chemical intumescent coating is usually composed by a carbon source (monomer, dimer, trimer), an acid source (ammonium phosphate, diammonium phosphate), and a gas source (urea, melamine, chlorinated paraffins). The mechanism of the fire retardancy is to produce foaming char, which serves as barrier to prevent mass loss and heat transfer. Namely, dehydrate the materials into char, release gas in a transitional semi-liquid state that sufficient to enable foaming and expansion, and carbonize the materials without char collapse. However, the application of urea formaldehyde, ammonium phosphate and starch would reek of formaldehyde, and thus is not leach resistant [100].

As the name may suggest, the other type of the intumescent coatings contains expandable graphite. The expandable graphite is obtained from treating crystalline graphite with intercalants, such as sulfuric acid or nitric acid. Since no covalent bonding exists between the planes of the carbon atoms, the intercalant can be inserted into the gaps between the planes and positioned within the graphite lattice. When exposed to heat, the inserted molecules would decompose and release gases, resulting in the expansion of the coating. The expansion rate of the expandable graphite is much higher than that of the traditional intumescent coatings, and thus it provides better insulation. However, it is well known that the expandable graphite might experience the “popcorn effect”, that is the expansion of the

grains of graphite would cause the grains to pop off from the underlying materials and might also damage the underlying structure by inducing in air turbulence [100].

There are other shortcomings associated with the intumescent coating. For instance, due to application of the hydrophilic components, the exterior intumescent coatings usually lack weathering ability. This may lead to the coatings be dissolved and rendered inactive by water or water vapor, or require elevated cure temperatures and extended cure times. Protective top coating can be used to overcome this drawback, but the cost will rise. Another shortcoming is the poor adhesion of the intumescent coating to substrates [101]. Compared to other fire retardant system, even though intumescent coating has better fire retardancy, lower smoke emission, high temperature resistant, *etc.*, screening tests conducted by Sorathia *et al* had led them to conclude that intumescent coatings were not sufficient to protect shipboard spaces during fire scenario, and thus could not replace the **thick** batt or blanket type fibrous fire insulation. For example, the requirement for the cold side temperature of a composite structure, after being subjected to certain heat flux for 30min, should be lower than 250F. However, the measured cold side temperatures of the composites coated with commercial intumescent coatings were about 260F. Only those sandwich structure composites samples that containing 3 inches of balsa core can pass the test. Future more, Sorathia *et al* suggested that prior to the wide application of intumescent coating, issues such as the cost, performance, and durability of the coatings over a life time of use should be carefully addressed [102-103].

2.2. Numerical Modeling of PMCs Subject to Heat Flux

While the experimental research provides qualitative information to understand the mechanisms of flame retardancy for various types of retardant systems, it is necessary to develop a mathematical model that is able to predict the evolution of material status and temperature in a quantitative sense, as such, critical information could be obtained for the future materials design. However, it is difficult to develop a comprehensive model for such a complex and unstable phenomenon, in which involves the coupling of fluid dynamics, chemistry, and conjugate heat transfer between solid, liquid and gas phase. Nevertheless, it is still possible to come up with some relatively manageable models, which is constructed based on the simplification of some conditions during combustion reaction. For example, the physical condition of a simplified combustion reaction is that the sample is horizontally exposed to a stable external heat flux and the materials in each phase are isotropic. When this model is set up, it can be extended to the conditions of filled polymer, filled composites, and simple char-forming systems.

The ability to develop an accurate mathematical model to explain fire resistance mechanisms crucially depends on the understanding of fluid dynamics and degradation phenomenon of the polymers. And also depends on the understanding of how these factors (such as thermal conductivity, heat capacity, heat absorption and permeability of char, and viscosity of the polymer) affect the flammability of the composites. Fortunately, the models to simulate the combustion phenomenon are abundant [104-105].

Furthermore, the degradation and decomposition of the composites will lead to losses in mass and that leads, in turn, to losses in mechanical strength of the structure. Therefore, it is important to develop the capability to predict the mechanical properties of PMCs when they are subjected to high temperatures.

Bai *et al* studied the stiffness of PMCs composites under high temperature conditions. They presented a model that estimated the mechanical properties of the material by dividing the states of the polymer matrix into four temperature dependent and three transition states [106]. In the case of the thermo-mechanical response of PMCs simultaneously subjected to heat flux and loading, Asaro *et al* proposed a temperature and time dependent constitutive theory to study the mechanical degradation of the material, a theory inspired by the crystal plasticity study, takes full account for the anisotropy of the laminate elastic and interlaminar shear inelastic behaviors, also proposing that the property degradation is monotonic with density [107-108]. Other examples of real time thermo-mechanical models involving anisotropic properties of PMCs and softening of matrix and reinforce fibers were presented by Gibson [109] and Feih [110-112].

However, in the case of post-fire mechanical analysis, it is found that when the heat treated PMCs cooled down to room temperature, the material tends to regain some of their initial strength and stiffness [113]. With this in mind, it would be problematic to assemble the temperature and time-dependent material properties to obtain the bulk material properties. Sorathia *et al* proposed a temperature-limit criterion to assess the post-fire mechanical

properties of coupon shape composites. They assumed that when the temperature of the material during fire exposure was lower than the critical temperature, the sample would retain its initial mechanical properties after cooling down to the ambient temperature [114]. Mouritz and Mathys presented a two-layer model to study the post-fire mechanical properties of marine composites such as glass fiber reinforced polyester and glass fiber reinforced vinyl ester. After the composites were exposed to heat flux, they assumed that the residues were composed of one layer of un-degraded material and one layer of charred material, with the virgin mechanical resistance assigned to the un-degraded layer while zero mechanical resistance was assigned to the char layer. The challenge in this model lies in the determination of the depth of the char layer. Initially, an empirical correlation between the depth of the char layer, the exposure time, and the time at that charring first occurred was proposed, with experimental data of char depth was acquired through physical measurement [115-116]. Later, they introduced a thermal degradation model into their post-fire mechanical study. Then the depth of the char layer was determined by using a pulse-echo instrument and percentage remaining resin content (RRC) criterion [117-118]. Unlike Mouritz's small scale study, Keller *et al* studied the post-fire mechanical behavior of liquid cooled PMCs slabs in large scale. They proposed a three-layer model that modeled the heat treated PMCs as composed by the fully degraded layer, the partially degraded layer, and the virgin layer [119-120]. Recently, Bai and Keller presented a post-fire mechanical model that considering the E-modulus recovery which occurred between the glass transition and

decomposition of the polymer matrix [121].

Due to the complex nature of the polymer degradation and the combustion process, governing equations of the thermal degradation models are difficult to solve by analytical methods such as Fourier Transforms, Bessel Function, and Separation of Variable (SOV) Techniques, or by the semi-analytical procedure in reference to the global coordinates such as variational and weight residue methods. This problem has often been analyzed by numerical methods. One of the early studies regarding the thermal degradation model for PMCs was proposed by Henderson *et al* [122]. In their model, it was assumed that there was no accumulation of gas, no volumetric expansion, material parameters such as specific heat was only a function of temperature, and thermal equilibrium exists between gases and solid. In the model, a second order PDE for energy equilibrium with proper boundary and initial conditions was solved using finite difference method (FDM). Later, modified and refined models with more accurate input material parameters that solved either by FEM, finite volume method (FVM), or FDM were presented by Gibson, Looyeh, Krysl, Lattimer, and Lua [123-128]. Recently, Staggs developed a much different model with the inclusion of a developing char layer front at which energy and mass balance equations were established [129].

There are also many research papers that deal with the thermal response modeling of composites panels coated with protective layers while subjecting to heat, especially the thermo-chemical modeling of the composites panels protected by intumescent coating

[130-136]. However, most of research was focused on the detailed modeling of the coating layer while, the impact of porosity and permeability of the underlying composites was ignored, probably due to the limited available data. These parameters have recently been estimated by Goodrich *et al* as they were studying the microscopic changes within the composites structure during fire, which makes it possible to refine the thermal response model of the structure [137].

CHAPTER 3

SYNTHESIS AND PROCESSING OF NANOCOMPOSITES AND HYBRID NANOPAPER

3.1. Processing of Hybrid Nanopaper

As mentioned in the first chapter, the purpose of coating a nanopaper onto the surface of a composites structure is to take advantage of the pre-existing char layer to improve the fire resistance performance of the structure. The effectiveness of the pre-existing char layer depends on their thermal conductivity in the transverse and perpendicular directions, their permeability, and some other related properties. Therefore, in order to fully reveal the synergistic effect between those nano-sized particles within the hybrid nanopaper, the design is critical.

The base material has been used in this study to fabricate the hybrid nanopaper is the vapor grown carbon nanofibers (Polygraf III, PR25-PS-HHT), supplied by Applied Science, Inc. with a diameter of 50-100nm and a length of 30-100 μ m. The choice of CNFs over CNTs is based on their following advantages:

(a) Easier to disperse and process

CNFs have diameters of 50-200nm, while CNTs have diameters of only 1-30nm.

As a result, the energy associated with CNFs/solution interfacing should be much less than that with CNTs/solution interfacing. Therefore, CNFs are easier to be dispersed and processed.

(b) Easier to modify

Unlike CNTs' "perfect" cylindrical structures, the surfaces of CNFs are featured with graphene edge planes. And this "pre-existing defect" makes CNFs readily modified through traditional chemical functionalization or thermal treatments in both small and large scales. On the other hand, the walls of CNTs have to be modified before the functionalization process. As such, it requires more steps and costs more to process CNTs.

(c) Lower cost

Typically, CNFs cost an order-of-magnitude lower than CNTs. The price of CNFs ranges from \$100 per pound to \$500 per pound, while that of CNTs, depending on the quality and purity, goes from \$100 per pound to more than \$750 per gram. Due to the difficulty in processing, the cost for CNTs can go even higher.

Other nanoparticles used in this study included: the Cloisite Na⁺ clay, which was the pure and non-modified form of montmorillonite clay and was obtained from Southern Clay, Inc; the exfoliated graphite nano platelets (xGnP), which were obtained from XG Sciences. Both of them had a layered structure. Besides these nanoparticles, traditional fire retardants, ammonium polyphosphate (APP), were also used in the hybrid system. The specific type of APP, AP423, is supplied by Clariant International Ltd.

The as-received nanoparticles were mix together under designated weight ratios (more details will be discussed in the next chapter). Then they were dispersed in distilled water

(0.6g of the base material CNF + 600ml water + other nanoparticles) with the aid of surfactant Triton-X100 (3-5 drops per 600ml). The mixture was sonicated by a sonicator for certain amount of time under designated input power (more detail will be presented in the next chapter). It is important to note that the more the input power during the sonication process, the better the dispersion quality should be. Nevertheless, the nanoparticles could be damaged if the sonication time was too long or the input power was too high. Therefore, it is important to control the input energy carefully in order achieve an optimized dispersion quality.

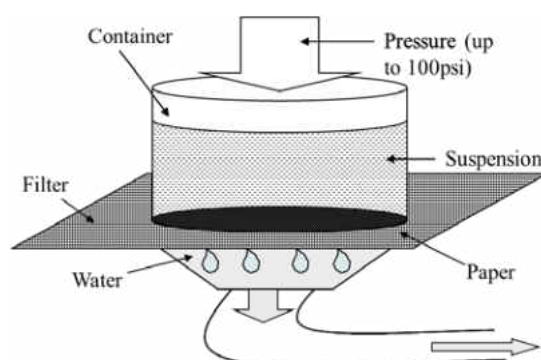


Figure 6 High pressure filtration system.

After the sonication process, the well dispersed suspension will be filtered through a polycarbonate or hydrophilic PTFE filter with the pore size of $0.5\mu\text{m}$. The filtration process can be carried out by a vacuum pump or a compressor. The system, as shown in Figure 6, uses compressed air to fabricate nanopapers. The maximum pressure of the compressed air is 100psi and the diameter of the closed cylinder container is about 110mm. Therefore, this

system is capable of fabricating relatively small size hybrid nanopapers that have low permeability.

Another way to fabricate hybrid nanopapers is by using vacuum as a driving force to filtrate the suspended mixture. As shown in Figure 7, the size of nanopapers made by this type of filtration system can be relatively large (18 by 18 inches) as the suspension can be continuously poured into the open container during the filtration. In addition, it is possible to roughly control the concentrations of the nanoparticles layer by layer. For example, when fabricating hybrid nanopapers that containing nanoclay, the pores of the filter would probably be covered by the clay particles and thus inhibit the flow of the water. Sometimes it is even impossible to continue the filtration process. However, the problem can be solved by first pouring the suspension without the planar structure nanoparticles into the container, so that the thin initial layer on the surface of the filter will prevent the above phenomenon from occurring.

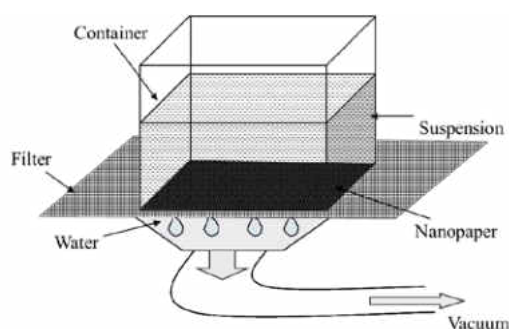


Figure 7 Vacuum assisted filtration system.

The quality of the nanopaper made by the high pressure or vacuum assisted system is

shown in Figure 8. It can be seen that the carbon nanofibers and nanoparticles are well dispersed, no aggregation can be found. The nanoparticles are entangled in the CNF network (more nanopaper SEM images will be shown in the next chapter).

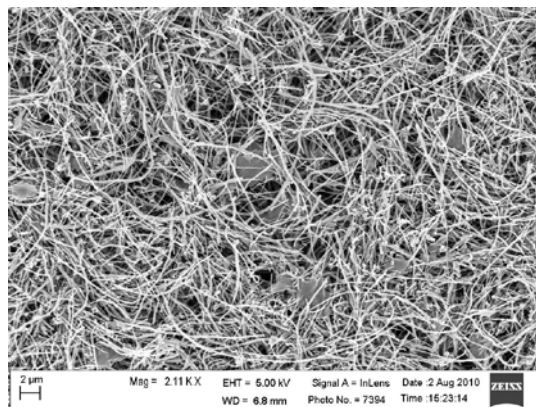


Figure 8 SEM image of a hybrid nanopaper.

3.2. Processing of Nanocomposites Coated with Nanopapers

After the nanopapers have been fabricated, they are coated onto the surface of PMCs by resin transfer molding (RTM) process. Since it is undesirable for the fire resistance purpose that the surface of the nanopaper been covered with resin, a surface treatment prior to the RTM is necessary. It is carried out by the following steps: 1. Place a piece of mold release fabric that has slightly larger size than that of the nanopaper on the inside surface of a mold; 2. Evenly brush nanoclay/water paste on the fabric and then place the nanopaper onto the wet fabric so that the pores of the nanopaper should be covered by the nanoclay particles and the resin should not penetrate through the nanopaper during the RTM process; 3. Heat up the

mold in an 120°C oven for 2 hours to dry the nanopaper and fabric. In order to prevent the distortion of the nanopaper while drying, a proper weight should be applied onto it. The final appearance of the surface treated nanopaper before RTM process is shown in Figure 9. As shown in the figure, the edges of the nanopapers are sealed by tapes in order to prevent the resin from flowing to the other side of the nanopaper, rendering the surface treatment useless.



Figure 9 Final appearance of the nanopapers before the RTM process.

There are two approaches to carry out the RTM process in this study. The difference between them is the source of the force to drive the resin: one uses compressed air and the other uses compressed nitrogen. The pressure of the compressed air system can reach up to 100psi. The chamber size of the aluminum mold used for this system is 10 by 10 by 0.3 inches. Eight layers of glass fiber mats should be fit into the chamber before RTM process. Most of hybrid nanopapers can be infused with resin in this system and it is relatively easy to operate it when compared to the compressed nitrogen system. As shown in Figure 10, initially,

valve 3 will be opened and valve 1 and 2 will be closed, such that the vacuum pump will remove the air that is trapped within the glass fiber mats in the mold. Then valve 3 will be closed and valve 1 and 2 will be opened such that the compressed air being generated by a compressor will drive the resin in the resin tank into the mold. By slightly opening and closing valve 3, extra air could be driven out of the mold. Therefore, a better quality composites panel will be made.

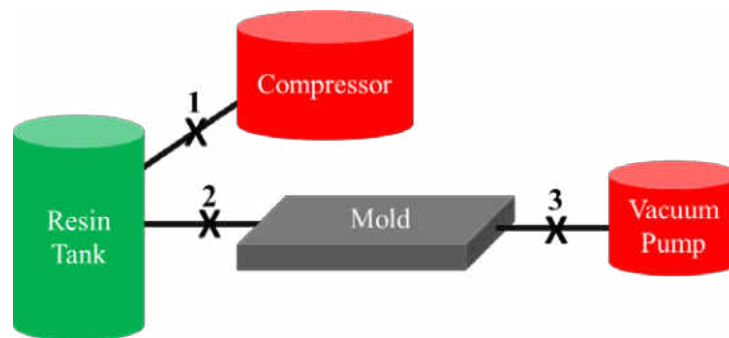


Figure 10 Compressed air VARTM system.

However, when the permeability of the nanopaper becomes very low such as when it contains nanoclay, the 100psi pressure is not high enough to fabricate high quality nanocomposites, *i.e.* some locations of the nanopaper may detach from its underlying structure due to the incomplete resin infusion. Therefore, a higher pressure is needed to accomplish the infusion. And the compressed nitrogen RTM is designed for this special purpose. The pressure of the compressed nitrogen can reach to 2000psi. The size of this aluminum mold is about 12 by 8 by 0.16 inches and 4 layers of glass fiber mats should be

placed in the chamber of the mold. Due to the pressure limitation of the pipe system, the pressure of the compressed nitrogen is regulated to 300psi, which is enough for the infusion of any nanopapers mentioned in this dissertation. As shown in Figure 11, resin is added into the resin tank through valve 2 before the RTM process. During the infusion process, initially, valves 5 and 6 are opened and valves 1, 2, 3, and 4 are closed. Therefore, the air trapped within the glass fiber mats in the mold will be removed by the vacuum pump. Then valve 6 will be closed and the vacuum line will be disassembled. Valve 1 and 5 will be opened and the high pressure from the nitrogen tank will drive the resin into the mold. By slight opening and closing valve 6, extra air within the mold could be driven out. After holding pressure for about 5 minutes, valve 1 and 5 will be closed, and the RTM process is completed.

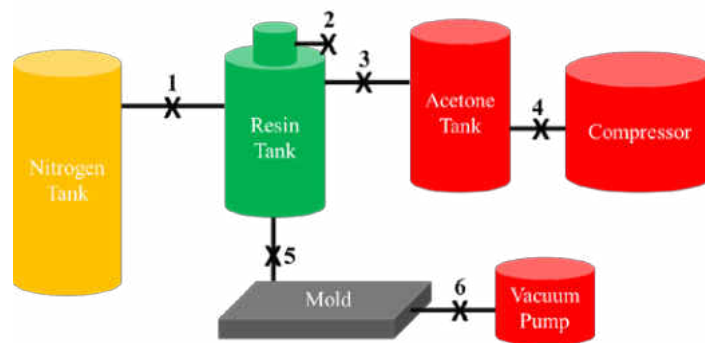


Figure 11 High pressure VARTM system.

The challenge to operate this system is the limited time margin. In order to sustain the 300psi pressure, the pipes that been used in this system are not disposable and the diameter of the pipe is small. In addition to that, the resin been used in this dissertation is polyester, which will cure under the room temperature. Therefore, the limited operation time is

necessary to prevent the resin from blocking the pipes. Immediately after the RTM process, the whole system will be thoroughly flushed with acetone to eliminate the resin residue. Specifically, open valve 2 to reduce the pressure within the resin tank. Then close valve 2, disassemble the pipe that is connected to valve 5 and put it in a sealed empty container. Open valve 3 and 4, such that the acetone will be driven into the resin tank to flush the system. In order to make sure that the residual resin has been completely washed away, a second flush is necessary.

CHAPTER 4

FIRE RETARDANT PERFORMANCE EVALUATION OF THE NANOCOMPOSITES

4.1. Introduction

Understanding the combustion process of composite laminates has led to the knowledge that fire resistant performance can be improved chemically and physically in both vapor phase and condensed phase by reducing the heat and/or fuel below critical levels. In short, fire can be prevented if the concentration of gaseous mixture and auto-ignition temperature are maintained below critical values [138-139].

For the analysis of the fire resistant performance of polymer composites, open literature primarily focuses on discussing parameters such as heat release rate, peak heat release rate, and time to ignition. If the evaluation on material's fire performance was based solely on these data, it ran the risk of oversimplification, and possibly misleading [140]. For example, when evaluating structural materials, understanding their capability to sustain loading under heat condition is also important [115-116] [141]. While the glass transition temperature " T_g " is an intrinsic material property that cannot be modified without changing the molecular structure of the polymer, it is possible to reduce the mass loss and mass loss rate in order to enhance the structural integrity of the material during heating. In this case, it is necessary to evaluate those parameters, which would otherwise have been ignored.

The discussion in this chapter focuses on the experimental study and can be divided

into three steps: 1. optimize the weight ratio between the nanoparticles that compose the hybrid nanopaper, 2. select right materials to realize the proposed idea, and 3. extensively evaluate the optimized nanopaper by various tests, to gain deep understanding in the fire retardant mechanism of the nanopaper and to provide data for future thermo-mechanical degradation modeling. Specifically, the flame retardant performance of the composites prepared by directly mixing nanoparticles into polymer matrix was studied. It was found that when the polymer matrix was composed by 3% of xGnP, 17% of APP, and 80% of polyester resin, the synergistic effect between xGnP and APP was better revealed. The fire response of the nanocomposites was further investigated after coated with the xGnP/CNF nanopapers. The study showed that the nanocomposites coated with the nanopaper containing xGnP/CNF were equal to 3/1 possessed best flame retardant property. Then the fire performance of the composites coated with the xGnP/CNF nanopaper was compared with the nanopaper that containing nanoclay particles. Due to the low permeability (led to the pressure build-up beneath the nanopaper) of the Clay/CNF nanopaper, the detachment of the nanopaper was observed. However, such phenomenon did not occur to the xGnP/CNF nanopaper. Based on these findings, fire performance of the composites coated with the nanopapers containing xGnP/CNF/APP equaled 3/1/9 was thoroughly evaluated under various heat fluxes. And the fire retardant mechanism was studied.

4.2. Fire Retardant Performance Evaluation of the xGnP/APP Nanocomposites

In this section, exfoliated graphite nanoplatelets (xGnP) were introduced into polymer matrix to reduce the flammability of the composites. Their planar structure is such that the permeability of the composites would be reduced and, thus, the path of decomposed polymer (fuel) would become torturous [86] [142-144]. However, the addition of nanofillers alone into the polymer, sometimes, will not satisfy the requirements of fire regulations. The incorporation of traditional additives is still necessary [145-146]. Therefore, when preparing the samples, the intumescent flame retardants-APP particles were used with a weight ratio of APP/resin equaled. Under this ratio, 25wt%, 15wt%, 10wt% and 5wt% of APP particles were replaced by xGnP. The samples were characterized by XRD and cone calorimeter. To attempt a further improvement of the flame resistant efficiency of the nanocomposites, xGnP/CNF hybrid nanopapers were designed, fabricated, and coated onto the surfaces of the laminates. Besides their unique planar structure that should introduce the barrier effect, the selection of xGnP was also intended to take advantage of their anisotropic thermal conductivity ($K_{\parallel}=3000\text{W/m}$; $K_{\perp}=6\text{W/m}$), so heat could be easily dissipated transversely during the heat transfer process. Thus, less heat should be able to penetrate through the coating. In addition to that, xGnP and APP were still mixed into the polymer matrix at the given ratio of xGnP/APP/Resin equaled 2/18/80. The samples coated with hybrid nanopapers were characterized by cone calorimeter, and the char collected after the test was examined by SEM.

Materials

Vapor grown carbon nanofibers (Polygraf III PR25-HHT) were supplied by Applied Sciences, Inc. (Cedarville, Ohio, USA), with an average diameter of 80nm and average surface area of about 50m²/g. The traditional flame retardants, ammonium polyphosphate (AP423), were supplied by Clariant International Ltd. The exfoliated graphite nanoplatelets (xGnP) were obtained from XG Sciences with a thickness of 5-15nm. The reinforcement, E-glass fiber mat, was supplied from Composites One, Inc. with a surface density of 800g/m² and an average thickness of 0.85mm. The matrix material for the composites was unsaturated polyester resin. It was a pre-promoted, thixotropic, orthophthalic type of resin that was supplied by PolyGard (product code: GP100P; density: 1.1g/cm³; heat deflection temperature: 75°C). The hardener used in this study was methyl ethyl ketone (MEK) peroxide, and was mixed with resin at a weight ratio of 100:1.

Processing nanocomposites containing xGnP and APP

Prior to mixing with the unsaturated polyester, xGnP was rinsed with acetone to improve its wettability with the resin. Specifically, xGnP powders were dispersed in acetone and then the mixture was sonicated using the Misonix S-3000 sonicator with a power of 90 watts for 20min. The acetone was then drained using a vacuum system. Finally, the treated xGnP and as-received APP were mixed into the unsaturated polyester by a mechanical shear mixer (Model 50002-30, manufactured by Cole-Parmer Instrument Company, Illinois, USA) with the speed of 1400rpm for 2.5 hours. After preparing the matrix, the RTM process was

carried out to prepare the glass fiber reinforced nanocomposites. The polymer was injected into an aluminum mold containing eight layers of glass fiber mats at a pressure of 80psi. After resin was allowed to cure in the mold at room temperature overnight, the composites were post-cured at 120°C in an oven for 2 hours. Table 2 shows the compositions of the xGnP nanocomposites.

Table 2 Composition of the xGnP-based nanocomposites.

Sample ID*	Contents (wt %)			Weight ratios of GNP/APP/Resin (%)
	GF	Resin	Additives	
xGnP-APP-0-laminates	51.75	48.25	0	0/0/100
xGnP-APP-15-laminates	48.23	41.41	10.35	5/15/80
xGnP-APP-17-laminates	49.18	40.66	10.16	3/17/80
xGnP-APP-18-laminates	47.30	42.16	10.54	2/18/80
xGnP-APP-19-laminates	49.78	40.18	10.04	1/19/80
xGnP-APP-20-laminates	50.71	39.43	9.86	0/20/80

* For the purpose of simplification, the above sample IDs are called Control, APP15, APP17, APP18, APP19 and APP 20 later, respectively.

Processing hybrid nanopapers and nanocomposites

The as-received CNF and xGnP were dispersed in distilled water with the aid of surfactant Triton-X100. The mixture was sonicated with the Misonix S-3000 for 30min under a power of 30-50 watts. After the suspension was well-dispersed, nanopaper was fabricated by filtering the suspension with a compressed air system (see Figure 6 in Chapter 3) at a pressure of 80psi. The nanopaper was then coated onto the surface of the nanocomposites by RTM process. The compositions of the hybrid nanopapers and nanocomposites are shown in Table 3.

Table 3 Composition of the hybrid nanopapers and nanocomposites.

Nanocomposites sample ID*	Composition (wt %)					Weight ratios in the nanopaper
	GF	Resin	xGnP	APP	Nanopaper	
GA-L	49.83	40.14	1.00	9.04	0	no paper
C0G1-GA-L	50.17	38.91	1.10	9.84	1.20	CNF/xGnP = 0/1
C1G3-GA-L	49.16	39.73	1.11	9.99	1.17	CNF/xGnP = 1/3
C1G5-GA-L	49.10	39.81	1.10	10.00	1.16	CNF/xGnP = 1/5
C1G1-GA-L	48.12	40.59	1.13	10.17	1.15	CNF/xGnP = 1/1
C3G1-GA-L	48.85	39.99	1.12	10.04	1.17	CNF/xGnP = 3/1
C5G1-GA-L	48.88	40.01	1.11	10.00	1.17	CNF/xGnP = 5/1
C1G0-GA-L	48.27	40.46	1.13	10.14	1.15	CNF/xGnP = 1/0

* For the purpose of simplification, the above sample IDs are called GA, C0G1, C1G5, C1G3, C1G1, C3G1, C5G1 and C1G0 later, respectively, GA is the control sample.

Cone Calorimeter Tests

According to the standard ASTM E 1345-10 (ISO 5660-1), the fire retardant performance of the composites with and without nanopaper coatings was evaluated by a FTT cone calorimeter (manufactured by Fire Testing Technology Ltd) with an incident heat flux of 50kw/m^2 . For all the samples, the unexposed surfaces and side edges were wrapped in an aluminum foil. There was ceramic wool within the sample holder of the cone calorimeter. Therefore the unexposed surfaces of the samples were insulated. The samples were evaluated in a horizontal position with the surfaces coated with nanopapers, when applicable, directly exposing to the heat flux during cone calorimeter tests. The thickness and diameter of the samples were, respectively, 8mm and 75mm, with resin volume and weight fraction of approximately 70% and 50%, respectively. The experiments were repeated 2 times for all of the samples. The results showed less than 10% variation. The flammability data reported in this study was the average of the 2 replicated tests.

X-Ray Diffraction Analysis

X-Ray Diffraction (XRD) analysis was carried out to evaluate the microstructure of the direct mixing samples (*i.e.* without nanopaper coating) by using a Rigaku D/MAX X-ray diffractometer (45kV, 30mA), which was equipped with a copper X-ray tube (wavelength of 1.54\AA). The scanning rate of the analysis was 0.06 degree per 7 seconds.

Scanning Electron Microscopy Analysis

The hybrid nanopapers and the char of the samples coated with nanopapers after cone

calorimeter test were sputter-coated with a conductive gold layer. They were analyzed by a Zeiss Ultra –55 SEM machine at extra high tension (EHT) of 5kV. This SEM machine was also equipped with an energy-dispersive X-ray spectroscopy (EDX), which was able to identify the chemical composition of the sample.

4.2.1. Results and discussion

Cone calorimeter test results of the nanocomposites containing xGnP and APP

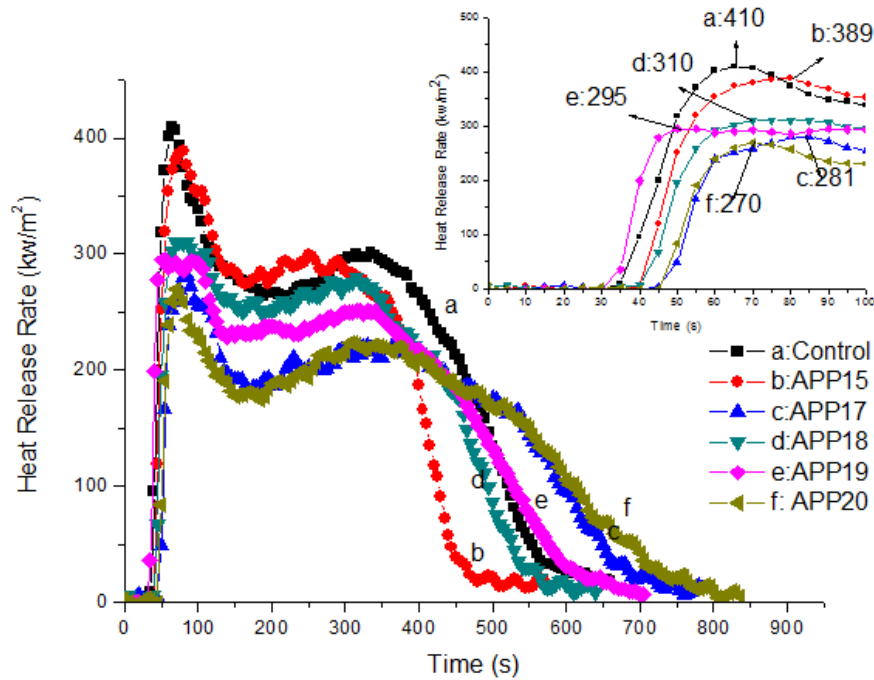


Figure 12 Heat release rate of the samples with different weight ratios of APP and xGnP.

Figure 12 shows the Heat Release Rates (HRR) of the samples containing different weight ratios of polyester, APP and xGnP. Compared to the control sample, the HRR of the samples containing APP and/or xGnP are visibly lower. The sample APP17 that is composed of 80% of resin, 17% of APP and 3% of xGnP shows the lowest HRR curve. However, the

other samples with the content of APP greater than 17% (xGnP is lower than 3%) or lower than 17% (xGnP is higher than 3%), show a higher HRR. With this information, it is inferred that there is an optimized weight ratio between APP and xGnP.

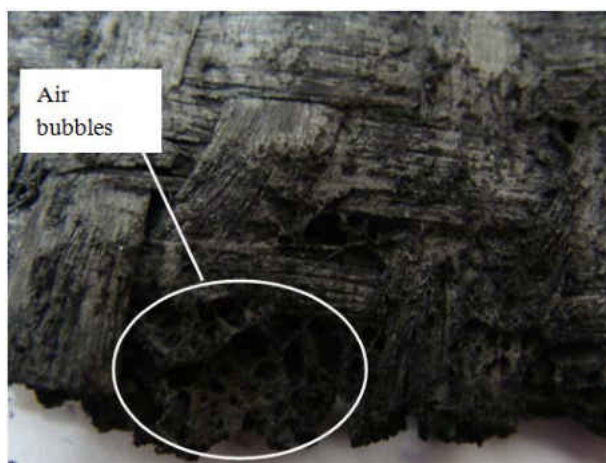


Figure 13 Air bubbles that had been trapped in the char structure of the xGnP-APP-17-laminates after the cone calorimeter test.

A reason for these results is that the APP particles serve to reduce the HRR of the samples by acting as “blow agents” to generate air bubbles, which are expected to lower the thermal conductivity in the thickness direction (Figure 13), and eventually, slow down the heat being transferred into the underlying materials.

However, the presence of xGnP could impair the thermal isolation ability of the foaming char layer due to its planar structure, high thermal conductivity, and heat absorption ability [75]. Therefore, the reduced HRR should be a consequence of a competing mechanism with the introduction of xGnP particles, that is their high heat absorption and thermal conductivity will stimulate the pyrolysis of the polymer. While the high thermal conductivity

and the stimulation of polymer pyrolysis will accelerate the heat dissipation and rate of char creation, respectively. In addition, the planar structure of xGnP might serve as barrier to inhibit the diffusion of the decomposed fuel to feed the flame above the surface of the laminates. As shown in Figure 14, it is proposed that the mechanism is that the planar structure of xGnP will decrease the permeability of the samples, making the diffusion path of the decomposed gases tortuous.

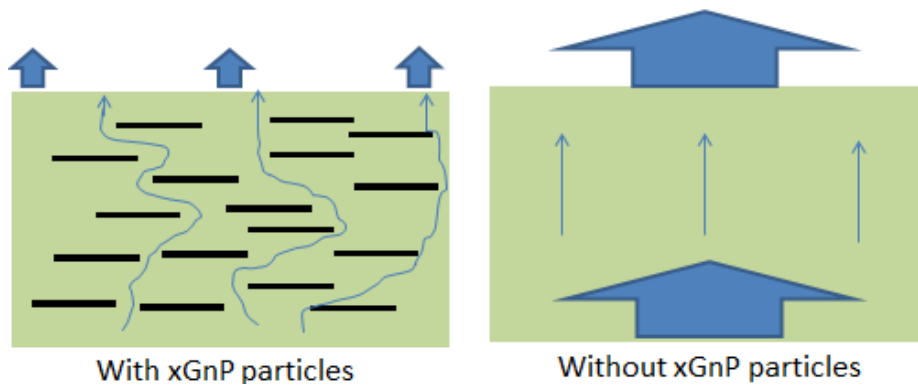


Figure 14 The presence of the xGnP nanoparticles inhibits the diffusion of the decomposed gases.

This mechanism is supported by the Mass Loss Rate (MLR) of the samples. Figure 15 shows the MLR of the control sample and the sample containing 3% of xGnP and 17% of APP (other samples have the similar results, but are excluded in this figure for ease of reading). It can be seen that the MLR curves closely line up with the HRR curves, which suggests that the reduced HRR is the consequence of reduced MRL. In other words, the xGnP effectively slow down the migration of the decomposed fuel.

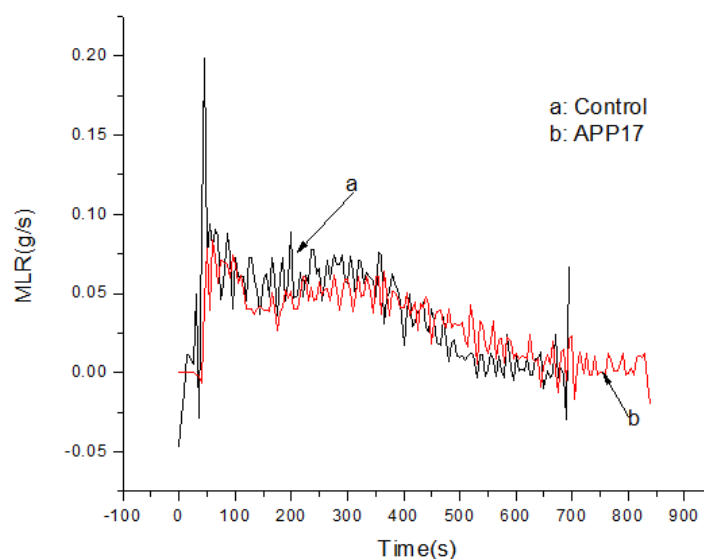


Figure 15 Mass loss rate of the samples.

From the cone calorimeter tests results shown in Table 4, it can be seen that the variations in weight ratios of xGnP and APP among the non-control samples yield limited differences in total heat release rate and char yielding. This indicates that the relatively large amount of intumescent flame retardants, APP, has a dominant effect. With the exception of APP15, the PHRR of APP17, APP18, APP19, and APP20 are relatively close, as shown in Table 4, suggesting that the addition of small amounts of xGnP particles into the polymer would not significantly reduce the flammability of the samples that already have a high concentration of APP additives, unless the loading of xGnP is relatively high (5% in this case).

Table 4 Summary of cone calorimeter test results of the mixing group.

Sample ID	Control	APP15	APP17	APP18	APP19	APP20
Total Mass (g)	55	58	58	57	57	56
Char Yielding (wt%)	0	17.8	14.6	10.9	15.9	14.1
Total Heat Released (MJ/m ²)	135	111	115	115	118	116
Peak Heat Release Rate (kw/m ²)	410	389	281	310	295	270
Total Smoke Release(m/m ²)	6063	6455	5270	5677	6104	4948

* The thickness of all the samples is about 8mm.

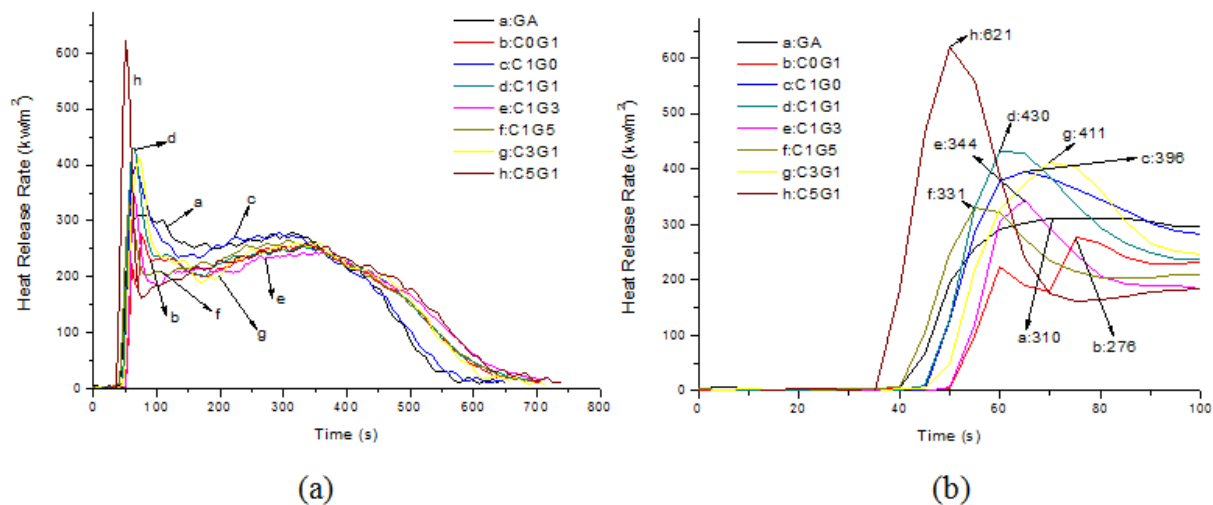


Figure 16 Heat release rate of the samples coated with the xGnP/CNF hybrid nanopapers. (a) 0~800s; (b) 0~100s.

The HRR of those samples coated with xGnP/CNF hybrid nanopapers are shown in Figure 16. As shown in Figure 16(b), the PHRR of C0G1 is 11% less than that of the control sample GA. The PHRRs of the C1G5, C1G3, C1G0, C3G1, C1G1 and C5G1 samples are 7%, 11%, 28%, 33%, 39% and 100% higher than that of the control sample, respectively. Such a high PHRR is undesirable for the purpose of fire retardancy and a more sophisticated material design is needed. However, it can be seen in Figure 16(a) that immediately following the peaks of the paper coated samples, there is the dramatic decrease in the HRR. Considering long high HRR after the peak, it is unlikely that the drop is due to the complete consumption of the composite material, rather is likely due to the formation of a protective char layer. In fact, it is intended that the introduction of the hybrid nanopaper should serve as a pre-existing char layer (which would otherwise being formed gradually during the combustion process

such as the case of direct mixing) to reduce the HRR as soon as possible. In terms of analyzing the long term heat release behavior, the Total Heat Release (THR) during different time period can be calculated by:

$$THR = \int_{t_0}^t HRR dt \quad (4-1)$$

By integrating the HRRs from 0s to 100s, the THR before 100s is shown in Table 5. The THR before 100s of the samples coated with C0G1, C1G5 and C1G3 papers are, respectively, 33%, 16% and 31% less than that of GA sample. The differences between the GA sample and the rest of samples are within 10%.

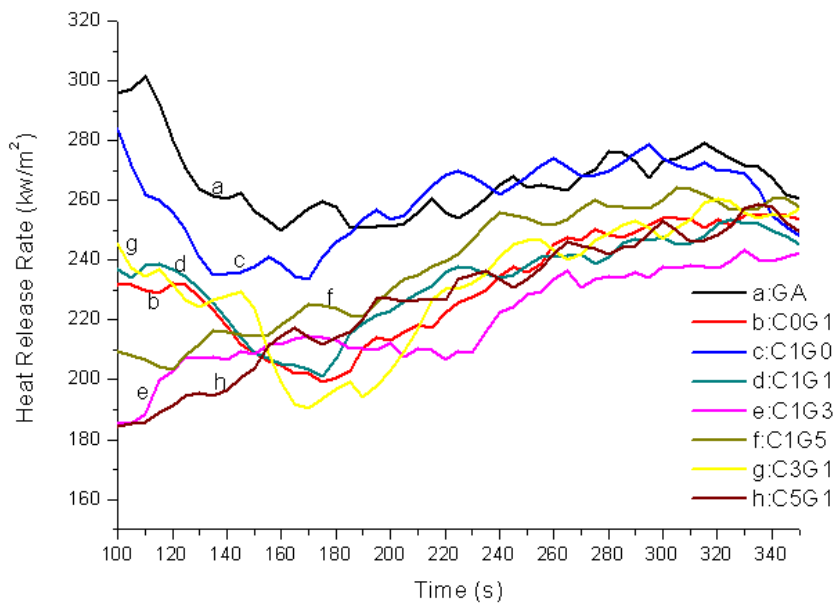


Figure 17 Heat release rate between 100s~350s.

During the major burning stage (100-350s) where most of the mass is consumed, Figure 17 shows that the samples coated with xGnP dominated hybrid nanopapers exhibit

lower heat release. By integrating the curve, it can be seen that the sample coated with C1G3 has the lowest THR (as listed in Table 5). The difference of THR between this sample and GA sample is more than 17%. Only the sample coated with a pure CNF nanopaper has similar THR value to the GA sample. This is attributed to the fact that the pure CNF nanopaper has much higher permeability, thermal conductivity, and heat absorption ability than the nanopapers containing xGnP. Therefore, only promoting the flammability of the composites.

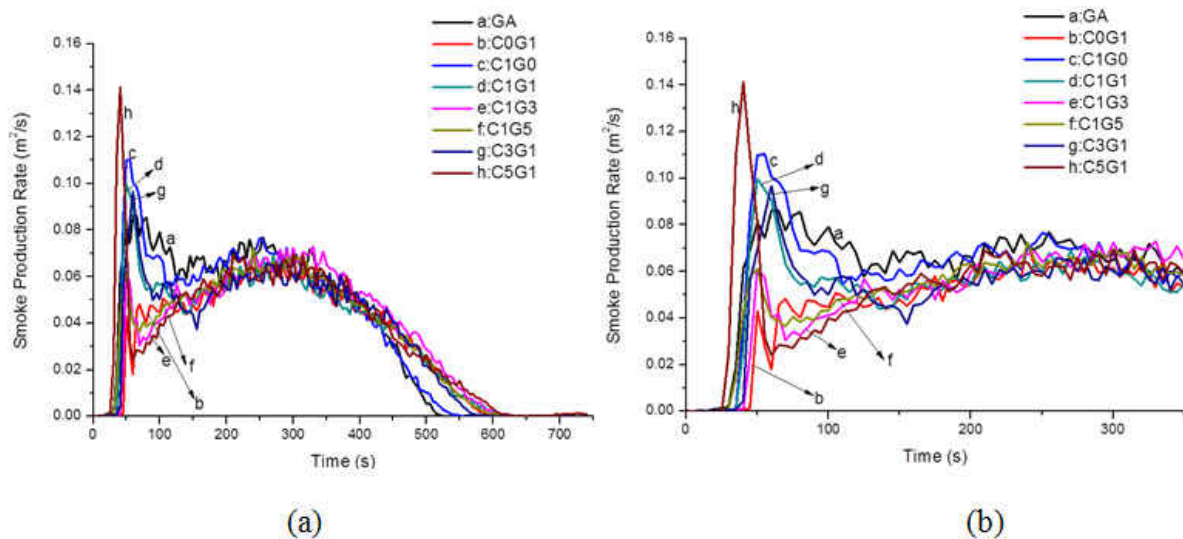


Figure 18 Smoke production rate of the samples coated with the nanopapers. (a)0~700s; (b)0~350s.

The above results demonstrate that the reduction in the THR of the composites is achieved by coating with the hybrid nanopapers. The hybrid nanopapers that are dominated by xGnP have better flame retardancy than that of the CNF dominated hybrid papers. Similar to the fire retardant mechanism previously discussed (Figure 14), it is suggested that the

Table 5 Summary of cone calorimeter test results of the paper-coated group.

Sample ID	GA	C0G1	C1G5	C1G3	C1G1	C3G1	C5G1	C1G0
Total Mass(g)	57	57	57	57	59	58	59	57
Char Yielding (wt%)	10.9	18.3	18.9	11.1	19.9	19.1	19.3	18.9
Peak Heat Release Rate (kw/m ²)	310	276	331	344	430	411	621	396
Total Heat Released (MJ/m ²)	114	110	115	112	117	113	122	114
Heat Released (MJ/m ²) (0~100s)	17.1	11.5	14.4	11.8	17.3	16.7	18.9	18.1
Heat Released (MJ/m ²) (100~350s)	69.3	60.3	62.0	57.2	60.7	60.6	59.0	67.5
Total Smoke Release(m/m ²)	5677	4811	5582	5765	5760	5578	5670	6011

* The thickness of all the samples is about 8mm.

xGnP dominated nanopapers have much lower permeability, thereby slowing the diffusion rate of the decomposed gases that feed the flame above the surface of nanopaper. In addition, despite resulting in a higher PHRR, it is expected that the CNF/xGnP hybrid nanopaper should accelerate the char formation process. This fire retardancy mechanism is further confirmed by analyzing of the Smoke Production Rate (SPR) data. As shown in Figure 18, the SPR curves are highly similar to the heat release rate curves. Most of the smoke generated before 350s, with the peaks of the GA samples (a) and the sample coated with CNF dominated nanopapers (c,d,g,h) occurring before 150 seconds, while the peaks of the samples coated with xGnP dominated nanopapers (b,e,f) occurring near 350s. The SPR of the sample coated with xGnP dominated nanopaper before 150s is much lower than the GA sample.

While HRR is an important parameter to evaluate the fire performance of PMCs [140], other parameters such as mass loss are useful in regarding to the material's post-fire mechanical properties. Figure 19 shows the change of remaining mass of the matrices during fire testing. Mathematically, the parameter is calculated by normalizing the instantaneous mass of the matrices during cone calorimeter test with the initial mass of the matrices. Since the glass fibers are thermally stable, and their mass remains unchanged during the whole testing, the instantaneous mass of the matrix of a sample can be obtained by minus the weight of the glass fibers from the total instantaneous mass of the sample, which is recorded by the cone calorimeter.

$$\text{Mass Percentage of Matrix} = \frac{M_t - M_G}{M_i - M_G} \quad (4-2)$$

where: M_t is the mass of sample recorded during test;

M_G is the mass of glass fiber which equals $800 \text{ g/m}^2 \times A_{\text{sample}} \times 8$;

M_i is the initial mass of the sample

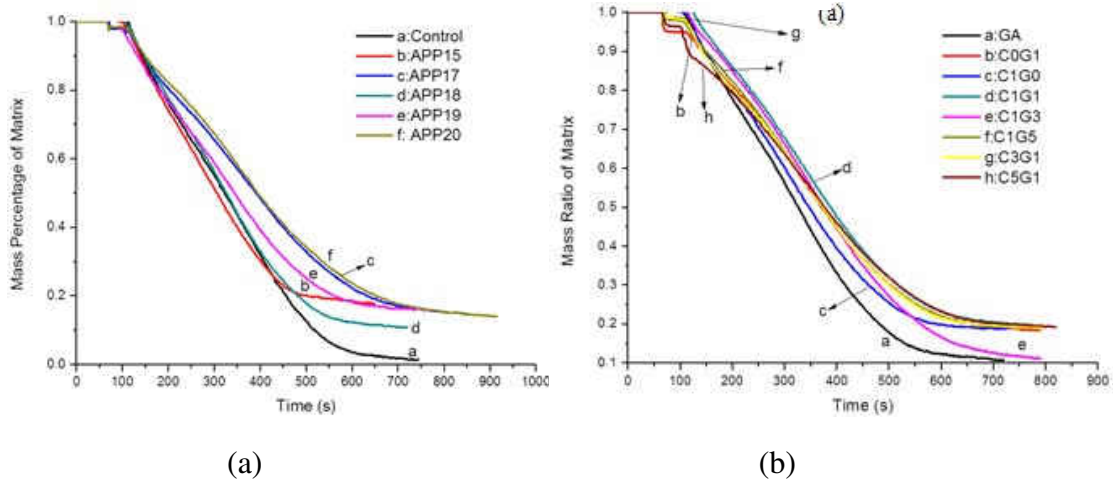


Figure 19 Mass percentage of the remaining matrices during the cone calorimeter tests. (a) mixing samples; (b) paper coated samples.

As shown in Figure 19(a), the polymer matrix of control sample has almost been completely consumed, while the samples containing APP and xGnP show an improved ability to retain their matrices during the fire testing. The sample containing 17% of APP and 3% of xGnP exhibits the similar results with the sample containing 20% of APP only. For the nanopaper-coated samples, as shown in Figure 19(b), all the samples show an improved capability in preventing the mass loss when comparing to the control sample. In addition to the low permeability of the CNT/xGnP hybrid nanopaper, which will effectively slow down the diffusion of decomposed gases, another possible explanation, as discussed previously, is that carbon-based material might accelerate the process of forming the protective char layer on the surface of the samples.

XRD results of the samples containing different concentrations of APP and xGnP

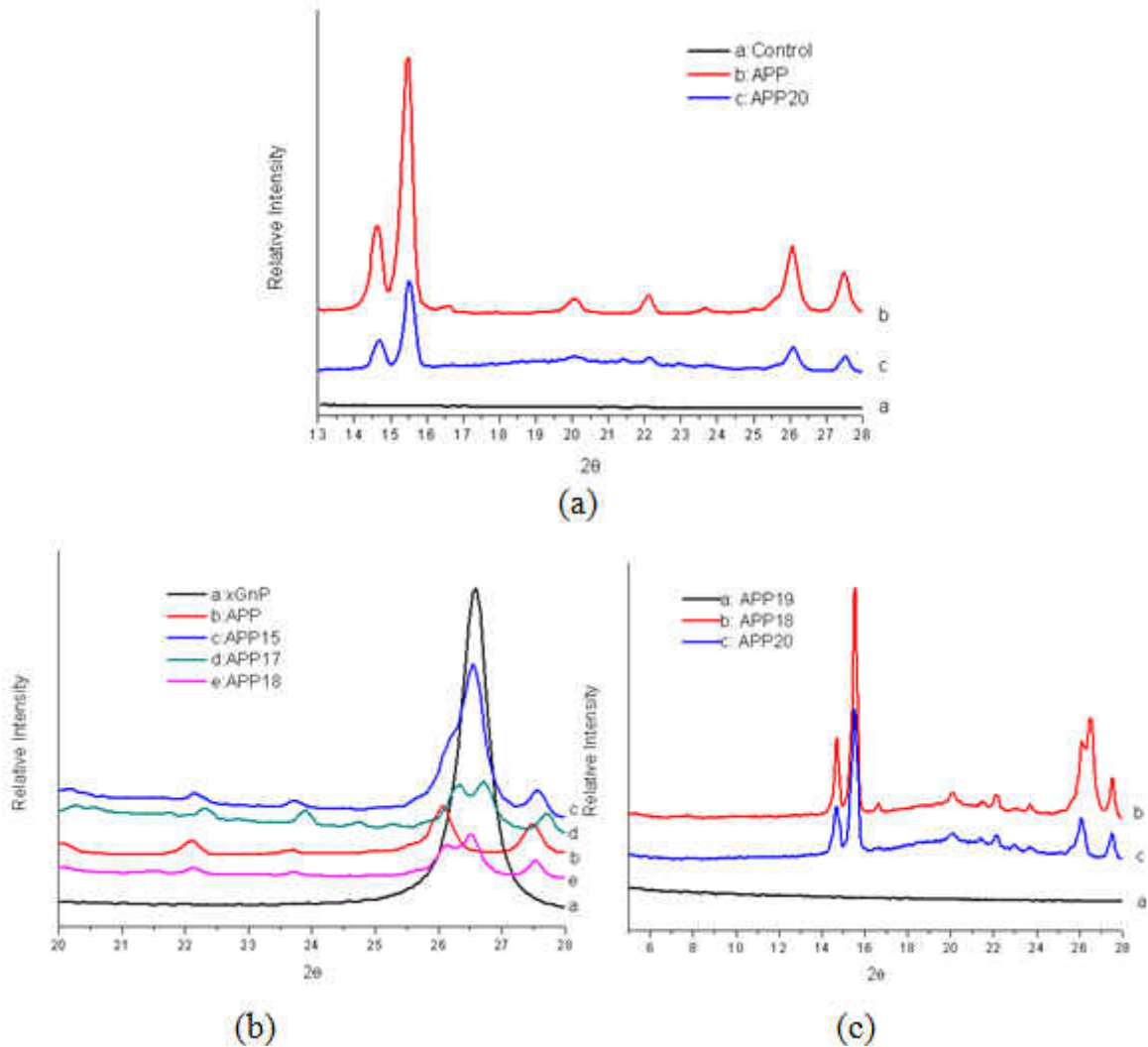


Figure 20 XRD results of the samples with different concentrations of APP and xGnP.

As shown in Figure 20(a), there is no peak for the sample only composed of glass fiber and polyester resin, while the peaks for APP powder (curve b) and the sample only containing APP are similar, only differing in their intensity, which is due to the obvious fact that the concentration of APP in the composites sample is lower than pure APP powder.

Figure 20(b) shows the XRD pattern of the xGnP powder, the samples containing APP only,

and the samples containing both APP and xGnP. It can be seen that the peak for xGnP is around 26.5° . When the particles are mixed into polymer with APP, the XRD patterns of the mixed samples are simply the combination of the XRD patterns of the pure APP and xGnP powder. For example, there are two peaks around 26° for the samples containing 2 and 3% (curves d and e) of xGnP. The lower angle peak is attributed to APP and the higher angle peak comes from xGnP. When the concentration of xGnP is increased to 5%, the contribution from xGnP around 26° becomes more obvious. These curves indicate that the mixing xGnP into the polymer using mechanical mixer at room temperature will not result in a significant change of intercalated distance between xGnP platelets.

As shown in Figure 20(c), it is interesting to note that there is no peak for the sample with its matrix being composed of 1% of xGnP, 19% of APP and 80% of polyester. If the xGnP particles had been exfoliated, there should be peaks for APP. The possibility of significant experiment errors is highly unlikely, since the tests for this sample was repeated for four times at different locations of the sample. This might have resulted from the APP and xGnP particles becoming amorphous under such a ratio. However, the phenomenon needs further investigation.

Morphologies of the nanopapers and char materials of the paper-coated samples after cone calorimeter tests

Morphologies of the nanopapers

The morphology of the nanopaper before coating onto the surface of PMCs is shown

in Figure 21. SEM images 21(a) and 21(b) indicate that xGnP particles are well dispersed and entangled within the CNF networks. As the loading of xGnP increases within the hybrid nanopapers, due to more pores of the CNF network will be covered by xGnP, the permeability of the nanopapers decreases. As shown in figure 21(c) and (d), the pure xGnP and CNF nanopaper should have the lowest and highest permeability, respectively.

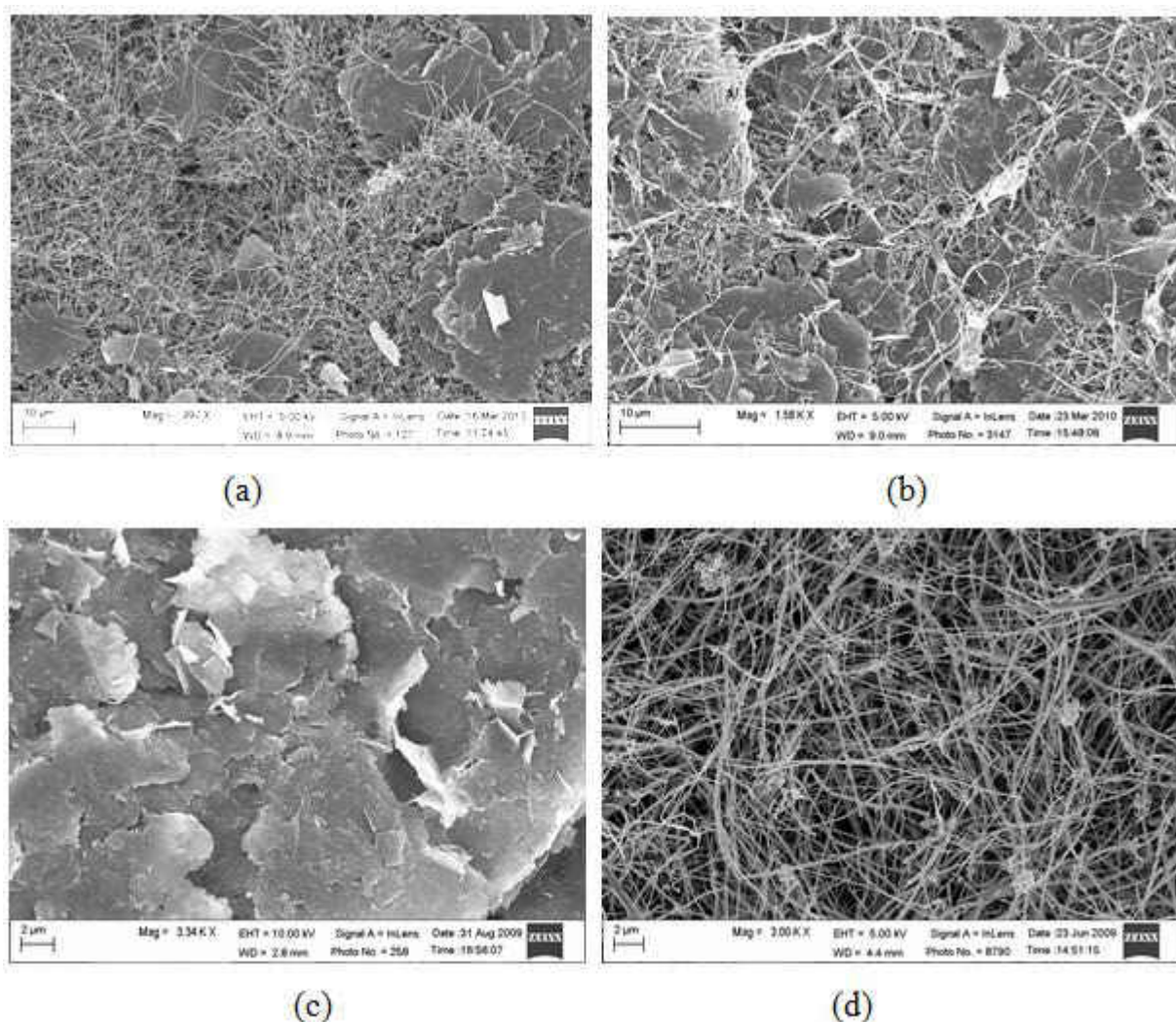


Figure 21 SEM images of the hybrid nanopapers. (a) C1G3; (b) C3G1; (c) C0G1; (d) C1G0.

Morphologies of the char materials after cone calorimeter tests

Figure 22 and 23 show the char characteristics of the composites samples coated with the nanopapers after cone calorimeter tests. There were three types of char had formed during the combustion reaction, labeled as A type, B type and C type. It is clear that A type char is the most compact, while the C type char has the highest porosity. Generally speaking, a sample that generates more compact char should possess higher flame retardant property [147]. The sample, C1G3 and C0G1, shows the largest amount of A type chars in the surface and also shows best flame resistance (Figure 22). However, most of the chars from sample C1G0 are composed of type B and C (Figure 23), and the sample even shows higher flammability than the control sample.

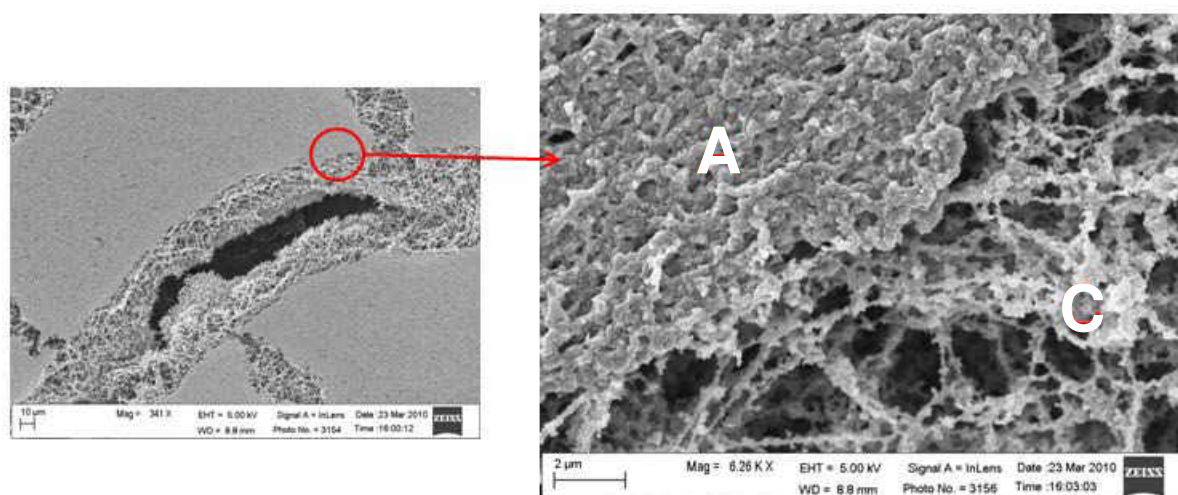


Figure 22 Char SEM image of the samples C1G3-GA-L and C0G1-GA-L.

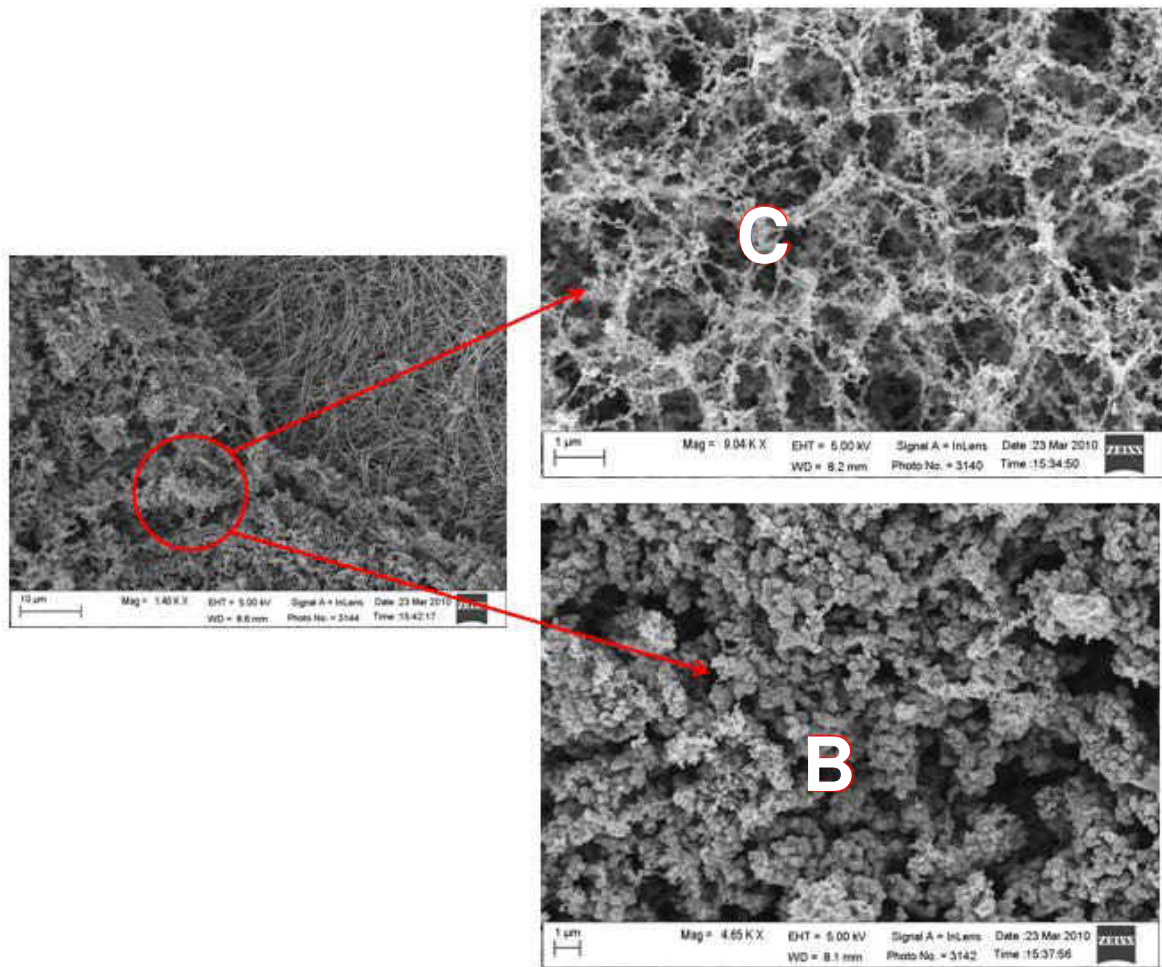


Figure 23 Char SEM image of the sample C1G0-GA-L.

4.2.2. Conclusions

By analyzing cone calorimeter test data and char characteristics, it is found that the thermal properties and permeability of composites and chars play important roles in determining the flammability of the materials. xGnP particles show an excellent barrier effect when they are mixed in polymers and incorporated into CNF-based nanopapers. Specifically, with an addition of 3% xGnP and 17% APP into polymer matrix, fire performance of the sample is the best of those tested, suggesting that there is an optimized weight ratio between xGnP and APP that uses their synergistic effect. By coating hybrid nanopapers onto the

surfaces of those samples, the fire resistance performance of the composites is further enhanced. The traditional flame retardants, APP, are proved to be important to reduce the overall heat release of the PMCs during the combustion reaction process.

4.3. Fire Retardant Performance Evaluation of the Glass Fiber Reinforced Polyester Coated with the xGnP/CNF/APP and Nanoclay/CNF/APP Nanopaper

In this study, new types of hybrid nanopapers were developed. APP particles were introduced into the CNF paper. As demonstrated by the previous section, APP was expected to serve as a blow agent when subjecting to heat. The expansion of the coating layer should lower the through-thickness thermal conductivity of the nanopaper. Furthermore, APP itself should initiate the creation of char that would protect the underlying polymer from fire damage. Nanoclay, similar to xGnP that possessed planar structure, was incorporated into the nanopaper. The fire retardant efficiency of nanopapers containing nanoclay or xGnP was evaluated and compared by cone calorimeter test. In addition, since the tensile modulus of the composites is dominated by glass fibers which should have no damage after fire, and the compressive modulus of the composites is determined by the mechanical properties of matrix, while the flexural modulus represents the combined effect of glass fibers and polymer matrix, the post-fire flexural moduli of the PMCs coated with these two types of nanopaper were evaluated by three-point bending test. The outcome of this study should help to determine which nanopaper system is more effective to improve the structure integrity of the PMCs under fire conditions.

In addition to the materials described in section 4.2.2, Cloisite Na⁺ clay was used in the following study. The nanoclay particles were the pure and non-modified form of montmorillonite clay, which was obtained from Southern Clay Products, Inc. According to the product specifications, 90% by volume of the dry particles have sizes that less than 13µm. The procedure of fabricating nanopaper and nanocomposites was similar to the process discussed in section 4.1.2, except that the RTM process was carried out by the compressed nitrogen system (Figure 11). As discussed in Section 3.2, the width and length of the chamber of the mold was 8 inches by 12 inches. The pressure used in RTM process was 250psi. The final thickness of the sample was roughly 3.5 mm. Furthermore, it should be note, due to the low permeability, the time to fabricate the nanopapers containing nanoclay was much longer than that nanopapers containing xGnP. The composition of the hybrid nanopapers and nanocomposites is shown in Table 6.

Table 6 Composition of the hybrid nanopapers and nanocomposites.

Nanocomposites sample ID	Contents (wt %)			Weight ratios of particles in the nanopaper
	GF	Resin	Nanopaper	
Control	50.6	49.4	0	no paper
CCA serials	49.3	47.6	3.1	CNF/Clay/APP=5/1/9
CXA serials	51.0	45.8	3.2	CNF/xGnP/APP=5/1/9

Besides the cone calorimeter test (35kw/m² applied heat flux in this section) and SEM analysis described in section 4.2.2, other characterization experiments had been conducted, which include:

Thermal gravimetric analysis (TGA)

The TGA instrument used in this study was TGA-Q500 from TA Instruments, USA. The characterization of the hybrid nanopapers infused with the polyester resin was conducted in a nitrogen atmosphere at a flow rate of 40ml/min and a heating rate of 10°C/min. The weight of a sample was approximately 10mg, which was obtained by knocking off the surface of the nanocomposites. Therefore, the TGA sample was composed of resin and hybrid nanopaper. The nitrogen atmosphere was chosen to simulate the anaerobic degradation of polymer within the PMCs.

Post-fire three-point bending test

Post-fire flexural moduli of the samples were determined by three-point bending test by using an INSTRON 5582 universal testing machine. The coupons' sizes were 25x130mm which were cut from the composites plates that were prepared by the RTM process. Prior to the bending test, they were exposed to 35kw/m² heat flux for varied amounts of time. The exposure time was selected based on the HRR curves, and was selected such that the samples would not lose all their mechanical resistance. When the samples caught fire, due to their small size, the flame could be easily quenched by covering a fire proof fabric. In accordance with the standard ASTM D790-10, the support span was 76mm and the speed of crosshead motion was 2.4mm/min. The test would stop if either the deflection of the centerline of the specimen reached 12mm or there was a dramatic drop in the load-deflection curve. The flexural modulus degradation rate was evaluated using a normalized modulus of elasticity,

which was calculated by [148]:

$$E_n = \frac{L^3 \cdot m}{4 \cdot b \cdot d^3 \cdot E_0} \quad (4-3)$$

where: E_n was the normalized modulus of elasticity in bending, E_0 was the modulus of the sample before it was exposed to heat, L was the support span, b was the width of the sample, d was the depth of the sample, and m was the slope of the initial straight line of the load-deflection curve.

During the bending test, the surface against the support experienced the largest stress. Hence, it was possible that even though the samples might have slight differences in the degree of damage within the exposed surfaces. The placing of the undamaged surface against the support might eliminate such differences on the flexural moduli being measured. However, this result was unlikely to occur if the damaged surface was chosen to be placed against the support, as shown in Figure 24.

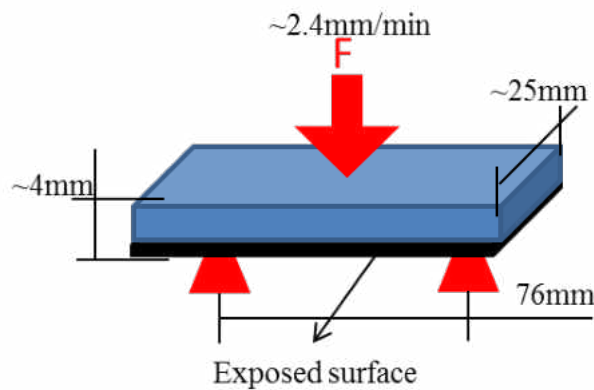


Figure 24 Experimental setup of a composite sample for the three-point bending test.

4.3.1. Results and Discussion

Cone calorimeter test results

Table 7 Summary of cone calorimeter test results.

Sample ID	THR (MJ/m ²)	THR (0~180s) (MJ/m ²)	THR (“platform”) (MJ/m ²)	First PHRR (kw/m ²)	Second PHRR (kw/m ²)	Time to Second PHRR (s)
Control	57.9	51.7	38.4	/	430	80
CCA	59.5	37.3	34.4	271	332	170
CXA	55.5	38.2	28.2	359	283	185

The HRR curves of these three groups of composite samples are shown in Figure 25 and summarized in Table 7. By integrating the heat release rate through time, the heat released before 180s for the Control, CNF/Clay/APP (CCA), and CNF/xGnP/APP (CXA) samples are 90%, 63%, and 69% of the total heat release (THR), respectively. Initially, the control samples have the highest HRR and become the lowest after 180 s. Such drop in HRR for the control samples is due to the fact that most of the polymer has been consumed up. Specifically, because all the samples have the same amount of polymer, when the control sample burns dramatically during the 0~180s period (90% of THR), it has less fuel to consume in the later combustion stage. Therefore, it can be concluded that in general, the samples coated with hybrid nanopapers exhibited better fire retardancy than the control samples.

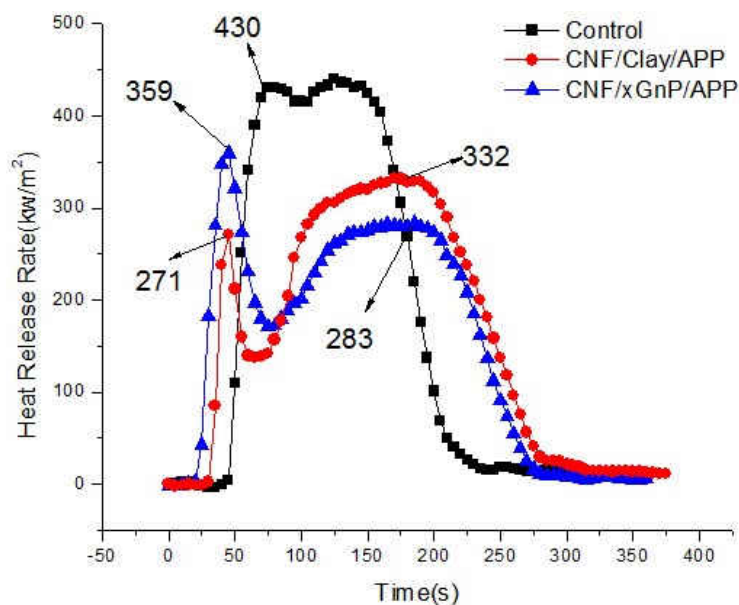


Figure 25 Heat release rate of the samples.

It is interesting to note that there are two peaks for the samples coated with hybrid nanopapers while there is only one peak for the control samples. The first and second peaks of the CCA samples are 37% and 23% lower than that the peak heat release rate (PHRR) of the control samples. The first and second PHRRs of CXA are 17% and 34% lower than that of the control samples. The first peaks of the paper-coated samples come from the ignition of the samples. The second peak of paper-coated samples and the peaks of the control samples all appear in the highest “platform” of their HRR curves. The “platform” represents the major period of decomposition of the composites, since the heat release during the platform period (less than one third of the total combustion process) for the Control, CCA and CXA samples take 66%, 58%, and 51% of the THR of the samples, respectively. It can be seen that the second PHRR of the CCA and CXA samples appear at 170 s and 185s, respectively. Much later than the control samples whose peaks occur at about 80s. As shown in Figure 25,

immediately following the first peak of the paper-coated samples, a dramatic decrease in HRR occurs. It is unlikely that the drop is due to the complete consumption of the polymer matrix as the control sample does. Rather it is due to the formation of the protective char layer. In fact, the introduction of the hybrid nanopaper is intentionally designed to serve as a pre-existing char layer and to prompt the formation of the protective char. The occurrence of the second peaks could be attributed to the cracking of the char layer near the end of combustion process.

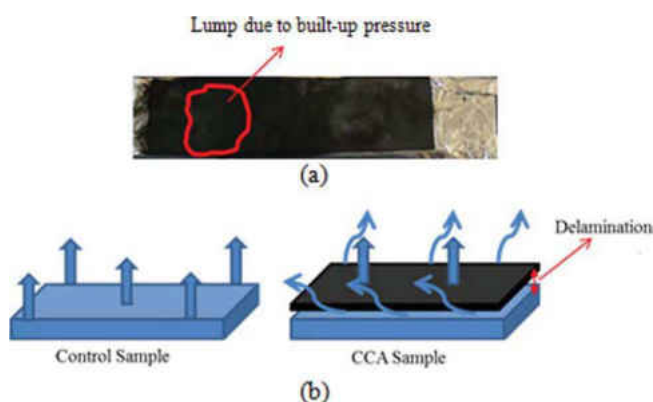


Figure 26 (a) The built-up pressure beneath a nanopaper results in the delamination and (b) the mechanism of permeability-related ignition (arrows indicate the decomposed fuel).

Since we expect the protective char to be formed at the early stage, the ignition time of the paper-coated samples is shorter than the control samples, as shown in Figure 25, and the first PHRR occurs when the samples catch fire. The shortened ignition time of CCA serial samples is attributed to high content of carbon particles in the hybrid nanopaper, which easily absorb energy and conduct heat. The reason for the first peaks (or ignition) in HRR curves of the CCA serial samples, besides the effect of high carbon content, could also be attributed to

the extremely low permeability, as mentioned in experimental section of this study, which results in the pressure (lump in Figure 26(a)) being built up between nanopaper and underlying structure. Consequently, the delamination of nanopapers occurs and the gas bursting out from the gap reaches the critical fuel concentration value that eventually leads to the ignition (as shown in Figure 26 (b)). Therefore, the peak occurs due to the large amount of newly-freed fuel igniting.

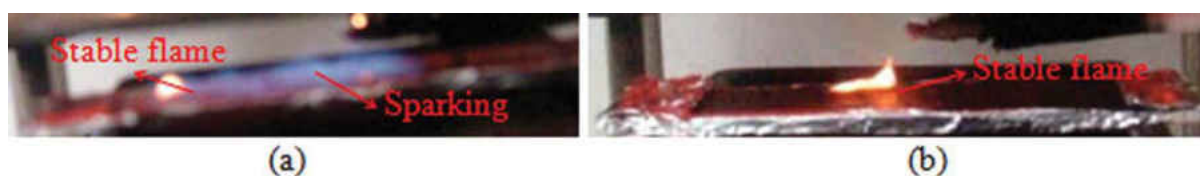


Figure 27 Flame patterns on the surfaces of the samples immediately after ignition. (a) control sample and (b) nanopaper-coated sample.

When the samples continuously burn, the resin within the nanopaper will be consumed up, and the protective char layer forms. Then, since the flame is maintained by the fuel that comes from the underlying polymer decomposition, the permeability of the nanopaper affects the long term HRR, *i.e.* the lower the permeability, the less the fuel pass through the protective layer, thus the lower the HRR. This is indicated as a dramatic drop in the HRR immediately after the first peak, then a relatively low HRR maintained after the drop. As shown in Figure 27(a), the lack in protection for the control sample leads to a large sparking area appears before and immediately after the ignition, which is barely observed with the sample coated with the nanopaper (Figure. 27(b)). The large sparking area of the control sample indicates that large amount of fuel present. It is important to note that despite

the HRR of the paper-coated sample being lower than the control sample, the THR of the three groups of samples are similar (about 57MJ/m^2) which indicates that the small quantity of the hybrid nanopaper does not affect the overall heat release of the material and a large amount of traditional fire retardants is indispensable if attempting to lower the value and achieve V-0 rating in the UL-94 test [146] [149].

The CCA type of nanopaper has much lower permeability than the CXA nanopaper, which causes the relatively lower HRR (less fuel penetrates the coating) during the first peak period and the lump of the nanopaper (Figure 26 (a)). However, the HRR of the CCA samples becomes much higher than the CXA samples after that. This phenomenon can be attributed to the complete detachment of the coating from the samples coated with the CCA papers. When the coating is detached from the underlying glass fiber mat, the barrier effect of the coating will be compromised. As evidenced by Figure 28, the CCA coating has already detached from the underlying glass fiber mat after cone calorimeter test, while the CXA paper is still attached to the 1st layer of the glass fiber mat. Furthermore, when there is no coating applied to the control sample, all the polymer matrix is completely burnt without turning into char, leaving the white original glass fiber mats behind. On the other hand, for the paper-coated samples, the glass fiber mats have caught more char as the coating stopped the degraded fuel to feed the surface flame during the combustion process.

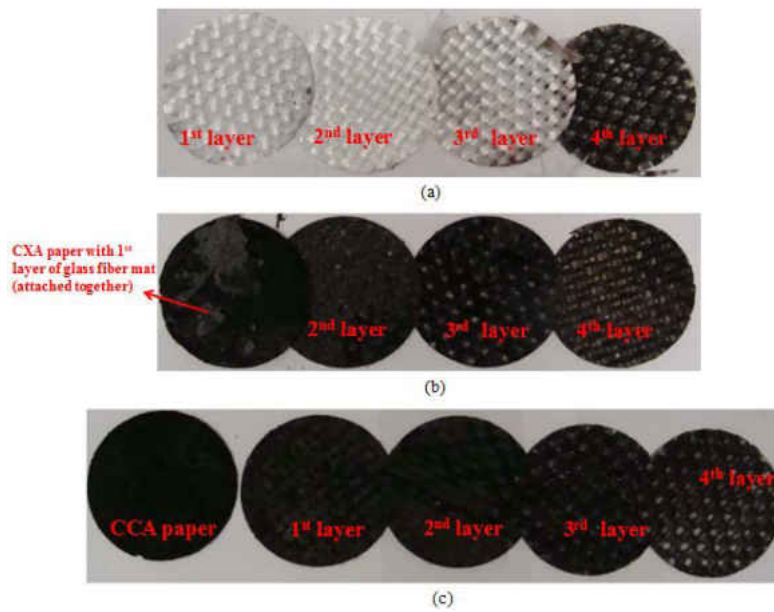


Figure 28 Char materials after the cone calorimeter test (first layer is more close to the heat flux than successive layers). (a) control sample; (b) CXA sample; and (c) CCA sample.

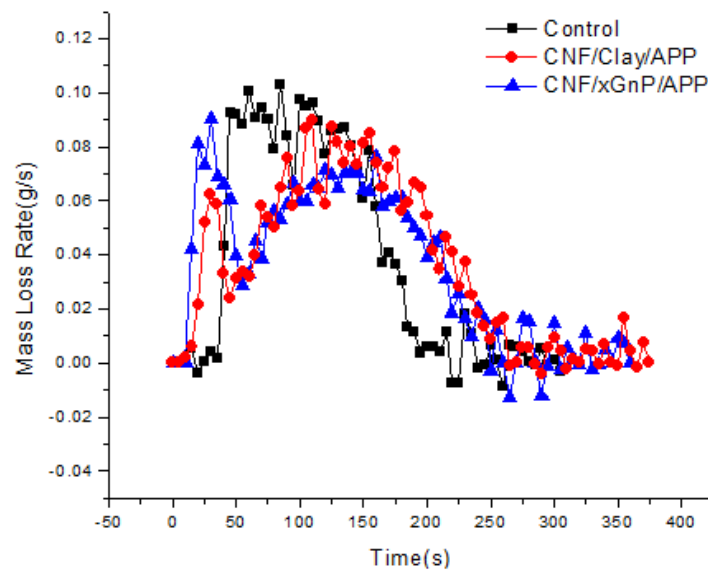


Figure 29 Mass loss rate of the samples.

Figure 29 shows the mass loss rate of the composite samples. The curves closely follow the HRR curves, *i.e.* the moment of the highest rate of mass loss is the same time when PHRR appears. Within the first 50s the mass loss rate of the paper-coated sample

increases and then decreases dramatically. The phenomenon suggests that the protective char layer has effectively lowered the available decomposed fuel to feed the flame.

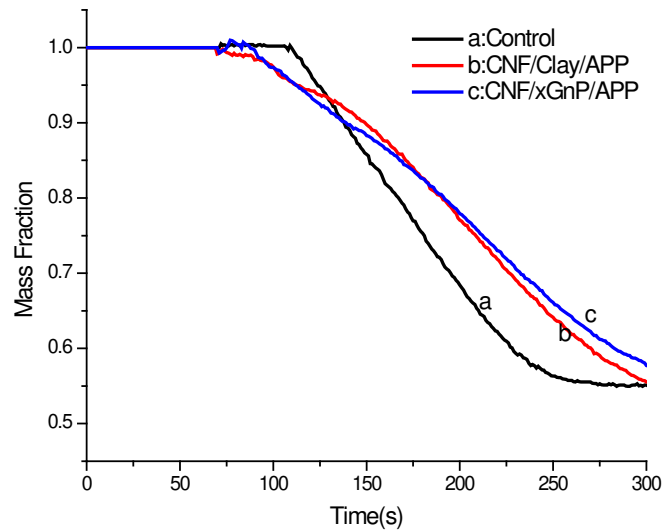


Figure 30 Remaining mass of the samples during the cone calorimeter test.

Figure 30 shows the change of the remaining mass of the samples, while they are exposed to heat flux. The mass ratios are calculated from normalizing the mass of the samples during the test by their initial weight. The hybrid nanopapers protect the samples in fire scenario by means of retaining the weight of samples. It can be seen that the mass of paper-coated samples begins to drop earlier than the control sample due to the reduced ignition time. However, since these samples are well protected by the nanopaper, the decrease in mass is much slower than the control samples.

Thermal stability

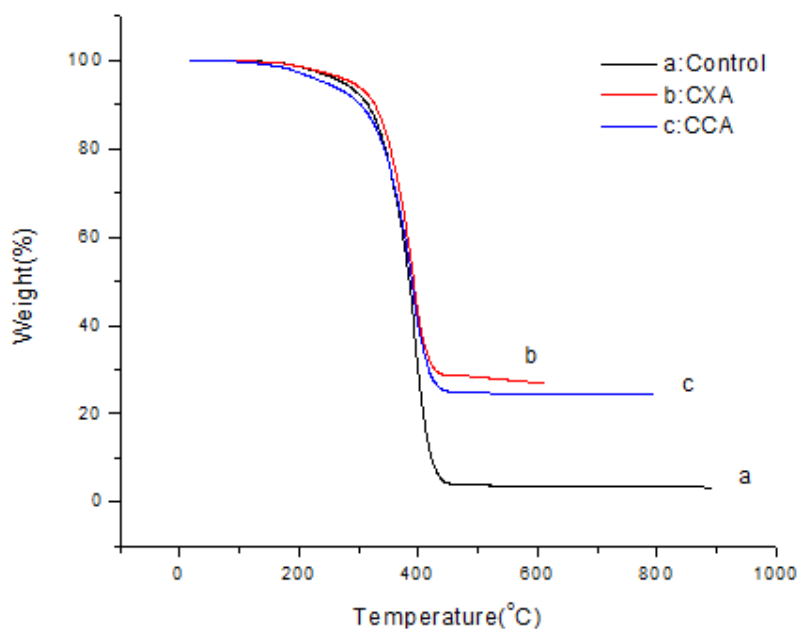


Figure 31 TGA results of the samples.

The thermal stability of the hybrid nanopapers is one of the important factors that affect the fire performance of the nanocomposites. TGA is the most widely used technique to evaluate the thermal stability of various polymer composites. As shown in Figure 31 and Table 8, the temperatures at 5% weight loss, which are defined as the initial decomposition temperatures, for the Control, CXA and CCA samples are 274°C, 289°C, and 242°C, respectively. The residual at 600°C for the above three samples are 3.65%, 27.1%, and 24.53%, respectively. Therefore, the incorporation of nanopaper into resin results in very high percentage of char yielding, which can be attributed to the high thermal stability of the CNF and xGnP particles. Compare to the CCA sample, the higher initial decomposition temperature and char residues for the CXA sample can be attributed to the fact that the

layered graphite can prevent the oxygen from diffusing into the substrate to decompose the polyester resin. And the resultant high degradation temperature stimulates the formation of the intumescent char due to the existence of APP. However, for the CCA sample, besides the positive effect due to the layered structure of clay, an ablative reassembling of the silicate layers from clay can hinder NH_3 from swelling, which has a negative effect on the formation of the intumescent char [150]. It can be seen that all the samples seem to have the same decomposition rate during the major mass loss period (300-450°C). However, if one considers the fact that CNF and xGnP particles are very stable (*i.e.* the exaggerated denominator for the decomposition rate of resin that containing hybrid nanopaper), it is reasonable to conclude that the introduction of hybrid nanopaper indeed increases the decomposition rate of resin which, also explains why the paper-coated sample has shorter ignition time.

Table 8 Summary of thermal stability of the samples.

TGA sample ID	$T_{-5\text{wt}\%}$ (°C)	Char (wt%) @ 600°C
Control	274	3.7
CCA	242	24.5
CXA	289	27.1

Post-fire mechanical properties

Since the samples exposed to heat flux for more than 150 s delaminated and their mechanical resistances were very low, the mechanical tests were only conducted for the samples with exposure times of 0s, 20s, 60s, 100s, and 150s. The post-fire mechanical

properties of these composite samples are shown in Figure 32.

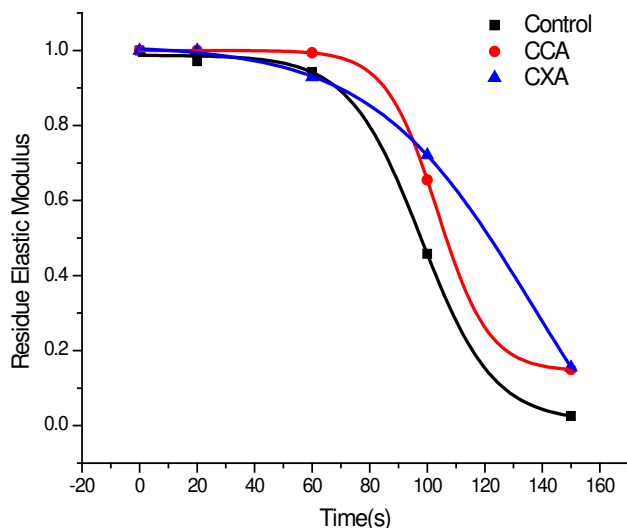


Figure 32 Residual elastic modulus of the samples with different exposure times.

It can be seen that the decrease rate in elastic modulus of the samples coated with hybrid nanopapers is lower than the control sample, both at the early stage (before 100s) and through overall period. The reductions in elastic modulus before 100s for the Control, CCA and CXA samples are 54%, 35%, and 25%, respectively, indicating the samples coated with hybrid nanopapers exhibit more than 20% improvement in mechanical resistance during the early stage of combustion. The greater improvement in the CXA samples can be attributed to the fact that they have remarkably low heat release rate during the major decomposition period, as shown in Figure 25. The overall decrease in elastic modulus for the Control, CCA, and CXA samples are 97%, 85%, and 84%, respectively. The curves that connect the data points were generated by Boltzmann Fit.

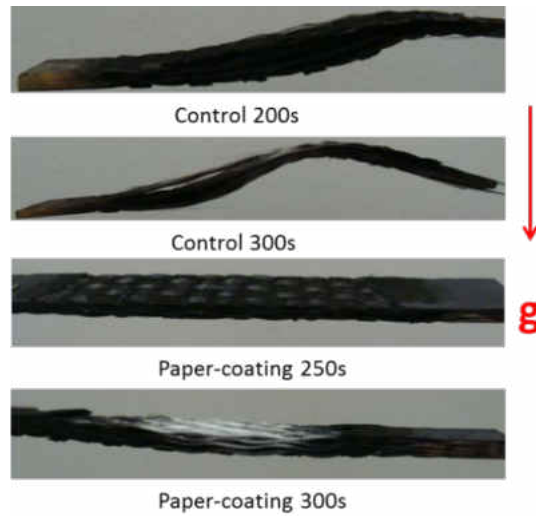


Figure 33 Comparison of the self weight-sustaining ability.

Figure 33 shows the mechanical resistance of the samples with exposure time of more than 150s. As shown in Figure 33, the control sample cannot sustain its own weight after an exposure time of 200s, while the samples coated with the nanopapers can sustain their own weight even after 300s of exposure. The observation confirms that the hybrid nanopapers have effectively retained the mechanical properties of PMCs during fire scenario. Furthermore, even though the paper-coated samples are completely turned into char, the self-weight sustaining ability indicates that the samples still have mechanical resistance. Therefore, one cannot claim that the charred layer has no mechanical resistance.

Morphologies of the nanopapers and char materials

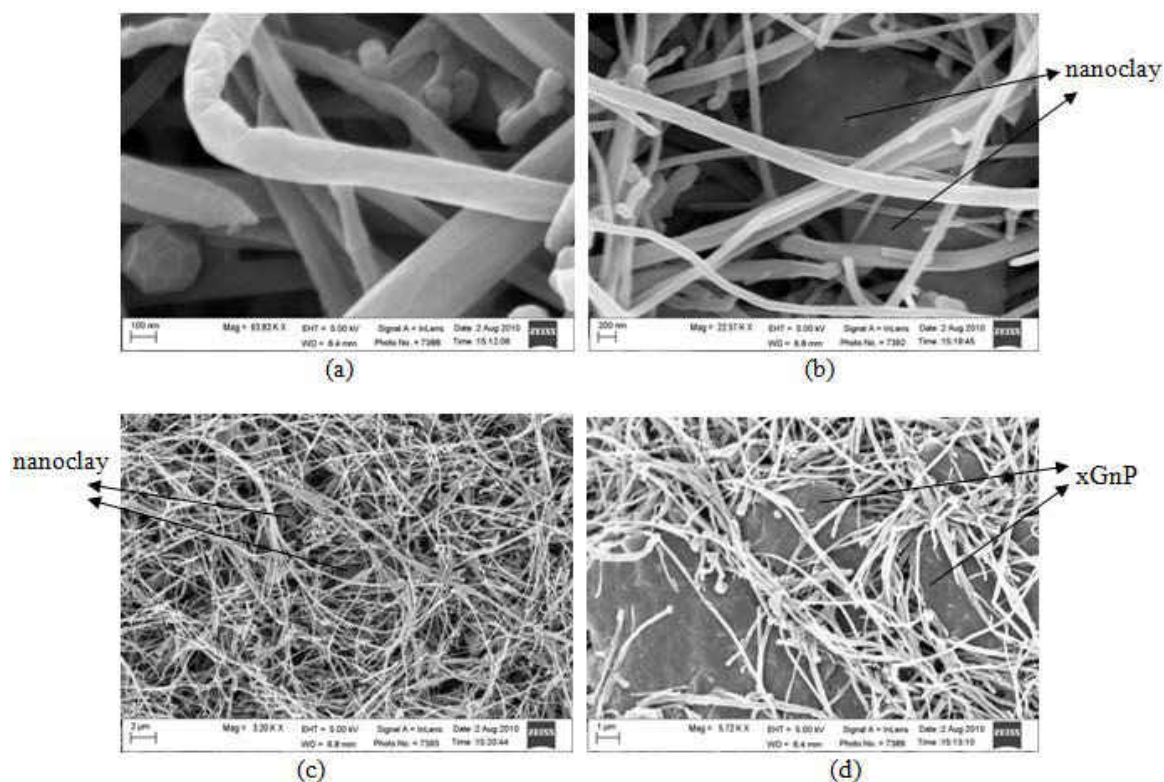


Figure 34 Hybrid nanopapers. (a) morphology of nanofibers; (b) nanoparticles within the nanofiber networks; (c) CNF/Clay/APP hybrid nanopaper; (d) CNF/Clay/xGnP hybrid nanopaper.

Figure 34 (a) to (d) show the morphologies of the nanofibers and hybrid nanopapers with the scale bar of 100nm, 200nm, 2μm, and 1μm, respectively. As shown in Figure 34 (a), nanofibers are entangled with each other and the average diameter of nanofibers is about 80nm. Figure 34 (b) shows that the particles fit within the network structure of nanofibers so that the permeability of the nanopaper will be reduced. The morphology of hybrid nanopapers show in Figure 34 (c) and (d) indicate that the nanofibers and particles are well dispersed without aggregation.

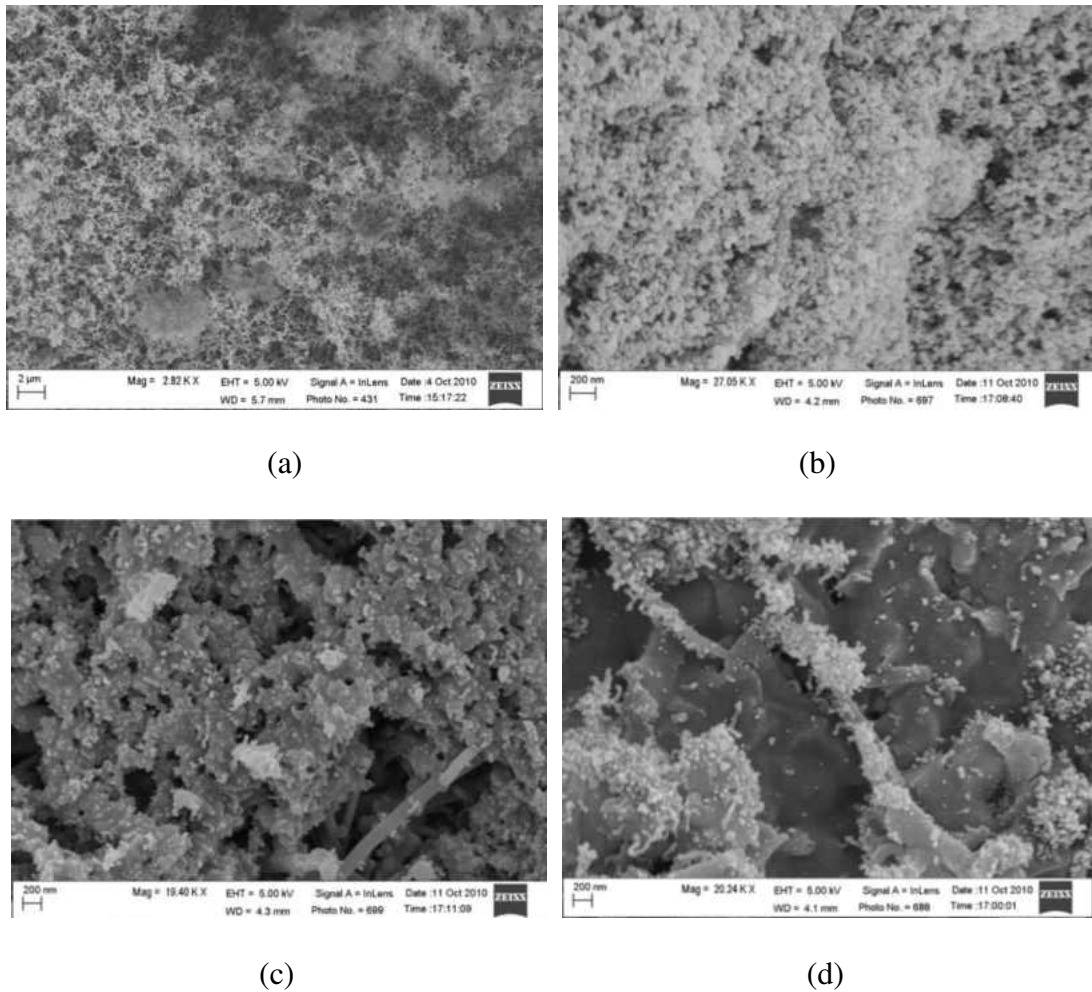


Figure 35 Morphologies of different types of char. (a) top surface char structure of all samples; (b) back surface char structure of both types of nanopapers; (c) and (d) back surface char structure of CCA nanopaper.

Figure 35 shows the morphology of different types of char obtained from the samples. The scale bar for the first image is 2 μ m and for the rest of images is 200nm. The char indicated in Figure 35 (a) is the only type of char that appeared in the top surfaces of all the samples. It comes from the deposition of burnt gas and is very loose. Figure 35 (b) shows the type of char that appears in both the back surfaces of the CXA and CCA nanopapers. Figure 35 (c) and (d) show the types of char that appear only in the back surfaces of the CCA nanopapers. Type (c) and (d) are more compact than type (b) char, which is formed due to the

low permeability of the CCA nanopapers; the compact morphology of the char also explains why the PMCs samples coated with the CCA nanopaper tends to build up pressure underneath the coating.

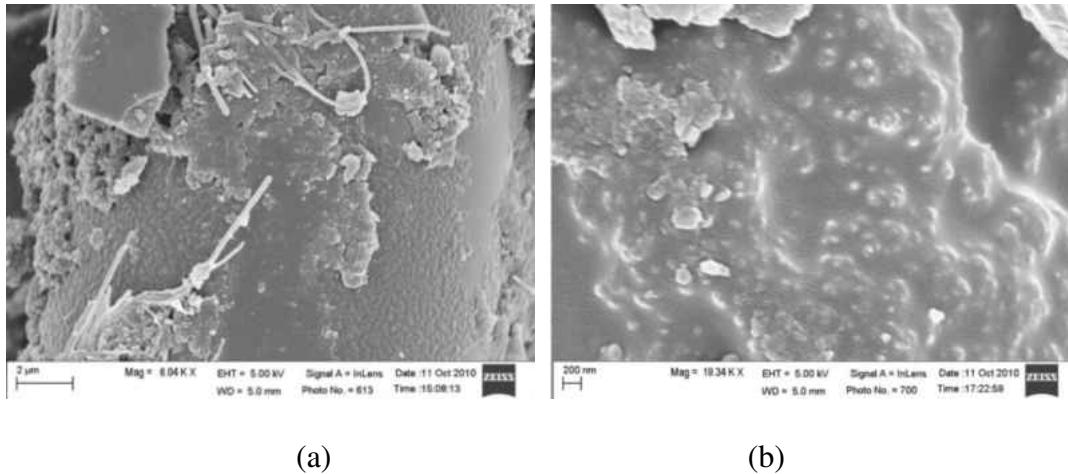


Figure 36 Morphologies of the glass fibers of the samples coated with hybrid nanopapers. (a) 2 μ m, (b) 200nm.

Figure 36 (a) and (b) shows the morphology of glass fiber after the paper-coated sample is exposed to heat flux for 200s. It can be seen that the un-decomposed resin is still attached to the surface of glass fiber, which retains the mechanical properties of the sample. It is reasonable to conclude that there is a direct proportional relationship between the amount of un-decomposed resin retention and the elastic modulus of the sample, and by extension, the efficiency of the nanopaper.

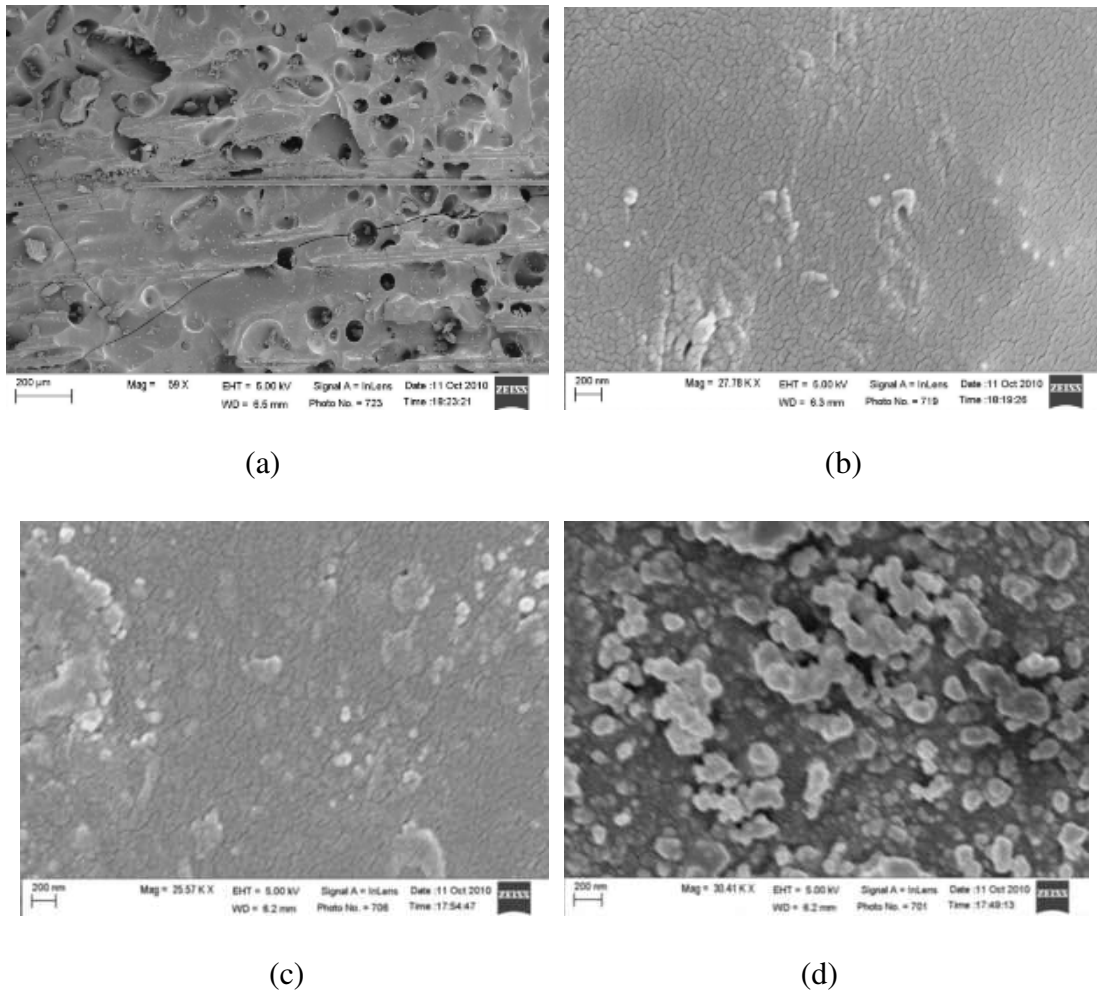


Figure 37 Morphologies of the resin. (a) back of the sample with the exposure time of 150s and scale bar of 200µm; (b) back of the sample with the exposure time of 150s and scale bar of 200nm; (c) virgin resin with the scale bar of 200nm; (d) front surface of the control sample with an ignition time of less than 5s.

Figure 37 shows the morphology of virgin, degraded, and burnt resin. It is interesting to note that even though the back of the PMCs sample has been severely degraded, the microscopic structure of the resin is similar to the virgin resin and is quite different from the resin that is even slightly burnt.

4.3.2. Conclusions

Hybrid nanopapers containing CNF/Clay/APP or CNF/xGnP/APP were fabricated and coated onto the surface of PMCs. Their efficiency in improving the fire resistance of PMCs was evaluated. The test results indicate that the hybrid nanopaper has effectively reduced the heat release rate and mass loss of the composite samples. The peak heat release rate (PHRR) of the CCA and CXA samples in the major decomposition period are 23% and 34% lower than the control samples. The time to reach this PHRR for the CCA and CXA samples is roughly 125% longer than the control samples. However, even though the CCA nanopaper has much lower permeability than the CXA paper, this is not necessarily preferable for fire retardancy due to the fact that the CCA paper tends to detach from the underlying structure, because of the built-up pressure underneath the nanopaper. Although the sample coated with the CCA paper has lower HRR than the CXA during the initial period of combustion, the CXA sample exhibit a lower HRR in the most of the combustion period.

Bending tests indicate the post-fire mechanical properties of PMCs have been enhanced with coating the hybrid nanopapers onto the surface. As a result, the samples coated with hybrid nanopapers exhibited more than 20% improvement in mechanical resistance during the early stage of combustion. The overall decrease in elastic modulus for the Control, CCA, and CXA samples are 97%, 85%, and 84%, respectively. The SEM images of the char materials suggest that the compact char under the nanopapers results in an improvement in fire performance and post-fire mechanical properties.

4.4. Fire Retardant Performance Evaluation of the Glass Fiber Reinforced Polyester Coated with the xGnP/CNF/APP Nanopaper Subject to Various Heat Fluxes

The nanopaper that was composed by xGnP, CNF, and APP with a weight ratio of xGnP/CNF/APP equaled 3/1/9 was selected for experimental study, because of its relatively good flame resistance performance (as discussed in section 4.2) and bonding with underlying PMCs (as discussed section 4.3). To gain deeper insight into the combustion process of the samples for future modeling, and to understand the flame retardancy mechanism which provides guidelines for material design, PMCs coated with 3xGnP/1CNF/9APP went through extensive testing. The flammability of the nanocomposites was thoroughly investigated by exposing them to different levels of heat fluxes. In addition, the temperature profiles were recorded and the post-fire flexural moduli of the samples were also determined.

The materials and sample preparations were discussed in the previous sections. Nevertheless, it was found that the APP powders run the risk of decomposing into smaller particles during sonication, potentially preventing their inclusion in the nanopaper during filtration. Instead of directly mixing them with CNF and xGnP in the sonication process, they were mixed into the polymer matrix using a mechanical shear mixer (Model 50002-30, manufactured by Cole-Parmer Instrument Company, Illinois, USA) at 1400rpm for 4 hours, and then the mixture was brushed onto the back surface of the dry paper. The amount of APP was calculated based on the weight of nanoparticles used for the nanopaper and the designated weight ratios shown in Table 9. The weight ratio of the paste for APP and resin was 1 to 4 in order to balance the viscosity of the paste and the amount of resin that had been

used.

Table 9 Composition of the hybrid nanopapers and nanocomposites.

Nanocomposites sample ID	Contents (wt %)			Weight ratios of particles in the nanopaper
	GF	Resin	Nanopaper	
3xGnP/1CNF/9APP	51.0	46.0	3.0	xGnP/CNF/APP=3/1/9

Similar to the previous sections, the samples were characterized by cone calorimeter test and three-point bending test. The difference in this section was that the samples were subjected to various heat fluxes, including 25, 35, 50, 75, and 100kW/m². The heat exposure time of the samples for the three-point bending test is showed in Table 10.

Table 10 Heat treatment for the post-fire three-point bending test.

Applied Heat	
Flux (kW/m ²)	Exposure Times (s)
25	0, 120, 180, 240, 300
35	0, 60, 100, 140, 180
50	0, 40, 80, 120, 150
75	0, 20, 50, 75, 100
100	0, 15, 40, 70, 100

In addition to that, the temperature histories were recorded for the paper coated samples and the control samples, as they were exposed to varied heat fluxes in cone calorimeter. The thermocouples used in this study were the K-type, GG-K-24-SLE (obtained from Omega Engineering Inc.) with a diameter of 0.51mm, and a maximum temperature measurement of 1250°C, and an error of ±0.4%. The temperature data was recorded at one

second intervals using the NI USB-9213 data acquisition system and NI Labview. Both were developed by National Instruments. As shown in Figure 38, the side and bottom of the samples were insulated. The temperature profiles of the middle and back surface of the samples were recorded using embedded thermocouples, as shown in Figure 38 (a). The size of these samples was the same as the size of the cone calorimeter test samples. The applied heat fluxes also included 25, 35, 50, 75, and 100kw/m².

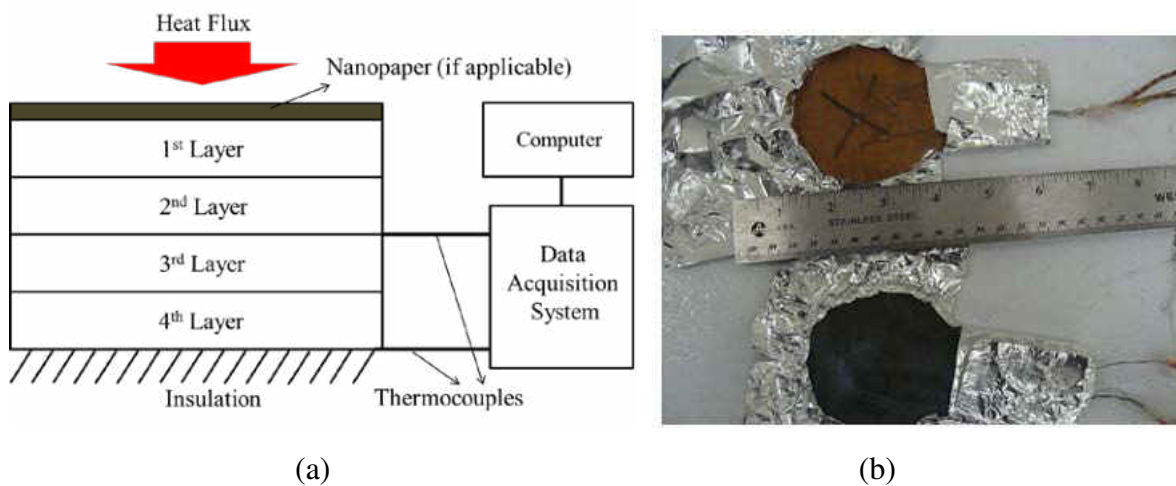


Figure 38 (a) Temperature measurement setup and (b) actual samples.

4.4.1. Results and discussion

Cone calorimeter test results

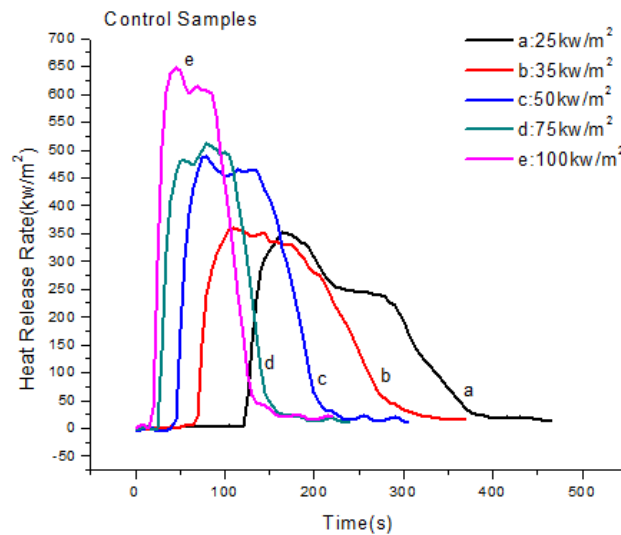


Figure 39 Heat release rate curves of the control samples subjected to various heat fluxes.

Figure 39 and Table 11 show the HRR curves and summarized cone calorimeter test data for the control samples subjected to varying heat fluxes, respectively. From these, it is observed that the HRR and PHRR gradually increase with the increase of applied external heat fluxes. According to Schartel and Hull [140], the HRR curves shown in Figure 39 suggest that the control samples might belong to the “thermally thick charring” type of samples. However, the curves related to a higher intensity external heat flux, including 50, 75, and 100kw/m^2 , do not strictly follow the characteristic of “thermally thick charring”, in which the HRR initially hits a maximum value, and as the char layer thickens, the HRR decreases. In fact, it appears that the char produced by polyester decomposition that was observed on the surface of the sample when it was subjected to 25 and 35kw/m^2 heat fluxes

disappears when the sample is exposed to 50, 75, and 100kW/m² heat fluxes, as determined by a closer examination of the residual materials after the cone calorimeter test (Figure 40). The phenomenon indicates that the “char” is unstable and is more like intermediates, which eventually will be completely decomposed provided that the applied heat flux is strong enough. In fact, Lattimer *et al* also claimed that the remaining char in the char/fiber matrix after the completion of the resin decomposition process will oxidize in the presence of oxygen and sufficiently high temperature, leaving only the reinforced fiber for composites [151].

Table 11 Summary of cone calorimeter test results for the control samples.

Applied heat flux (kW/m ²)	Time to ignition (s)	Initial weights (g)	THR (MJ/m ²)	PHRR (kW/m ²)	Time to PHRR (s)	Char Yield (%)
25	116	25	57	350	170	6
35	64	25	57	361	110	3
50	39	26	58	488	80	1
75	21	24	49	510	80	-1
100	14	25	54	648	45	-5

As expected, Table 11 shows that when the applied heat flux increases, time to ignition (TTI), time to PHRR, and char yield decreases. The negative values of char yield (CY) in the table arise from the definition of CY which is calculated by excluding the influence of the weight of glass fiber that is considered to be very stable during combustion process (see Equation 4-2). Therefore, the negative values of CY would indicate that even the glass fibers are severely damaged and degraded for the control samples when they are

exposed to high heat flux (75 and 100kw/m²). These damaged glass fiber mats are clearly observed and shown in Figure 40.

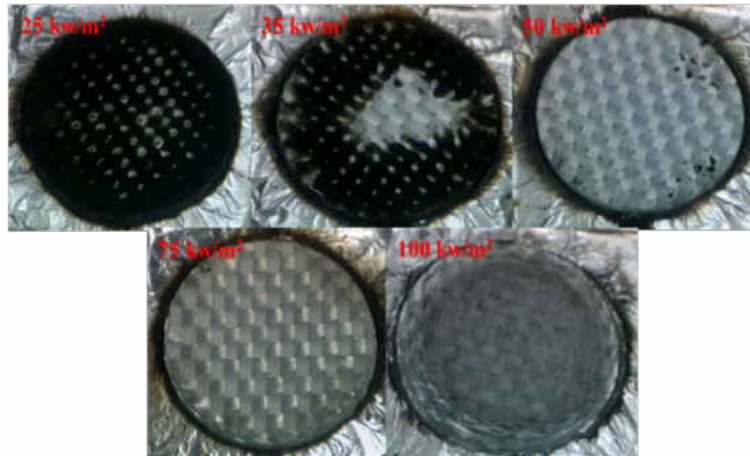


Figure 40 Residues of the control samples after the cone calorimeter test.

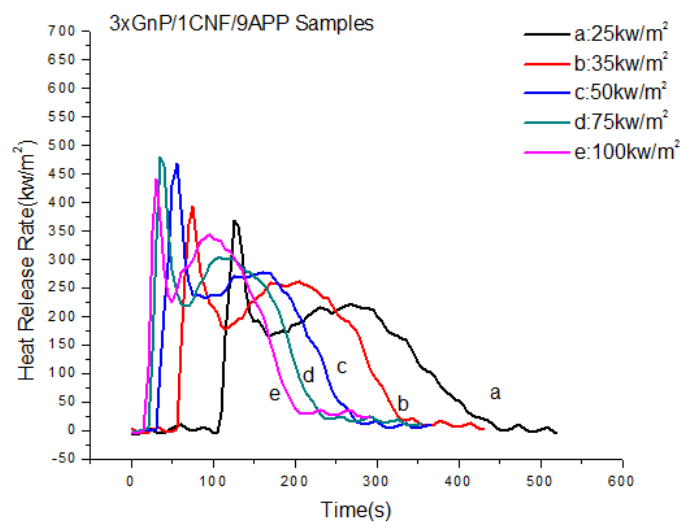


Figure 41 Heat release rate curves of the paper-coated samples subjected to various heat fluxes.

The HRR curves and cone test data for the composites coated with 3xGnP/1CNF/9APP nanopaper are shown in Figure 41 and Table 12, respectively. The HRR

curves in Figure 41 suggest that the value of the 1st PHRR increases when the applied heat flux is increased, with this trend holding to a heat flux of 50kw/m². After that point, the 1st PHRR appears to be independent of heat flux, which exhibits a “thermally thin sample” characteristic [140]. Such a result is reasonable when considering that the 1st PHRR is the result of the ignition of a very thin coating layer of resin that remained in the nanopaper. A probable explanation is that since the weight of resin within the coating layer is the same for all of the paper coated samples, the increase of heat flux results in the increase of the 1st PHRR of the paper coated sample at a low heat flux until there is not enough resin within the coating layer for further degradation at a high heat flux. This results in a phenomenon that the 1st PHRR is independent of heat flux. This aside, the behavior for time to ignition, 1st PHRR, 2nd PHRR, and char yield of these samples is otherwise unremarkable. When compared with Figure 40 and Table 11, however, the yield of char for the paper coated sample is much higher than that of the control sample, likely due to the impact of the protective coating. The 2nd PHRRs for the paper coated samples are substantially lower than the PHRR of the control sample.

Additionally, the paper coated samples as a whole behave as “thick charring with additional peak at the end of burning” materials. This is shown by the 2nd PHRR occurring at the end of the test [140]. The reason for the occurrence of the 2nd PHRR can be attributed to either, the pyrolysis zone approaching the insulation fabric of the sample holder, which prevents heat from transferring to the surrounding environment, or to the char cracking, with

either occurring near the end of the test [140].

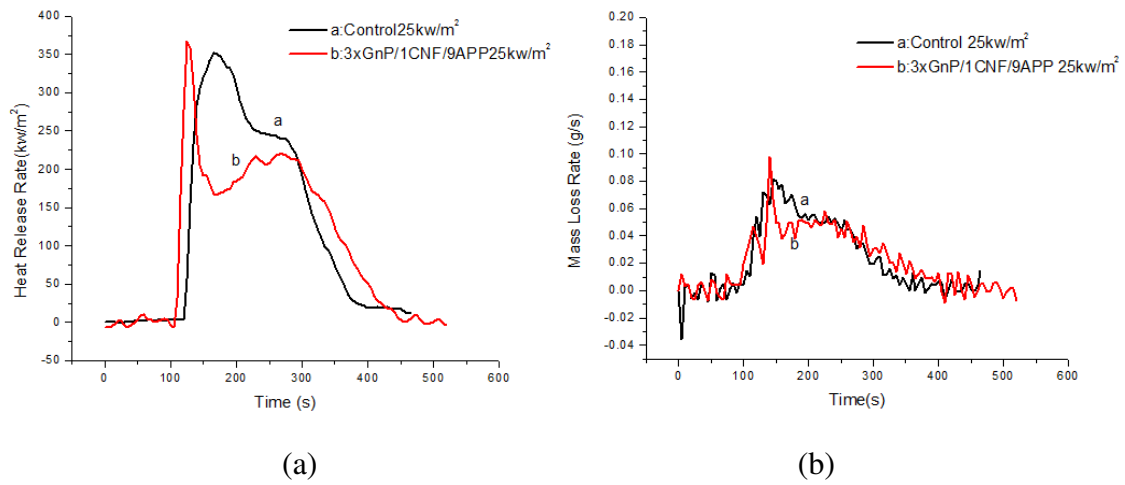


Figure 42 (a) Heat release rate and (b) mass loss rate of the two groups of samples subjected to low heat flux (25kw/m^2).

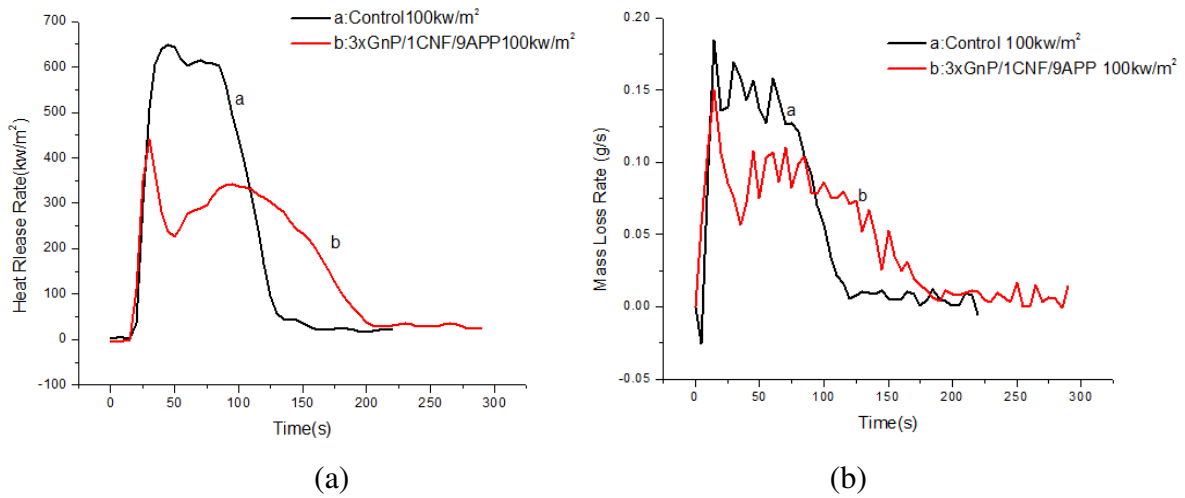


Figure 43 (a) Heat release rate and (b) mass loss rate of the two groups of samples subjected to high heat flux (100kw/m^2).

Figure 42 and 43 show the HRR curves of the control and paper coated samples under low and high intensity heat flux, respectively. It is evident that the flame retardant properties

Table 12 Summary of cone calorimeter test results for the 3xGnP/1CNF/9APP samples.

Applied heat flux (kW/m ²)	Time to ignition (s)	Initial weight (g)	THR (MJ/m ²)	1st PHRR (kW/m ²)	Time to 1st PHRR (s)	2nd PHRR (kW/m ²)	Time to 2nd PHRR (s)	Char Yield (%)
25	110	28	55	362	155	220	230	14
35	68	28	55	393	75	260	205	12
50	32	28	54	468	55	273	170	10
75	18	28	51	481	35	302	120	5
100	12	28	49	442	30	343	95	4

of the paper are improved when the sample is exposed to a higher intensity of heat flux, indicating its potential for the thermal protection system (TPS) of space probes. The 1st and 2nd PHRR of the paper coated sample are more than 32% and 47% lower than the PHRR of the control sample, respectively, when samples of the same makeup are exposed to 100kW/m² heat flux. Since the protective layer has already formed after the resin in the coating layer is consumed, the 2nd PHRR does not exhibit a substantial increase proportional to the heat flux. Due to the formation of protective char layer at the early stage of combustion, as shown in Figure 42 (a) and 43 (a), immediately following the 1st PHRR of the paper coated samples there is a dramatic decrease in HRR change. The 2nd PHRR then increases slowly compared to the change in heat flux, even when it is increased to 100kW/m². For the control sample, since there is no protective layer being formed during combustion process, the HRR dramatically increases with the increase of heat flux, especially at high intensity. Thus, the difference in HRR between these two groups of samples becomes increasingly evident and the flame retardant efficiency of the nanopaper is better demonstrated at higher heat flux intensity.

As discussed in the Introduction section, the nanopaper is designed to serve as a pre-existing char layer and to prompt the formation of protective char. As shown in Tables 11 and 12, the ignition time of the paper-coated samples is slightly shorter than the control samples. The shortened ignition time of paper coated samples is attributed to high content of carbon particles in the nanopaper, as they easily absorb heat. The 1st PHRR of the paper

coated sample is relatively higher than its 2nd PHRR, except the samples subjected to 25 and 35 kW/m² heat flux, they are generally still lower than the PHRRs of the control samples.

Figure 42(b) and Figure 43(b) show the mass loss rate of the composite samples. It can be seen that the curves closely follow the evolution of HRR curves, *i.e.* the moment of the highest rate of mass loss is the same time when PHRR appears. This result confirms Morgan's statement that regardless of the different phenomena occurring when one tries to reduce the flammability of polymers by incorporating nanofillers, the HRR is reduced by inhibiting the mass loss rate [152].

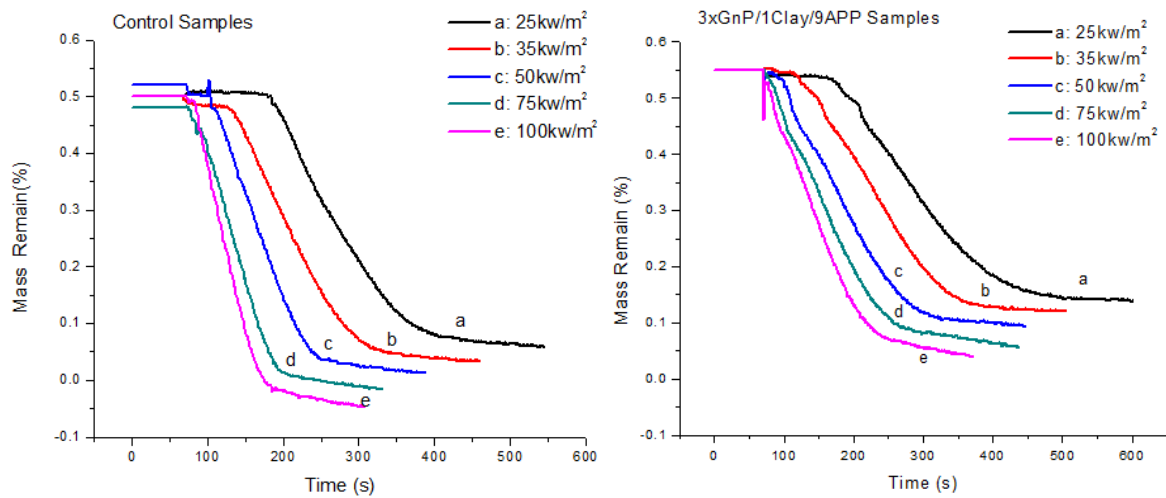


Figure 44 Mass remains of the samples during the cone calorimeter test.

Figure 44 shows the evolution of remaining mass of the samples during the cone calorimeter test. As shown in this figure, these curves indicate that there are three stages of decomposition for the polyester resin [152]. It can be seen for all the samples, the mass loss rate is faster and char yield is lower when they are exposed to a higher heat flux. For the

control samples, the remaining mass at the end of the test at high intensity of heat flux becomes negative due to the damage to glass fiber mats, as previously discussed. In contrast, the paper coated samples are well protected by the coatings, and the rate of decrease in mass is much lower than that of the control samples. With this in mind, it can be said that Figure 44 suggests that the nanopapers protect the samples in a fire scenario by means of retaining the weight of samples due to the low permeability of the nanopapers, which contain the planar structure nanoparticles-xGnP. Considering the reduced HRR curves for the paper coated samples, the result confirms that HRR reduction was indeed achieved by inhibiting the mass loss rate [153]. Additionally, the ability to prevent the mass loss is also critical for retaining the mechanical properties of the composites which will be addressed in the following discussions.

Temperature profiles of the composites under fire condition

To gain deeper insights into the combustion process of the samples for future modeling, and to understand the flame retardancy mechanism for material design, it is crucial to study the evolution of temperatures at different locations in the samples during the combustion process. Figure 45 shows the middle and back temperature profiles of the samples when they are subjected to varying intensities of external heat. Keeping in mind that the pyrolysis zone for glass fiber reinforced polyester is roughly from 250°C to 400°C [152], the temperature profiles can be divided into three regions, as shown in Figure 45. The reason for increased temperature before the pyrolysis zone can be attributed wholly to heat

conduction. During the heat conduction period, the differences of the back surface temperature curves between the coated and uncoated samples in Figure 45 are very small. This would indicate the coating of a thin layer of nanopaper does not affect the overall thermal conductivity of the composites. The temperature differences of the middle surface of the samples are more obvious than that of the back surface. This was probably due to the imbedding of the thermal couple, which was not perfectly in the middle of the samples.

Within the pyrolysis zone, as shown in Figure 45, the temperature increases at a much lower rate than the previous heat conduction region. This is because the pyrolysis of the polymer and vaporization of the decomposition products are endothermic in nature, and the temperature increases at a lower rate in this region. Furthermore, by close examination of these temperature profiles, it is observed that the rate of temperature increase for the paper coated samples is slower than of that the uncoated samples. The differences in the temperature increase rate is much greater at higher temperatures and when exposed to higher heat flux as shown in Table 13. For example, the time for the paper coated sample to reach a middle surface temperature of 400°C at 25kW/m^2 (Figure 45(a) and Table 13) is delayed 40% compared to the control sample. This difference grows to 190% at 100kW/m^2 (Figure 45(e) and Table 13). As a result, the fire retardancy of the nanopaper is better revealed at higher heat fluxes. This is very likely due to a char layer which forms more quickly at higher heat fluxes, growing into the composite as the nanopaper slows down mass loss.

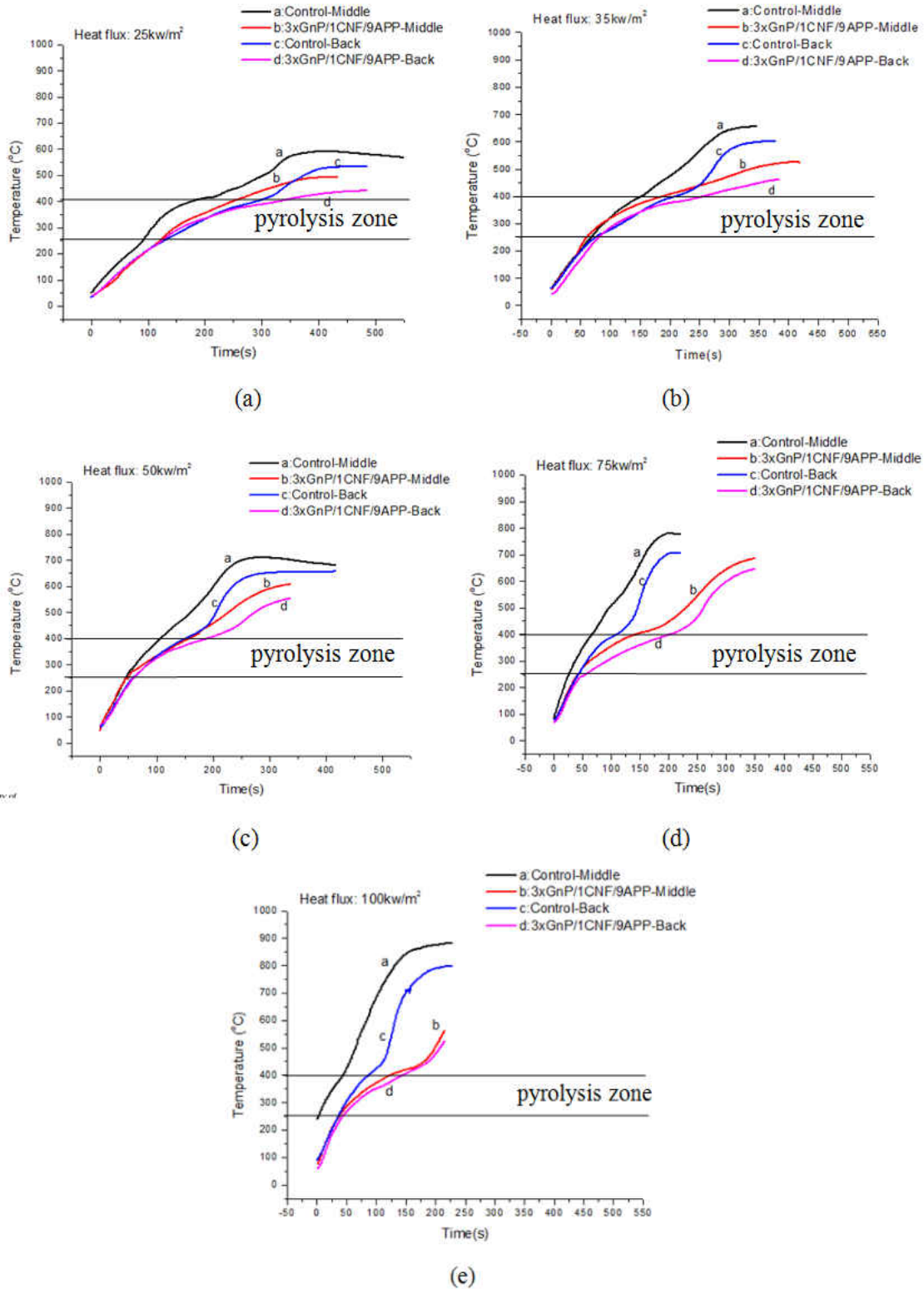


Figure 45 Temperature profiles of the samples subjected to various heat fluxes. (a) 25kw/m^2 ; (b) 35kw/m^2 ; (c) 50kw/m^2 ; (d) 75kw/m^2 ; (e) 100kw/m^2 .

Table 13 Time (seconds) to reach the critical temperatures for the samples.

		25kw/m ²		35kw/m ²		50kw/m ²		75kw/m ²		100kw/m ²	
		M	B	M	B	M	B	M	B	M	B
250°C	Control	90	126	69	70	49	60	26	44	3	36
	XCA	121	135	70	69	50	60	44	56	36	44
400°C	Control	179	282	152	212	105	148	66	108	45	87
	XCA	248	332	221	224	150	190	145	205	124	146

*In this table M, B, and XCA represent middle, back, and 3xGnP/1CNF/9APP, respectively.

Above the pyrolysis zone, all of the thermocouples for the control sample can be treated as free standing and they recorded the temperature evolution due to the heat conduction of the glass fiber mat, since there was no formation of char within the control samples. However, the thermocouples of the paper coated samples measure the temperature evolution within the char materials. Due to thermal barrier effect of the thick char layer, the temperature of the paper coated sample is much lower than that of the control sample in this region. For example, at 100kw/m² heat flux, the final temperature within the paper coated sample is approximately 280 °C lower than the control sample.

Post-fire flexural moduli

When composite materials are exposed to heat flux, the polymer matrices decompose, resulting in degradation in mechanical properties. The major degradation in mechanical properties usually occurs above the glass transition temperature of the polymer [154]. In this section, the mechanical degradation rate is evaluated using the normalized flexural moduli of the samples after they are exposed to varied heat flux with different times. They are calculated using Equation 4-3. It should be noted that when the samples are cooled to ambient

temperature, they tend to regain some of their mechanical properties [155]. Since the objective of this study is to evaluate the flame retardant performance of the nanopaper, and since the post-fire flexural moduli of the control and paper coated samples are compared under the same conditions, the effect of the above mechanical property recovering phenomenon can be neglected.

As shown in Table 14, the degradation rate of flexural moduli is faster at higher intensity of heat flux, for all these samples. However, the rate for the paper coated sample is much lower than that of the control sample. For example, when a sample is exposed to 25kW/m^2 heat flux for 240s, the flexural modulus of the control sample is almost completely depleted, while the paper coated sample retains half of its flexural modulus. Since the char yield, as shown in Table 12 and Figure 44, is very high for the paper coated samples, it is reasonable to conclude that there is a correlation between mass loss and flexural moduli depletion: the nanopaper coating can effectively protect the structural integrity of the underlying composites by retaining their mass under fire conditions.

Furthermore, an interesting phenomenon of the relationship between flexural moduli and the temperature can be obtained by comparing data in Table 13 and 14. As shown in Table 13, the time that the back surface of the control sample reaches 400°C for the 25, 35, 50, 75, and 100kW/m^2 heat fluxes is 282, 212, 148, 108, and 87 seconds, respectively. At this temperature, the polymer matrix has apparently been completely decomposed. The time that the control samples lost all their flexural moduli for the above heat fluxes is roughly 300, 180

Table 14 Normalized flexural moduli of the samples subjected to various heat fluxes with different exposure times.

Heat flux	Sample	Normalized flexural moduli (Exposure Times)				
25kw/m ²	Control	1 (0s)	0.90 (120s)	0.65 (180s)	0.08 (240s)	0 (300s)
	3xGnP/1CNF/9APP	1 (0s)	1 (120s)	0.99 (180s)	0.45 (240s)	0 (300s)
35kw/m ²	Control	1 (0s)	0.60 (60s)	0.45 (100s)	0.16 (140s)	0 (180s)
	3xGnP/1CNF/9APP	1 (0s)	0.70 (60s)	0.68 (100s)	0.35 (140s)	0.1 (180s)
50kw/m ²	Control	1 (0s)	0.56 (40s)	0.32 (80s)	0.04 (140s)	0 (150s)
	3xGnP/1CNF/9APP	1 (0s)	0.57 (40s)	0.47 (80s)	0.28 (140s)	0.03 (150s)
75kw/m ²	Control	1 (0s)	0.58 (20s)	0.34 (50s)	0.11 (75s)	0 (100s)
	3xGnP/1CNF/9APP	1 (0s)	0.59 (20s)	0.49 (50s)	0.38 (75s)	0.13 (100s)
100kw/m ²	Control	1 (0s)	0.57 (15s)	0.34 (40s)	0.09 (70s)	0 (100s)
	3xGnP/1CNF/9APP	1 (0s)	0.60 (15s)	0.59 (40s)	0.29 (70s)	0.06 (100s)

140, 100, and 70 seconds, respectively. This means that when the temperature of the back surface of the control sample reaches the upper limit of pyrolysis temperature of the polyester resin, the sample will lose all its flexural resistance. The same result is observable by examining the data of the paper coated sample in Table 13 and 14, and the only difference is that the time to reach the critical temperature has been prolonged due to the presence of the coating. It can be concluded that the nanopaper can also protect the composites by means of thermal barrier. It is also reasonable to treat the region that has passed by the upper limit line of pyrolysis zone as no mechanical resistance. This information is important for future post-fire mechanical modeling.

Morphologies of the nanopapers and char

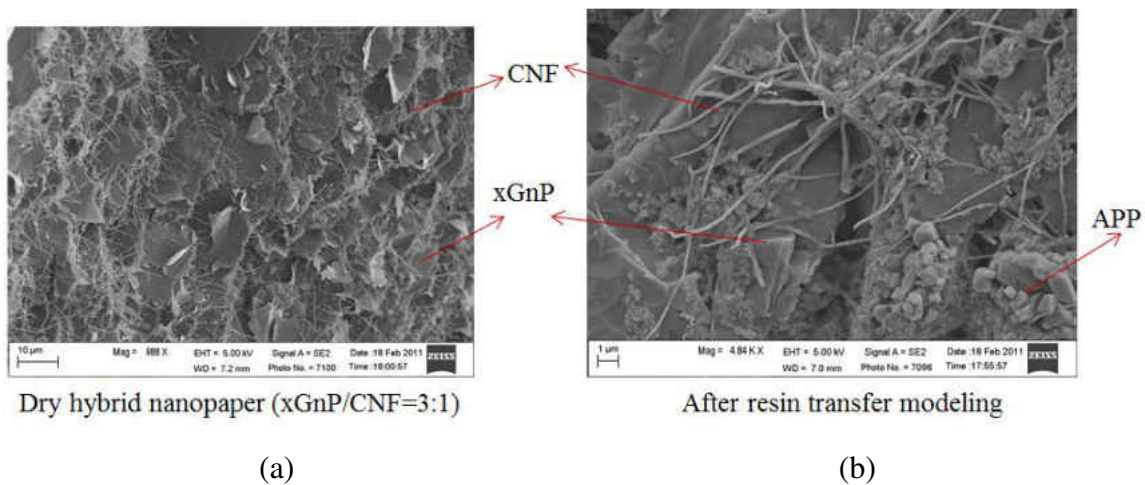


Figure 46 (a) Morphologies of the dry nanopaper and (b) the paper structure after resin transfer molding.

The morphologies of a nanopaper before and after coating onto the surface of PMCs are shown in Figure 46. The SEM images show that xGnP particles are well dispersed and

entangled within the CNF networks, and the APP particles are clearly observed after resin transfer molding. Since the CNF and xGnP particles are more thermally stable than the polyester resin, as indicated in Figure 46, the structure is stable and is expected to effectively prevent the mass loss of the underlying composite materials in a fire scenario by convoluting the path of the decomposed polymer (fuel) as discussed before.

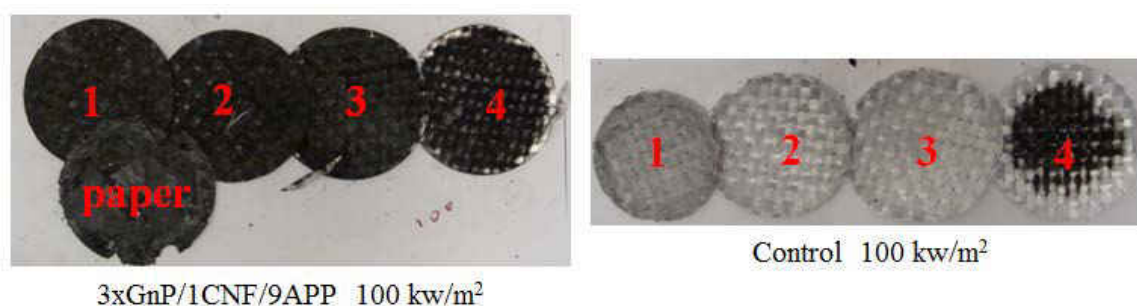


Figure 47 Morphologies of the residues of the samples that had been exposed to 100kW/m² heat flux.

Figure 47 shows the morphology of the glass fiber mats after the samples are exposed to 100kW/m² heat flux. The smaller number in the figure means the layer is closer to the heat source. It can be seen that for the control sample, even the glass fibers are severely damaged, while no obvious damage can be observed from the glass fibers of the paper coated sample. This indicates the excellent flame retardant efficiency of the nanopaper. Furthermore, the color of the upper layers is much darker than that the lower layers for the paper coated sample, as shown in Figure 47. In contrast, the bottom layer of the control sample is the darkest. Even the bottom layer of the paper coated sample is darker than that the bottom layer

of the control sample. Therefore, there is much more char material collected by the upper layers of the glass fiber mats in the paper coated samples, which also explains why the paper coated sample has better flame retardancy.

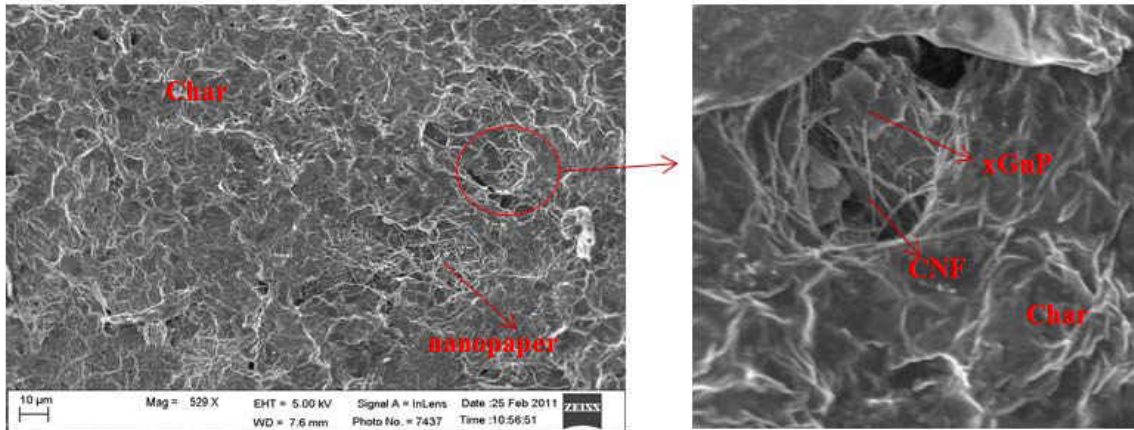


Figure 48 Char materials on the back surface of the hybrid nanopaper.

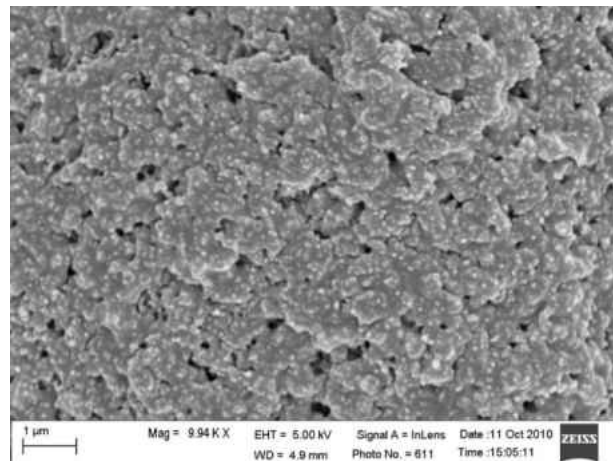


Figure 49 Char materials attached to the glass fibers of the control sample.

Figure 48 and Figure 49 show the SEM images of the char collected from paper coated sample and control sample, respectively. It can be seen that the char materials in the

back surface of the nanopaper are more compact than that the char materials of the control sample. Together with the relatively low permeability of the nanopaper, they can effectively reduce the rate of decomposition products (fuel) that feed the flame on the surface of the sample, thus enhancing the flame resistance of the composites.

4.4.2. Flame retardancy mechanism

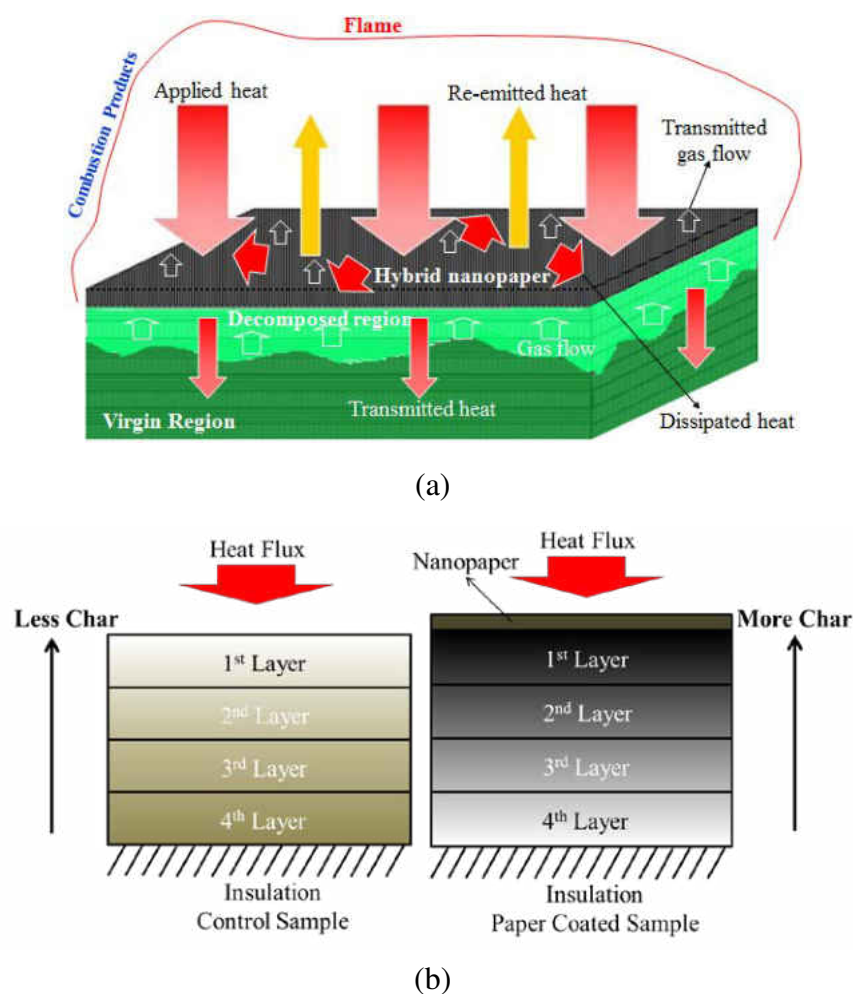


Figure 50 Flame retardancy mechanism.

Figure 50 is a sketch that shows the flame retardancy mechanism of the hybrid nanopaper coating. Under fire conditions, the polymer in the composites decomposes into

gases, which will evaporate. Due to the low permeability of surface coating, however, the gases are caught and aggregated on the upper layers of the sample as demonstrated by Figure 47. The direct result of this is decreased mass loss, less fuel to support the fire propagation, and a lower HRR. As the combustion process continues, a thicker char layer forms that in turn serves as a thermal barrier to further protect the underlying structure. In contrast, since there is no coating on the surface of the control sample to prevent the mass flow, the decomposed products (or fuel) directly enter into the combustion zone, stimulating flame development, which in turn accelerates the pyrolysis of the intermediates attached to the glass fiber mats. Since the upper layer of the control sample is subjected to higher temperature and easier access to oxygen, the rate of pyrolysis is much higher for the intermediates in the upper layer in this scenario, hence less char is observed as evidence by Figure 47. Future more, due to the relatively high in-plane thermal conductivity and low through-thickness thermal conductivity of the coating layer, the nanopaper, as shown in Figure 50(a), should also serve as a heat barrier/sink to further protect the underlying structure. It should be noted that this advantage was not full revealed during the cone calorimeter tests in which the samples experienced 1-D heat transfer scenario. However, in reality, this mechanism should take place and alleviate the localized heat concentration.

In summary, with the aid of the nanopaper, a char layer with low permeability is developed on the surface of composites at the very beginning of combustion process. The surface char serves as a mass barrier, inhibiting the mass loss of the matrix. This results in the

thickening of char layer that serves as a thermal barrier, preventing heat transfer into the underlying structure.

4.4.3. Conclusions

The fire response of glass fiber reinforced polyester composites with and without the 3xGnP/1CNF/9APP nanopaper coating were thoroughly studied by cone calorimeter tests, using heat fluxes from 25kW/m^2 to 100kW/m^2 . It was observed that at higher heat flux, the flame retardant effect of the nanopaper was better revealed, indicating its potential for the ablation application. When both samples were exposed to 100kW/m^2 of heat flux, the 1st and 2nd PHRR of the paper coated sample were more than 32% and 47% lower than the PHRR of the control sample, respectively. Furthermore, the middle and back temperature profiles of the samples during the cone calorimeter tests were recorded to gain deeper insight into the pyrolysis process and flame retardancy mechanism. It was found that the time for paper coated sample to reach the middle surface temperature of 400°C at 25kW/m^2 heat flux was 40% later than that of the control sample. Such difference became 190% at 100kW/m^2 heat flux, and the final temperature within the paper coated sample, under this level of heat flux, was roughly 280°C lower than the control sample. The degradation rates in flexural moduli of the samples with coupon shape were determined using three-point bending test. The results also indicated a good fire retardant property of the nanopaper coating. For example, when a sample was exposed to 25kW/m^2 heat flux for 240 seconds, the flexural modulus of the control sample almost was 0, whereas the paper coated sample still retained half of its

flexural modulus. Based on the above observations, a relationship between the fire behaviors, temperature evolutions, mass loss, and mechanical properties of the samples can be inferred. And a flame retardancy mechanism was developed for the nanopaper coated composites.

CHAPTER 5

FINITE ELEMENT MODELING OF THERMAL RESPONSE AND POST-FIRE FLEXURAL DEGRADATION OF GLASS FIBER REINFORCED POLYESTER

5.1. Introduction

The degradation and decomposition of composites will lead to loss in mass and that leads, in turn, to loss in mechanical strength of the structure. Therefore, it is important to develop the capability to predict the mechanical properties of PMCs when they are subjected to high temperatures.

In this study, a temperature dependent post-fire mechanical model was presented. Unlike the two layer model or three layer model, in which a bulk mechanical property value was assigned to each layer [115-121], the residual mechanical properties of the partial composites presented in this chapter, were modeled as temperature-dependent. First, the classic PMCs thermal degradation model with second kind boundary condition (constant heat flux) was derived and solved using finite element method (FEM) with weak form constructing by Galerkin Method. Then using the temperatures that were calculated at different depths and in different locations, a temperature-dependent post-fire residual modulus was assigned to each element within the FE model. Finally, the bulk residual modulus was obtained by assembling the modulus of each element. Both the predicted temperatures and normalized residual modulus were compared with experimental data, and a reasonable agreement was achieved. Furthermore, based on the model, a composites design

application was proposed.

5.2. Thermal Degradation Model Derivation

5.2.1. Energy equations

The first law of thermodynamics indicates that the change in the total energy of the system equals the total energy entering the system minus the total energy leaving the system:

[155]

$$Q_{in} - Q_{out} + E_g = \Delta E_{sys} \quad (5-1)$$

The first two terms in the left hand side represent the net heat transfer and the third term represents the energy generated within the system. The right hand side term represents the energy change of the system. Taking the derivative of the above equation yields:

$$\dot{Q}_x - \dot{Q}_{x+\Delta x} + \dot{E}_g = \frac{\Delta E}{\Delta t} \quad (5-2)$$

$$\dot{Q}_x - \dot{Q}_{x+\Delta x} + \dot{g} A \Delta x = \frac{\Delta E}{\Delta t} \quad (5-3)$$

$$-\frac{\dot{Q}_{\Delta x+x} - \dot{Q}_x}{A \Delta x} + \dot{g} = \frac{\Delta E}{\Delta t A \Delta x} \quad (5-4)$$

When Δx and Δt approach to zero, the above equation can also be written as:

$$-\frac{1}{A} \frac{\partial \dot{Q}}{\partial x} + \dot{g} = \frac{dE}{dt} \quad (5-5)$$

Using Fourier's law, equation (5-5) can be re-written as:

$$\frac{\partial}{\partial x} \left(k \frac{\partial T}{\partial x} \right) + \dot{g} = \frac{dE}{dt} \quad (5-6)$$

In the case of the degradation of PMCs, the density of the material is time-dependent, not a constant. By assuming the volume of the material doesn't change, the rate of change of

internal energy on the right side of equation (5-6) should be:

$$\frac{dE}{dt} = \frac{\partial}{\partial t}(\rho h) = h \frac{\partial \rho}{\partial t} + \rho \frac{\partial h}{\partial t} = \frac{\partial \rho}{\partial t} h + \rho \frac{\partial h}{\partial T} \frac{\partial T}{\partial t} = \frac{\partial \rho}{\partial t} h + \rho c_p \frac{\partial T}{\partial t} \quad (5-7)$$

where c_p is the specific heat of the material. During degradation, part of the polymer becomes char, therefore c_p is a function of temperature and time.

The energy generation term on the left hand side of Equation (5-6) is composed by the convection of energy resulting from gas flow and mass flux from the decomposition of the polymer:

$$\dot{g} = -\frac{\partial}{\partial x}(\dot{m}_g h_g) - Q \frac{\partial \rho}{\partial t} = -\frac{\partial \dot{m}_g}{\partial x} h_g - \dot{m}_g \frac{\partial h_g}{\partial x} - Q \frac{\partial \rho}{\partial t} \quad (5-8)$$

where \dot{m}_g is the mass flux of gas, h_g is the gas enthalpy, Q is the heat of decomposition (negative for the endothermic reactions).

Assuming that there is no accumulation of the gas within the composites structure, due to the conservation of mass, the rate of gas production right at the degradation front can be expressed as:

$$\frac{\partial \dot{m}_g}{\partial x} = -\frac{\partial \rho}{\partial t} \quad (5-9)$$

Assuming that the enthalpy of the material and gas to be functions of temperature only:

$$h = \int_{T_\infty}^T c_p dT = c_p (T - T_\infty)$$

$$h_g = \int_{T_\infty}^T c_{pg} dT = c_{pg} (T - T_\infty) \quad (5-10)$$

where c_{pg} is the specific heat of decomposed gas and T_∞ is the ambient temperature.

From equation 5-6-5-10, the governing equation of the decomposition of PMCs can be rearranged as:

$$\rho c_p \frac{\partial T}{\partial t} = \frac{\partial}{\partial x} \left(k \frac{\partial T}{\partial x} \right) - \dot{m}_g c_{pg} \frac{\partial T}{\partial x} - \frac{\partial \rho}{\partial t} (c_p - c_{pg}) T - \frac{\partial \rho}{\partial t} (Q - (c_p - c_{pg}) T_\infty) \quad (5-11)$$

The decomposition rate of the polymer matrix can be expressed by the well-known Arrhenius empirical equation, namely:

$$\frac{\partial m}{\partial t} = -A m_v [(m - m_e) / m_v]^n \exp(E_a / RT) \quad (5-12)$$

where m , m_v and m_e are, respectively, the mass of the current, virgin (initial), and end stage of the composites during thermal degradation process, A is the pre-exponential factor, E_a is the activation energy, R is the gas constant, n is the order of reaction.

Since it is assumed that there is no volume change throughout the whole decomposition process, by dividing the mass with the volume of the material, equation (5-12) can be written as:

$$\frac{\partial \rho}{\partial t} = -A \rho_v [(\rho - \rho_e) / \rho_v]^n \exp(E_a / RT) \quad (5-13)$$

The non-linear partial differential equations (5-9), (5-11), and (5-12) must be solved simultaneously for \dot{m}_g , T , and m , respectively.

Defining the fraction of remaining virgin material in the solid matrix as:

$$F = \frac{m - m_e}{m_v - m_e} \quad (5-14)$$

Assume that only reinforced fiber left at the end stage of the degradation (also see Figure 51). The density, thermal conductivity, and specific heat of instantaneous stage

composites could be estimated by using the mixture rule:

$$\rho_v = V_f \rho_f + (1 - V_f) \rho_r \quad (5-15-a)$$

$$c_{pv} = V_f c_{pf} + (1 - V_f) c_{pr} \quad (5-15-b)$$

$$\varphi = F \varphi_v + (1 - F) \varphi_e \quad (5-15-b)$$

where the subscripts v , f , r , and e respectively represent virgin composites, fiber, resin, and the end stage. Letter φ can be either ρ , k or c_p .



Figure 51 Residues of the composites after cone calorimeter tests.

In this study, a constant heat flux is applied to the surface of the composites.

Therefore, the boundary condition for exposed surface is:

$$-k \frac{\partial T}{\partial x} = f(x) \quad \text{for } x=0, t>0 \quad (5-16)$$

where $f(x)$ is a function related to the applied heat flux.

For the material subjected to constant heat flux. Staggs suggested [129]:

$$f(x) = \dot{q}'' + h_1(T_\infty - T_s) + \varepsilon\sigma(T_\infty^4 - T_s^4) \quad (5-17)$$

where ε , \dot{q}'' , h_1 , σ , and T_s denote the emissivity of the exposed surface, applied heat flux, convection heat transfer coefficient at the exposed surface, Stefan-Boltzmann constant, and surface temperature, respectively. The values of the above parameters, except the surface

temperature, are assumed to be constant.

At the cold (unexposed) surface, where the material is insulated, the boundary condition can be denoted as:

$$\frac{\partial T}{\partial x} = 0, \dot{m}_g = 0 \text{ for } x=l, t>0 \quad (5-18)$$

The initial conditions are:

$$T=T_0, \rho=\rho_0, \dot{m}_g = 0, F=1 \text{ for } 0 \leq x \leq l \text{ at } t=0 \quad (5-19)$$

5.2.2. Finite element implementation

As previously mentioned, it is difficult to solve the above set of non-linear equation analytically or even semi-analytically. With the development of modern computational technologies, however, one can easily solve the problem by means FDM, FVM or FEM. In this study, the non-linear partial differential equations are solved by means of FEM. And the only remaining challenge is the construction of element matrix. There are many well established techniques to perform this task, including the direct method, variational (Rayleigh-Ritz) method, and weighted residual methods (collocation, subdomain, Galerkin, least square, moment). The Galerkin Method is employed in this study. In the case of global coordinates (semi-analytical approach), the Galerkin method requires the construction of the trial functions that are required to satisfy all the boundary conditions. The difficulty in the procedure is obtaining the coefficients of these trial functions that ultimately compose the explicit expression of the temperature function. In the case of applying Galerkin Method in FE analysis, the trial functions are comprised of nodal temperatures and shape functions and

are derived in local coordinates. The advantage of this process is that the boundary condition is no longer a consideration. It only requires that the shape functions satisfy the geometric continuity, and ultimately, the temperatures at each node are found directly.

Based on the boundary and initial conditions, the nature of heat conduction process, and the properties of the composites, the solution domain is modeled as a one-dimensional body of thickness l , being divided into n elements with the same thickness h . Each element has two nodes at both sides, as shown in Figure 52.

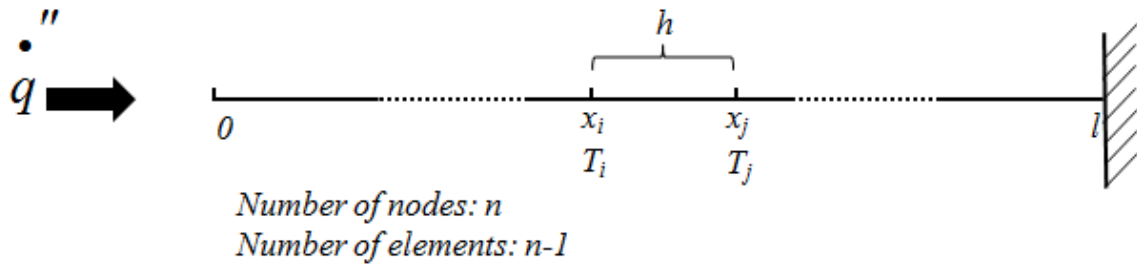


Figure 52 Geometric discretization of the solution domain.

Therefore, the linear trial function is:

$$T(x,t) = [N][T] = \left[\frac{x_j - x}{h} \quad \frac{x - x_i}{h} \right] \begin{bmatrix} T_i \\ T_j \end{bmatrix} \quad (5-20)$$

where N is the shape function, which represents bar element with two nodes.

From the governing equation (5-11), the residue of the problem could be directly expressed as:

$$R = \rho c_p \frac{\partial T}{\partial t} - \frac{\partial}{\partial x} \left(k \frac{\partial T}{\partial x} \right) + \dot{m}_g c_{pg} \frac{\partial T}{\partial x} + \frac{\partial \rho}{\partial t} (c_p - c_{pg}) T + \frac{\partial \rho}{\partial t} (Q - (c_p - c_{pg}) T_\infty) \quad (5-21)$$

Then the weak form of the residue expressed in the global coordinate is:

$$\int_0^l N^T R dx = \int_0^l N^T \rho c_p \frac{\partial T}{\partial t} dx - \int_0^l N^T \frac{\partial}{\partial x} \left(k \frac{\partial T}{\partial x} \right) dx + \int_0^l N^T \dot{m}_g c_{pg} \frac{\partial T}{\partial x} dx \quad (5-22)$$

$$+ \int_0^l N^T \frac{\partial \rho}{\partial t} (c_p - c_{pg}) T dx + \int_0^l N^T \frac{\partial \rho}{\partial t} (Q - (c_p - c_{pg}) T_\infty) dx$$

Using integration by parts, $\int_0^l u \frac{\partial v}{\partial x} dx = \int_0^l \frac{\partial(uv)}{\partial x} dx - \int_0^l v \frac{\partial u}{\partial x} dx$, the following expression

can be derived:

$$\int_0^l N^T \frac{\partial}{\partial x} \left(k \frac{\partial T}{\partial x} \right) dx = \int_0^l \frac{\partial}{\partial x} \left(N^T k \frac{\partial T}{\partial x} \right) dx - \int_0^l \frac{\partial N^T}{\partial x} k \frac{\partial T}{\partial x} dx = \quad (5-23)$$

$$- \int_0^l \frac{\partial N^T}{\partial x} k \frac{\partial T}{\partial x} dx + [N^T k \frac{\partial T}{\partial x}]^l - [N^T k \frac{\partial T}{\partial x}]_0$$

Invoking boundary condition of equation (5-19):

$$[N^T k \frac{\partial T}{\partial x}]^l = 0 \quad (5-24)$$

Keeping in mind that the objective is to reduce the weighted residual as close to zero

as possible and substituting equation (20) into the weak form, finally one could obtain that:

$$\int_0^l N^T \rho c_p N dx \frac{\partial T}{\partial t} + \int_0^l \frac{\partial N^T}{\partial x} k \frac{\partial N}{\partial x} dx T + \int_0^l N^T \dot{m}_g c_{pg} \frac{\partial N}{\partial x} dx T + \int_0^l N^T \frac{\partial \rho}{\partial t} (c_p - c_{pg}) N dx T \quad (5-25)$$

$$+ \int_0^l N^T \frac{\partial \rho}{\partial t} (Q - (c_p - c_{pg}) T_\infty) dx + [N^T k \frac{\partial T}{\partial x}]_0 = 0$$

or in a matrix form of

$$M \dot{T} + (K_c + K_g + K_d) T + L = 0 \quad (5-26)$$

where $M = \int_0^l N^T \rho c_p N dx$ is the capacitance matrix with the local form in element e

(superscripts within parentheses of the following equations denote the element) of

$$\begin{bmatrix} 1 & 1/2 \\ 1/2 & 1 \end{bmatrix} \left(\frac{h \rho c_p}{3} \right)^{(e)} \quad (5-27)$$

$K_c = \int_0^l \frac{\partial N^T}{\partial x} k \frac{\partial N}{\partial x} dx$ is the thermal conductivity matrix with the local form in element e of

$$\begin{bmatrix} 1 & -1 \\ -1 & 1 \end{bmatrix} \left(\frac{k}{h} \right)^{(e)} \quad (5-28)$$

$K_g = \int_0^l N^T \dot{m}_g c_{pg} \frac{\partial N}{\partial x} dx$ is the gas convection matrix with the local form in element e of

$$\begin{bmatrix} -1 & 1 \\ -1 & 1 \end{bmatrix} \left(\frac{h \dot{m}_g c_{pg}}{2} \right)^{(e)} \quad (5-29)$$

$K_d = \int_0^l N^T \frac{\partial \rho}{\partial t} (c_p - c_{pg}) N dx$ is the decomposition matrix with the local form in element e of

$$\begin{bmatrix} 1 & 1/2 \\ 1/2 & 1 \end{bmatrix} \left(\frac{h}{3} \frac{\partial \rho}{\partial t} (c_p - c_{pg}) \right)^{(e)} \quad (5-30)$$

$L = \int_0^l N^T \frac{\partial \rho}{\partial t} (Q - (c_p - c_{pg}) T_\infty) dx + [N^T k \frac{\partial T}{\partial x}]_0$ is the thermal load vector.

Applying boundary condition at the first node (the subscripts of letter L in the following equations denote the node) is:

$$L_1 = \frac{h}{2} \left(\frac{\partial \rho}{\partial t} (Q - (c_p - c_{pg}) T_\infty) \right)^{(1)} - (\varepsilon \dot{q}'' + h_1 (T_\infty - T_s) + \varepsilon \sigma (T_\infty^4 - T_s^4)) \quad (5-31)$$

at the last node is:

$$L_n = \frac{h}{2} \left(\frac{\partial \rho}{\partial t} (Q - (c_p - c_{pg}) T_\infty) \right)^{(n-1)} \quad (5-32)$$

at any other node is:

$$L_i = \frac{h}{2} \left(\frac{\partial \rho}{\partial t} (Q - (c_p - c_{pg}) T_\infty) \right)^{(i)} + \frac{h}{2} \left(\frac{\partial \rho}{\partial t} (Q - (c_p - c_{pg}) T_\infty) \right)^{(i-1)} \quad (5-33)$$

Therefore, within the first order differential equation (5-26), the unknown coefficients are ρ, c_p, k, \dot{m}_g , and $\frac{\partial \rho}{\partial t}$. As indicated by equation (5-15), the first three parameters are

functions of F . By manipulating equation (5-12) (5-13), and (5-14), one can derive the following expression:

$$\frac{\partial F}{\partial t} = -A[(\rho_v - \rho_e) / \rho_v]^{n-1} \exp(E_a / RT) F^n \quad (5-34)$$

$$\frac{\partial \rho}{\partial t} = \frac{\partial F}{\partial t} (\rho_v - \rho_e) \quad (5-35)$$

Furthermore, the integration of equation (5-9) throughout with $\int_x^l dx$ and the application of the boundary condition (5-19) yield:

$$\dot{m}_g(x) = \int_x^l \frac{\partial \rho}{\partial t} dx \quad (5-36)$$

Therefore, all the coefficients are eventually functions of F only, which initially has a value of 1.

5.2.3. Treatment of the transient part

By using the finite difference theory (Crank-Nicolson approximation), the matrix equation (5-26) has been re-written as:

$$\left(\frac{2}{\Delta t} M_{n+1} + (K_c + K_g + K_d)_{n+1}\right) T_{n+1} - M_{n+1} \dot{T}_n - \frac{2}{\Delta t} M_{n+1} T_n + L_{n+1} = 0 \quad (5-37)$$

$$\dot{T}_n = M_n^{-1} \left(-(K_c + K_g + K_d)_n - L_n \right) \quad (5-38)$$

where subscripts n and $n+1$ denote the known and unknown quantities, respectively.

Therefore, if one can calculate the value of F_{n+1} , the unknown temperature T_{n+1} in equation (5-38) can be solved using typical numerical iterations.

And Crank-Nicolson approximation and equation (5-34) give:

$$\frac{2}{\Delta t} (F_{n+1} - F_n) - \frac{\partial F}{\partial t}_n + A[(\rho_v - \rho_e) / \rho_v]^{n-1} \exp(E_a / RT_{n+1}) F_{n+1}^n = 0 \quad (5-39)$$

which indicates that F_{n+1} can be expressed as a function of T_{n+1} .

Finally, given the initial conditions of T and F , equation (5-37) is solvable as it is only a function of T_{n+1} .

5.3. Post-Fire Flexural Modulus Implementation

The post-fire mechanical properties differ from the real time thermal mechanical properties of the PMCs structures. For the post-fire scenario, when the materials are cooled to ambient temperature, they tend to regain their mechanical properties. One may assume that the mechanical properties are unchanged if the temperature of the polymer is only higher than its glass transition temperature, but lower than its degradation temperature. However, if PMCs were simultaneously subjected to thermal and mechanical loads (the real-time case), the structure was more likely to fail. In this case, a certain reduction in mechanical properties occurs when the temperature is higher than the glass transition temperature of the polymer.

Suppose the temperature range of the major mechanical degradation is from T_1 to T_2 . For polyester resin, T_1 is likely the same as its onset decomposition temperature, which from TGA analysis is about 500K. Therefore, in the following post-fire mechanical modeling, one could assume that the normalized modulus of the composites that experiences a temperature profile that below 500K have a value of 1, *i.e.* full recovery. However, when the temperature of the material is higher than the decomposition temperature of the polymer matrix, there will be irreversible damage even after the sample is cooled down to the ambient temperature. As

observed by Goodrich and Lattimer, the pore size (originated from debonding) between fibers gradually increased as the polymer matrix started to decompose [137]. Therefore, it is assumed that the bonding between reinforced glass and resin is destroyed long before the polymer is completely decomposed. T_2 should be much lower than the final decomposition temperature of the polymer. When the temperature is higher than T_2 , however, it is assumed that there is no mechanical resistance left for the sample.

Therefore, the remaining challenges are to determine the value of T_2 and the temperature and time dependent normalized residual mechanical properties functions. The residual mechanical moduli in this study are modeled as linearly dependent on the temperature, *i.e.*:

$$E_n(x,t) = \begin{cases} 1 & 0 \leq T < T_1 \\ \alpha[T_2 - T(x,t)] & T_1 \leq T < T_2 \\ 0 & T_2 \leq T \end{cases} \quad (5-40)$$

where $E_n(x,t)$ represents the normalized residual mechanical properties. The coefficient α and the temperature T_2 at which the composites have no mechanical resistance are determined by experiment. It should be note that in this model, since α is experimentally determined, the coefficient has already taken into account the effects of different loading conditions. That is when α is determined under bending condition, E_n should be the flexural modulus. Therefore, the FE implementation of the temperature dependent normalized residual mechanical properties in the global coordinates is:

$$E_N = \frac{\sum_{i=1}^n (E_n(x,t))^{(i)}}{n} \quad (5-41)$$

where i represents the position of the element. It should be noted, since the modulus of reinforced fiber is not affected by high temperatures and the mass loss is dominated by the decomposition of the resin matrix [137], the mechanical model which is derived based on the thermal degradation of the polymer matrix is only valid for the matrix-dominated properties such as flexural modulus.

Finally, the FE computational procedure for the thermo-mechanical problem is shown in the following flow chart.

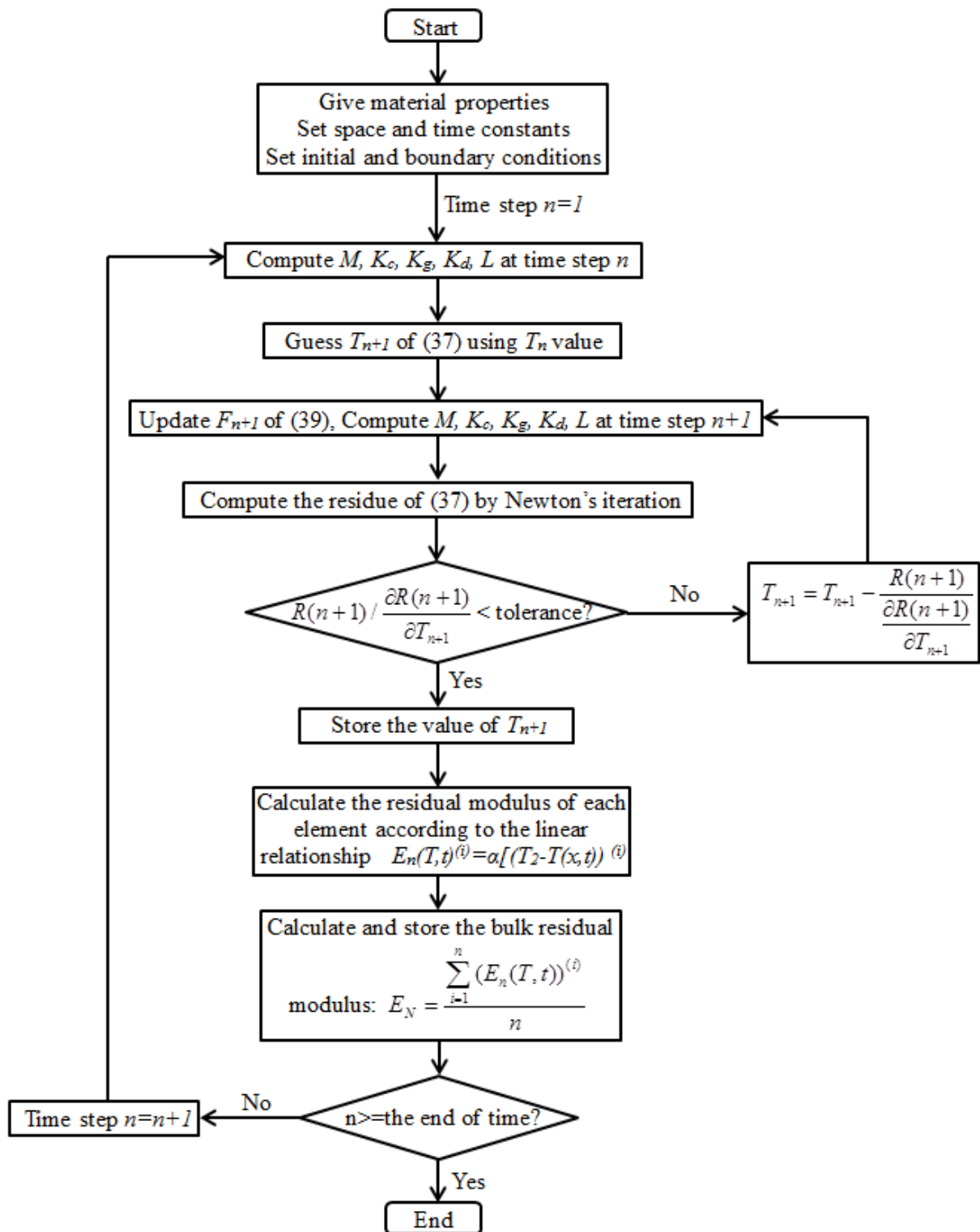


Figure 53 Computational algorithm of the FE model.

5.4. Verification and Discussion

Due to the limited available thermo-physical data for the polyester-based composites in the literature, the material properties such as specific heat and thermal conductivity were assumed to be temperature-independent. Furthermore, as indicated by the residues collected after cone calorimeter test in this study (Figure 51), it is reasonable to assume that in the final stage of the degradation process, there was only glass fiber left. As a result, the parameters of the glass fiber reinforce polyester panel used in this study were summarized in Table 15.

Table 15 Input parameters of the materials.

Parameters (Definition)	Value (Unit) [Ref.]
A (Pre-exponential factor)	1000 (s ⁻¹) [TGA]
c _{pf} (Specific heat of glass fiber)	760 (J.kg ⁻¹ .K ⁻¹) [125]
c _{pr} (Specific heat of polyester resin)	1600 (J.kg ⁻¹ .K ⁻¹) [125]
c _{pg} (Specific heat of decomposed gas)	2386.5 (J.kg ⁻¹ .K ⁻¹) [125]
E _a (Activation energy)	50000 (J.g ⁻¹ .mole ⁻¹) [TGA]
k _f (Thermal conductivity of glass fiber)	1.04 (W.m ⁻¹ .K ⁻¹) [125]
k _r (Thermal conductivity of polyester resin)	0.20 (W.m ⁻¹ .K ⁻¹) [125]
Q (Heat of decomposition)	-234460 (J.kg ⁻¹) [125]
V _f (Glass fiber volume fraction)	30%
L (Thickness of the composites)	3.5 (mm)
ρ _f (Density of glass fiber)	2694.7 (kg.m ⁻³)
ρ _r (Density of polyester resin)	1102.4 (kg.m ⁻³)
ρ _v (Density of virgin composites)	1580 (kg.m ⁻³)
n (Reaction order)	1[126]
ε (Emissivity of the exposed surface)	0.9 [129]
h ₁ (Convection heat transfer coefficient)	10 (W.m ⁻² .K ⁻¹) [129]

For the thermal conductivity of the virgin composites, Staggs suggested that for a heterogeneous medium with cylindrical glass fiber inclusions, which have a volume fraction

of V_f , in the direction normal to the fibers (heat conduction direction), the thermal conductivity is [156]:

$$k_v = k_r \left[1 + \frac{2V_f}{(k_r + k_f)/(k_f - k_r) - V_f + ((k_r - k_f)/(k_f + k_r))(0.3058V_f^4 + \dots)} \right] \quad (5-42)$$

For the residual materials which are composed by glass fibers and voids where polyester resin used to be, the thermal conductivity could be expressed as:

$$k_{ch} = k_f \left[\frac{1}{1 - V_f + 1/(k_{air}/k_f V_f + 4\sigma T^3 L/k_f)} \right] \quad (5-43)$$

where T is approximately equal to 400K [127].

Arrhenius kinetic constants are readily determined by fitting the TGA curve using Equation (5-12). In this paper, the adopted fitting technique was proposed by Feih *et al* as they found that the accuracy and reliability of the method was to be superior to the graphical analysis tools that were normally used [112]. Assuming that the polymer decomposition is a first-order Arrhenius process, F as a function of temperature (K) can be expressed as:

$$F(T) = F_f + (1 - F_f) e^{\left[-\int_{T_0}^T \frac{A}{HR} \left(e^{-\frac{E_a}{RT}} \right) dT \right]} \quad (5-44)$$

where $F(T)$ is the normalized mass fraction defined by Equation (5-14); F_f is the remaining mass of the polymer at the end of decomposition process, and is readily obtained from the experimental TGA data; T_0 is the onset decomposition temperature; HR is the heating rate.

The TGA instrument used in this study was TGA-Q500 manufactured by TA Instruments, USA. The experiment was conducted in nitrogen atmosphere at a flow rate of 40 ml/min and a heating rate of 10°C/min. In general, the determination of Arrhenius constants

goes through the fitting of TGA curves that obtain from different heating rate and the set of best fitted data is selected. However, the study done by Lua *et al* showed that the fire response predictions show little sensitivity to the heating rates [128]. Therefore, the kinematic parameters obtained from the TGA test at a single heating rate can be used in the modeling.

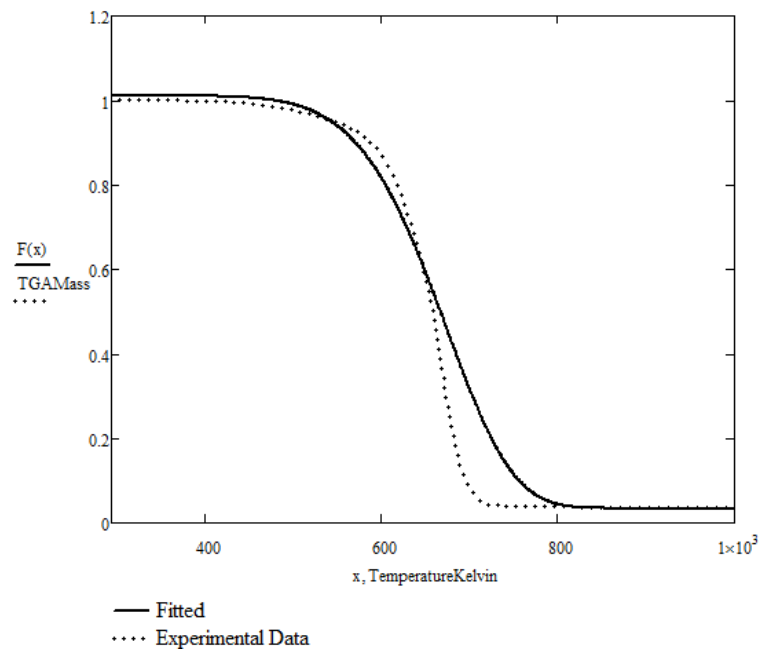


Figure 54 TGA data of the composites with curve fitting.

As shown in Figure 54 and Table 15, by using Mathcad, the values for E_a and A from curve fitting are $50000\text{J}\cdot\text{g}^{-1}\cdot\text{mol}^{-1}$ and 1000s^{-1} , respectively. In addition, for the 1-D FE model presented in this study, the solution domain in the thickness direction is divided into 10 elements, each with the same length of 0.35mm. The time step was chosen to be 0.5s and the model was computed for 300s based on the exposure time shown in Table 14.

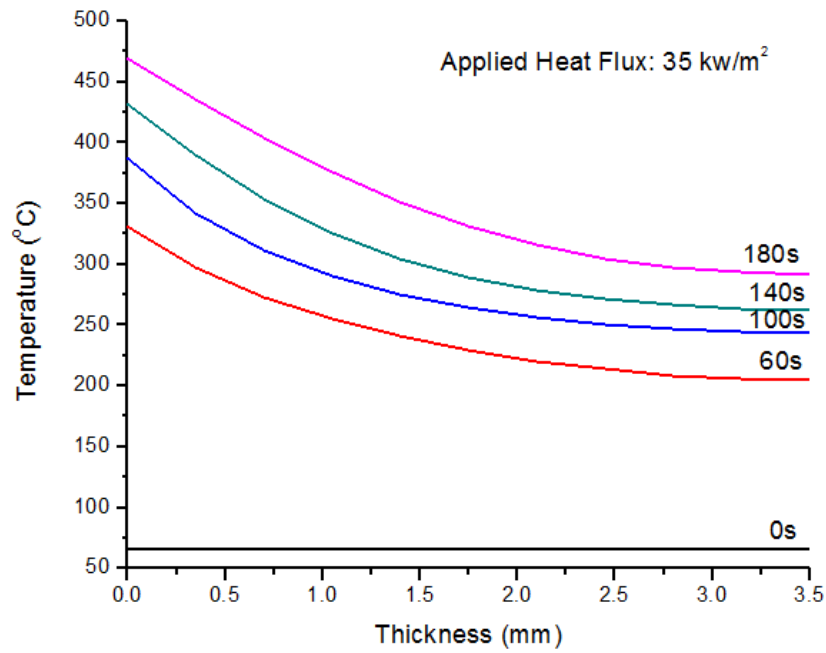


Figure 55 Temperature at different locations for different exposure times.

T_2 and α , shown in equation (5-40) are determined through an inverse solution technique. Experimentally, for the samples subjected to 35 kW/m^2 heat flux for 100s and 180s, the normalized post-fire flexural moduli respectively are 0.5 and 0. And the predicted temperatures at different depths of the samples with different exposure times are shown in Figure 55. As a result of Equation (5-40) and (5-41), the inversely determined values for T_2 and α are 573K and 1.674, respectively. Then these two values are used in the rest of the calculations.

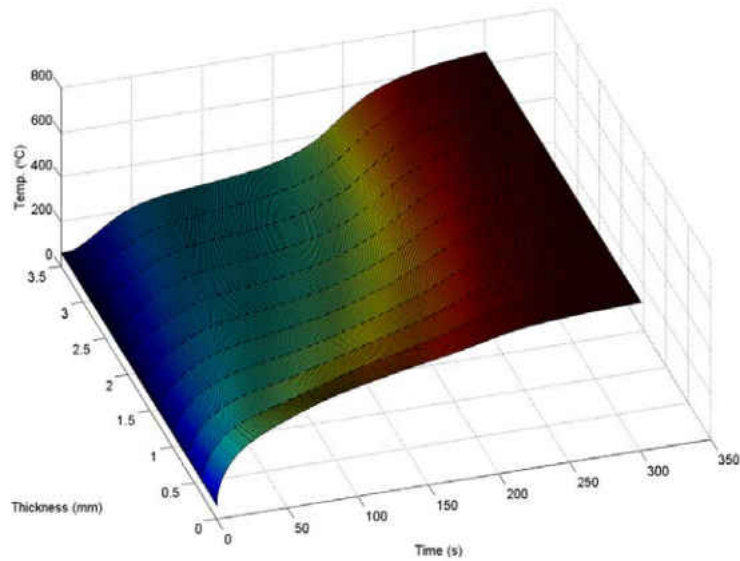


Figure 56 3-D plot of the thermal degradation model with applied heat flux of 50kW/m^2 .

Figure 56 shows the predicted temperature for those samples subjected to the 50kW/m^2 heat flux as a function of time and location. The 3-D plot indicates that the calculated data are in good agreement with the expected physical behavior, with higher temperature at the front surface and lower temperature at the back surface. The temperature gradually increases with time. And the zero slope for the data at the back surface, denoting the insulated boundary condition. Furthermore, the concave temperature surface in the 3-D plot at the middle stage (100s~200s) of degradation process indicates that endothermic decomposition reaction occurs.

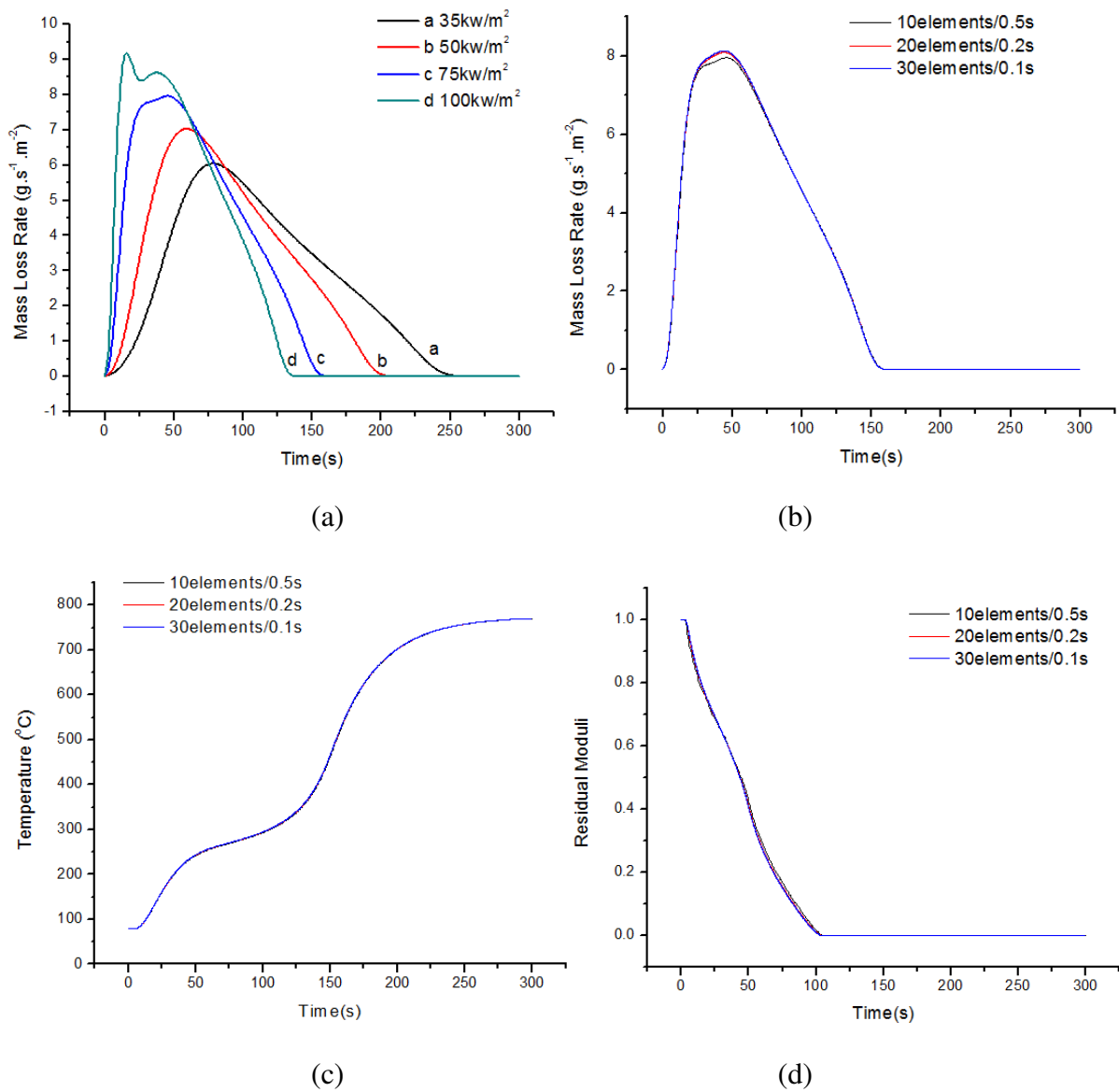


Figure 57 Convergence study. (a) mass loss rate; (b) mass loss rate with different discretizations (75kW/m²); (c) back side temperature with different discretizations (75kW/m²); (d) remaining mass with different discretizations (75kW/m²).

The convergence of the FE model presented in this study was studied and shown in Figure 57. As shown in Figure 57 (a), the mass loss rate gradually increases with the increase of applied heat flux, which physically makes sense. In addition, all of the predictions start with the value of zero and increase to a maximum before they drop back to the zero value,

indicating the convergence of the model. Furthermore, as shown from Figure 57 (b) to (d), the convergence of the model is confirmed by the result that the predictions are almost indistinguishable when the discretization level is changed.

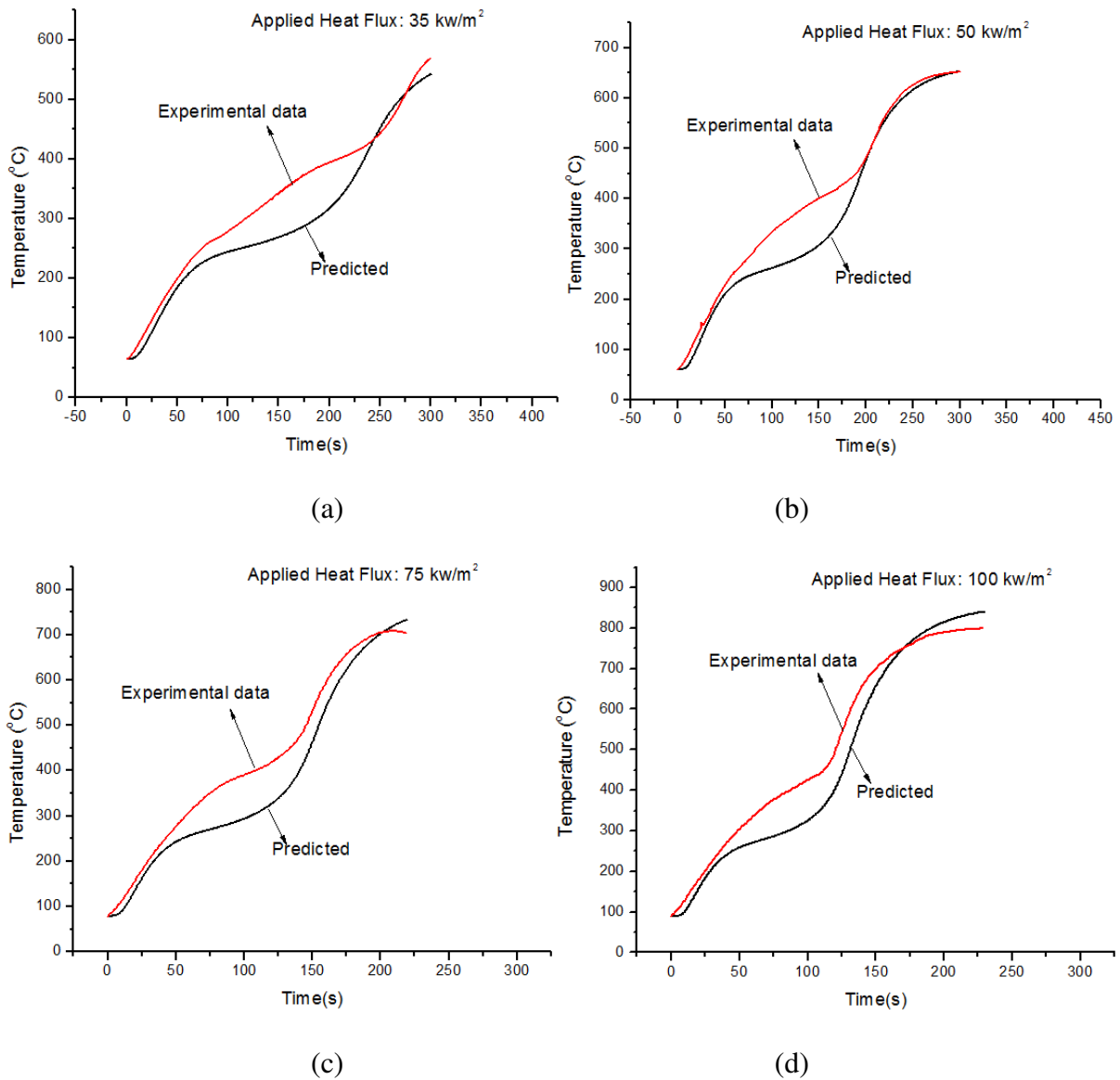


Figure 58 Comparison of experimentally measured temperatures with numerical predictions.

Figure 58 shows the comparison of the back side temperature between the predicted results and experimentally measured data. Generally speaking, a reasonably agreement

between the prediction and experimental data is observed for the samples that are exposed to heat fluxes of 35kW/m^2 , 50kW/m^2 , 75kW/m^2 , and 100kW/m^2 . The agreement is especially good during the initial and final stages of exposure. However, the predicted temperature during the middle stage is lower than the experimental data. Excluding the errors arising from the input parameters such as the thermal conductivity and specific heat, a possible reason for this result is that the model does not take the flame temperature into account. As a result, during the middle of decomposition process where the flame should be well developed, the re-radiation energy of flame back to the surface of the sample could increase its temperature. During the initial and final stages of the decomposition process, the contribution of flame temperature is small, leading to better fits. Therefore, in order to further improve the accuracy of the temperature prediction, it is important to redefine the surface boundary condition. Another possible reason is that when embedding thermocouples by the RTM process, the wires might not be perfectly located at the surface of the cold side. One notable shortcoming is that their diameter is about 0.51mm while the total thickness of the sample is only about 3.5 mm . In fact, the parameter such as the thickness would greatly affect the temperature distribution. This will be presented in the following discussion. Considering these factors, a higher cold side temperature might be observed.

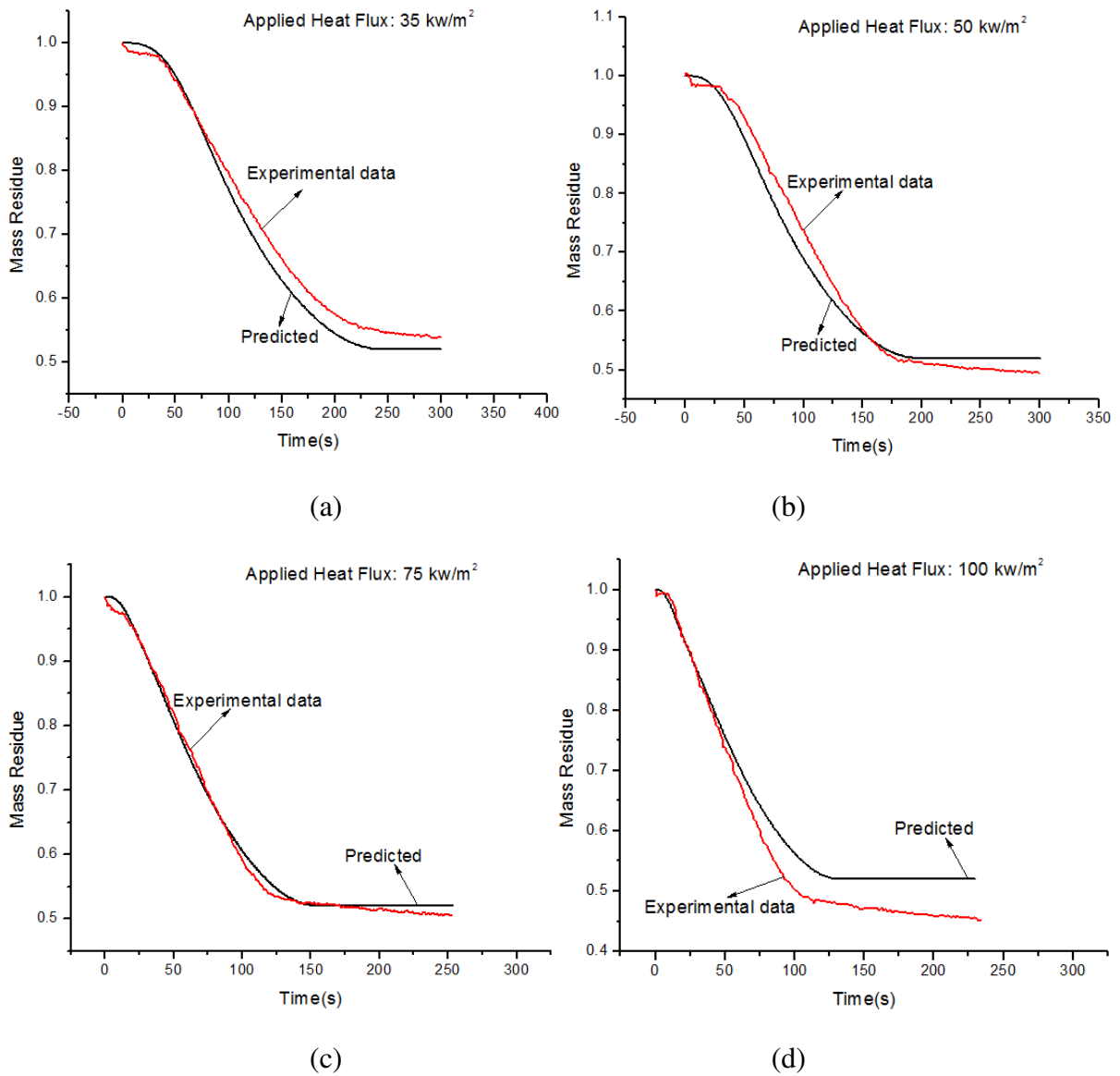


Figure 59 Comparison of experimentally measured ratio of remaining mass with numerical predictions.

The remaining weight ratios are shown in Figure 59. As expected, when the applied heat fluxes increased, the time at which the entire polymer matrix had been degraded (there is no change in mass residue) occurred earlier. Furthermore, in this model, no glass fiber degradation is taking into account. Therefore, all of the predicted results end up with approximately the same 52% of residue, which equals to the weight percentage of glass fiber

within the composites.

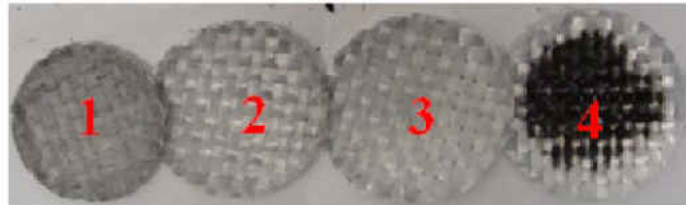
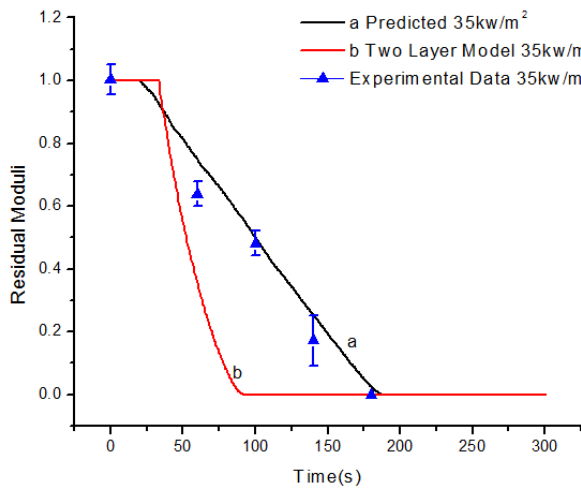


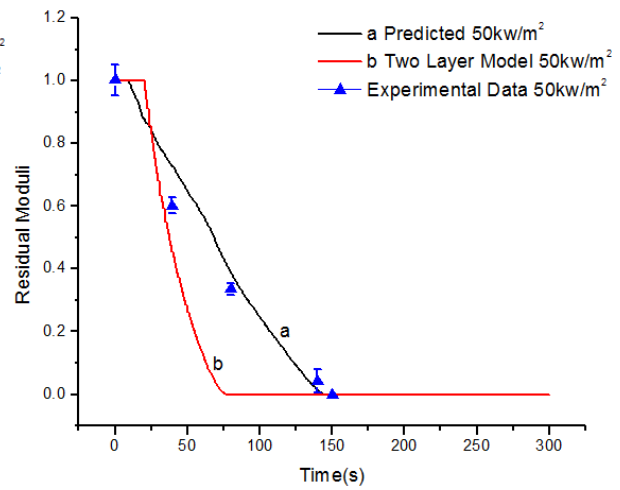
Figure 60 Remaining glass fiber mats after the sample was exposed to 100kw/m^2 heat flux (the surface layer is in the most left).

However, in reality, as shown in Figure 60 the degradation of glass fiber occurs at 100kw/m^2 of applied heat flux. As a result, the experimental data of the remaining mass is lower than the calculated value at the end of degradation process. Other than that, the predicted remaining mass seems very accurate, with less than 5% of difference.

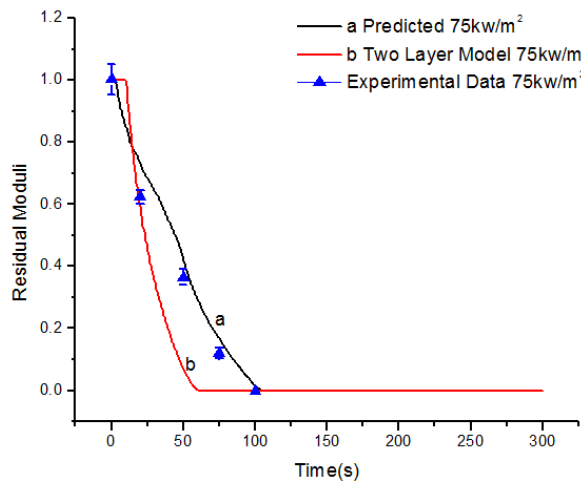
Figure 61 shows the comparison of residual flexural moduli between the predicted value from the FE model, the two-layer model proposed by Mouritz *et al* (by assuming that when the remaining resin content of the composites is more than 80%, they will regain their original strength), and the experimental data. The results indicate that the temperature related FE model prediction is more accurate than that of the two-layer model. Therefore, the assumption of the residual moduli being linearly temperature-dependent is acceptable, since a very good agreement can be obtained.



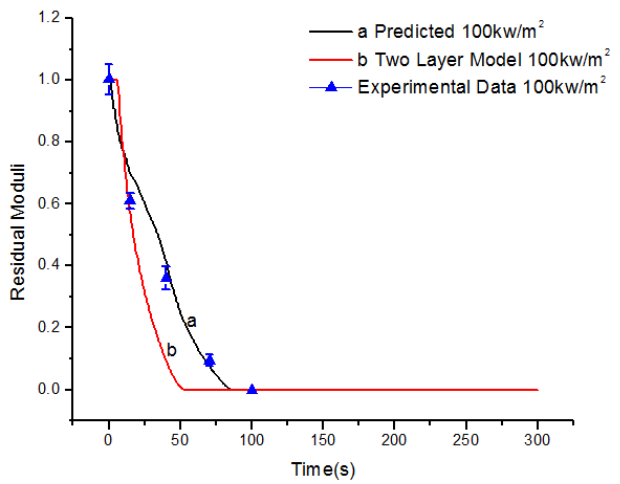
(a)



(b)



(c)



(d)

Figure 61 Model verification by normalized residual flexural moduli.

As both the experimental and predicted data suggest, the degradation rate in residual moduli increases when the samples are subjected to higher heat fluxes, and the exposure time of the samples after which they can fully regain their initial mechanical resistance becomes shorter. Furthermore, the good agreement of the bulk material flexural moduli implies that the predicted temperature cold side temperature profiles as shown in Figure 57 might be more

accurate than that the measured data.

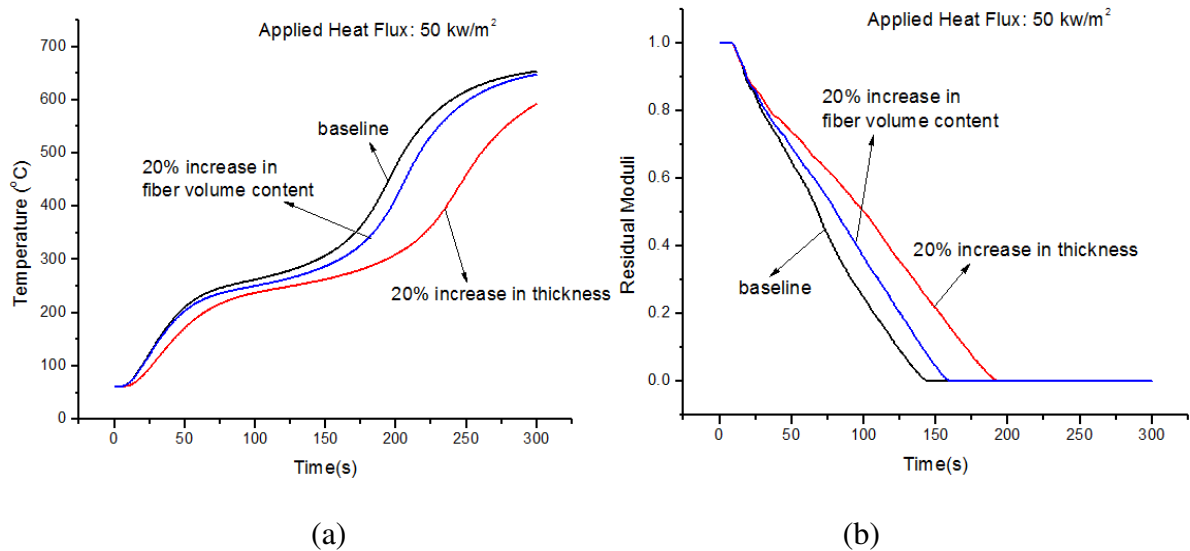


Figure 62 Material design. (a) model predictions of temperatures; (b) model predictions of residual moduli.

Upon successful developing the thermo-mechanical model, future material design can be formulated. In this study, two parameters, namely, fiber volume fraction and sample thickness are modified in order to find an efficient design of PMCs structure, for the given fiber and resin. The results for varying the content of fiber and thickness are shown in Figure 62 (a) and (b). As suggested by the figure, by increasing fiber volume fraction by 20% in the sample, the impact for the cold side temperature as well as the rate of mechanical resistance degradation is modest. However, the effect is more noticeable when the thickness of the sample is increased 20%, with both the cold side temperature and the mechanical resistance degradation rate being greatly reduced. From the model, it can be shown that improvement of

the latter case (increasing thickness) over the former (increasing the fiber count) being roughly doubled. In other words, it is more effective to enhance the durability of the composite by increasing its thickness than its fiber volume fraction. This might also partially explain the mechanism of the intumescent coating, namely, under the fire condition, the thickness of the composite materials is increased.

5.5. Conclusions

In this chapter, a FE model that couples with the temperature-dependent residual moduli to study the post-fire mechanical behavior of composites was successfully developed. The calculated temperature and residual mechanical moduli demonstrated reasonable agreement with the experimental data which was obtained from the samples exposing to various heat fluxes. However, it is suggested that if the temperature-dependent variables such as the thermal conductivity and specific heat are available, and if the front surface boundary condition is better defined, the accuracy of the model could be further improved. Furthermore, by manipulating some parameters of the model, an effective strategy was proposed for the design of PMCs structure with enhanced durability: it is more desirable to get a thicker composite than a higher fiber volume fraction composite.

CHAPTER 6

FINITE DIFFERENCE MODELING OF THERMAL RESPONSE AND POST-FIRE FLEXURAL DEGRADATION OF GLASS FIBER REINFORCED POLYESTER COATED WITH CARBON NANOFIBER BASED NANOPAPERS

6.1. Introduction

Extensive research has been done to improve the flame resistance performance of polymer composites, either by means of mixing different types of fire retardants directly into the polymer matrix or by means of coating various kinds of protective layers onto the surface of PMCs [10][12][15][157]. Morgan *et al* summarized that regardless of different approaches, the ultimate goal was to reduce the heat release rate of the material by inhibiting the mass loss rate [153]. Consequently, it is expected that with the lowered mass loss rate during fire scenarios, the structural integrity of the material will be improved. As discussed in previous chapters that when glass fiber reinforced polyester composites were surface coated with a very thin layer of CNF-based nanopaper, the post-fire flexural moduli of the materials were improved. As shown in the Figure 33 (the self-weight sustaining experiment), the control sample cannot sustain its own weight after a heat (35kw/m^2) exposure time of 200s, while the samples coated with the nanopapers can sustain their own weight even after 300s exposure.

Further investigation in the residues of the cone calorimeter test of the composites samples with and without surface nanopaper coating (Figure 47), showed that the paper coated samples produced a greater amount of char than the control sample. The upper layer

(layer 1 in Figure 47) of the reinforced glass fiber mats showed damage and shrinkage when the control samples were exposed to 100kw/m^2 heat flux. However, there was no clear damage observed for glass fiber mats of the nanopaper-coated samples.

The objective of this study is to numerically analyze the impact of the nanopaper on the post-fire mechanical property of the polymer composite materials. There are many research papers that deal with the thermal response modeling of composites panel coated with protective coating while subjecting to heat, especially the thermo-chemical modeling of the composites panel protected by intumescent coating [130-136]. However, most of research was focused on the detailed modeling of the thermal response of the coating layer while the impact of porosity and permeability of the underlying composites was ignored, probably due to the limited available data. These parameters have recently estimated by Goodrich *et al* as they studied the microscopic changes within the composites structure during fire, which makes it possible to refine the thermal response modeling of the composites structure [137].

In Chapter 5, a thermal response coupled with post-fire mechanical degradation model was developed for glass fiber reinforced polyester composites. The predicted results showed reasonable agreement with experimental data. In this study, a finite difference model was developed to predict the fire response of the composites coated with nanopaper. The model adopted the same post-fire mechanical model proposed in the previous study. However, unlike the previous model, the permeability and porosity of the composites were taken into account for the thermal degradation model in this study.

6.2. Thermal Degradation Model Derivation

6.2.1. Energy equations

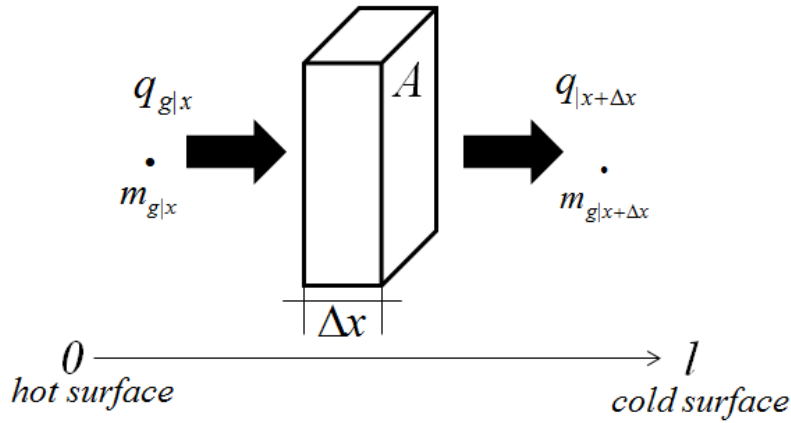


Figure 63 Schematic of the energy and mass flow within a finite volume of the composites.

Assuming that thermal equilibrium exists between the solid and gas phase and the decomposed gases are non-reactive, for the finite volume as shown in Figure 63, the energy equation will be:

$$\frac{\partial}{\partial t}(m_g h_g + mh) = (q|_x - q|_{x+\Delta x})A + [(\dot{m}_g h_g)|_x - (\dot{m}_g h_g)|_{x+\Delta x}]A + S.\Delta x.A \quad (6-1)$$

where h , m_g , m , \dot{m}_g , and S are enthalpy, mass of gases stored within the composite structure (kg), solid mass of composite structure (kg), mass of gases flow out of the composite structure ($\text{kg.m}^{-2}.\text{s}^{-1}$), and rate of heat generation per unit volume ($\text{J. m}^{-3}.\text{s}^{-1}$), respectively, with the subscript g referring to the gas phase. When Δx becomes 0, the above equation can be re-written as:

$$\frac{\partial}{\partial t}(m_g h_g + mh) = -\frac{\partial}{\partial x} q.dV + [-\frac{\partial}{\partial x} (\dot{m}_g h_g).dV] + S.dV \quad (6-2)$$

By assuming there is no volume change during thermal decomposition of the

composite structure and invoking Fourier's law, equation (6-2) becomes:

$$\frac{\partial}{\partial t}(\phi \cdot \rho_g h_g + \rho h) = \frac{\partial}{\partial x} [k_g \phi \frac{\partial T}{\partial x} + k(1-\phi) \frac{\partial T}{\partial x}] - \frac{\partial}{\partial x} (\dot{m}_g h_g) - Q \frac{\partial \rho}{\partial t} \quad (6-3)$$

where ϕ , ρ , k , and Q are the porosity of the composite structure (unit less), density (kg.m^{-3}), thermal conductivity ($\text{J.m}^{-1}.\text{K}^{-1}.\text{s}^{-1}$), and heat of decomposition (J.kg^{-1}), respectively. Q is negative in this equation, due to the endothermic nature of polymer decomposition reaction.

Additionally, the value of \dot{m}_g should be negative due to the definition of positive direction shown in Figure 64, while the value of $\frac{\partial \dot{m}_g}{\partial x}$ should be positive if the direction of gas flow was toward exposed surface.

Furthermore, the conservation of mass gives:

$$\frac{\partial \dot{m}_g}{\partial x} + \phi \frac{\partial \rho_g}{\partial t} = - \frac{\partial \rho}{\partial t} \quad (6-4)$$

The physical meaning of this equation is that the gases flow out of the composite structure plus the gases stored within the composite structure equal to the mass change of the solid material. Due to the decomposition of the polymer matrix, the value of $\frac{\partial \rho_g}{\partial t}$ should be positive and the value of $\frac{\partial \rho}{\partial t}$ should be negative.

By substituting equation (6-4) into equation (6-3) and assuming enthalpy is only a function of temperature, the energy equilibrium equation become:

$$\frac{\partial T}{\partial t}(\phi \cdot \rho_g c_{pg} + \rho c_p) = \frac{\partial}{\partial x} [k_g \phi \frac{\partial T}{\partial x} + k(1-\phi) \frac{\partial T}{\partial x}] - \frac{\partial T}{\partial x} \cdot \dot{m}_g c_{pg} - \frac{\partial \rho}{\partial t} [(c_p - c_{pg})(T - T_\infty) + Q] \quad (6-5)$$

where c_p is the specific heat ($\text{J.kg}^{-1}.\text{K}^{-1}$) and T_∞ is the ambient temperature (K).

In addition, assume that the decomposed gases behave ideally and the flow of gases is

governed by Darcy's law, one can get the following two equations:

$$\dot{m}_g = -\frac{r\rho_g}{\mu} \frac{\partial P}{\partial x} \quad (6-6-a)$$

$$P = \frac{\rho_g RT}{M} \quad (6-6-b)$$

where r , μ , P , R , and M are permeability (m^2) of the material, viscosity of the gases ($\text{kg}\cdot\text{s}^{-1}\cdot\text{m}^{-1}$), pressure (Pa), gas constant ($8.31\text{J}\cdot\text{mol}^{-1}\cdot\text{k}^{-1}$), and molecular weight of the gases ($\text{kg}\cdot\text{mol}^{-1}$), respectively.

Furthermore, the decomposition reaction of the polymer matrix is modeled by the Arrhenius empirical equation, namely:

$$\frac{\partial m}{\partial t} = -Am_v[(m - m_e)/m_v]^n \exp(E_a/RT) \quad (6-7)$$

where m , m_v and m_e are, respectively, the mass of the current, virgin (initial) and end state of the composites during thermal degradation process, A is the pre-exponential factor(s^{-1}), E_a is the activation energy ($\text{kJ}\cdot\text{kg}^{-1}\cdot\text{mol}^{-1}$), and n is the order of reaction.

As it is assumed that there is no volume change during the entirety of the decomposition process, dividing the mass with the volume of the material, equation (6-7) can be written as:

$$\frac{\partial \rho}{\partial t} = -A\rho_v[(\rho - \rho_e)/\rho_v]^n \exp(E_a/RT) \quad (6-8)$$

Since the reinforced glass fibers are thermally more stable than the other materials, one could assume that there is only glass fibers left at the end of the decomposition process.

Therefore, the fraction of virgin material remaining in the solid matrix can be defined as:

$$F = \frac{m - m_e}{m_v - m_e} = \frac{\rho - \rho_f}{\rho_v - \rho_f} \quad (6-9)$$

Assume the density, thermal conductivity, and specific heat of current stage composites could be approximately calculated by using the mixture rule:

$$\rho_v = V_f \rho_f + (1 - V_f) \rho_r \quad (6-10-a)$$

$$c_{pv} = V_f c_{pf} + (1 - V_f) c_{pr} \quad (6-10-b)$$

$$\varphi = F \varphi_v + (1 - F) \varphi_e \quad (6-10-c)$$

where the subscripts v , f , r , and e respectively represent virgin composites, fiber, resin, and the end stage. Letter φ stands for the material parameters that are evolving during the decomposition process and can be either ϕ , k , r , or c_p .

The non-linear partial differential equation set (6-4), (6-5), (6-6) and (6-8) must be solved simultaneously for ρ_g , T , \dot{m}_g and ρ , respectively. Similar thermal response models have been solve by Henderson, Gibson, Looyeh, Krysl, Lattimer, Lua, and Summers using finite difference method, finite volume method, and finite element method. But these solutions neglected the effect of the porosity and permeability of the composites structure and the impact of gas storage, [122-128][158]. In this study, due to the complexity of the non-linear equation system, the straightforward finite difference method was used to discretize the one dimensional geometry and the time zone. By incorporating equation set (6-10), the nonlinear system is ultimately expressed as functions of ρ_g , T , \dot{m}_g and ρ .

6.2.2. Post-fire flexural degradation model

As long as the temperatures of the sample at different locations and in different times are calculated, the post-fire mechanical properties can be determined based on the temperature dependent model proposed in the previous chapter:

$$E_n(T, t) = \begin{cases} 1 & 0 \leq T < T_1 \\ \alpha(T_2 - T(x, t)) & T_1 \leq T < T_2 \\ 0 & T_2 \leq T \end{cases} \quad (6-11)$$

where $E_n(T, t)$ represents the normalized residual mechanical properties. For polyester resin, T_1 is likely the same as its onset decomposition temperature which is about 513K. The coefficient α and the temperature T_2 at which the composites have no mechanical resistance are determined experimentally.

Finally, with proper initial and boundary conditions, the whole set of non-linear equations formulated by finite difference method are solved directly by using Newton iteration and Gaussian elimination with partial pivoting. The algorithm of the MATLAB code is shown in the following flow chart.

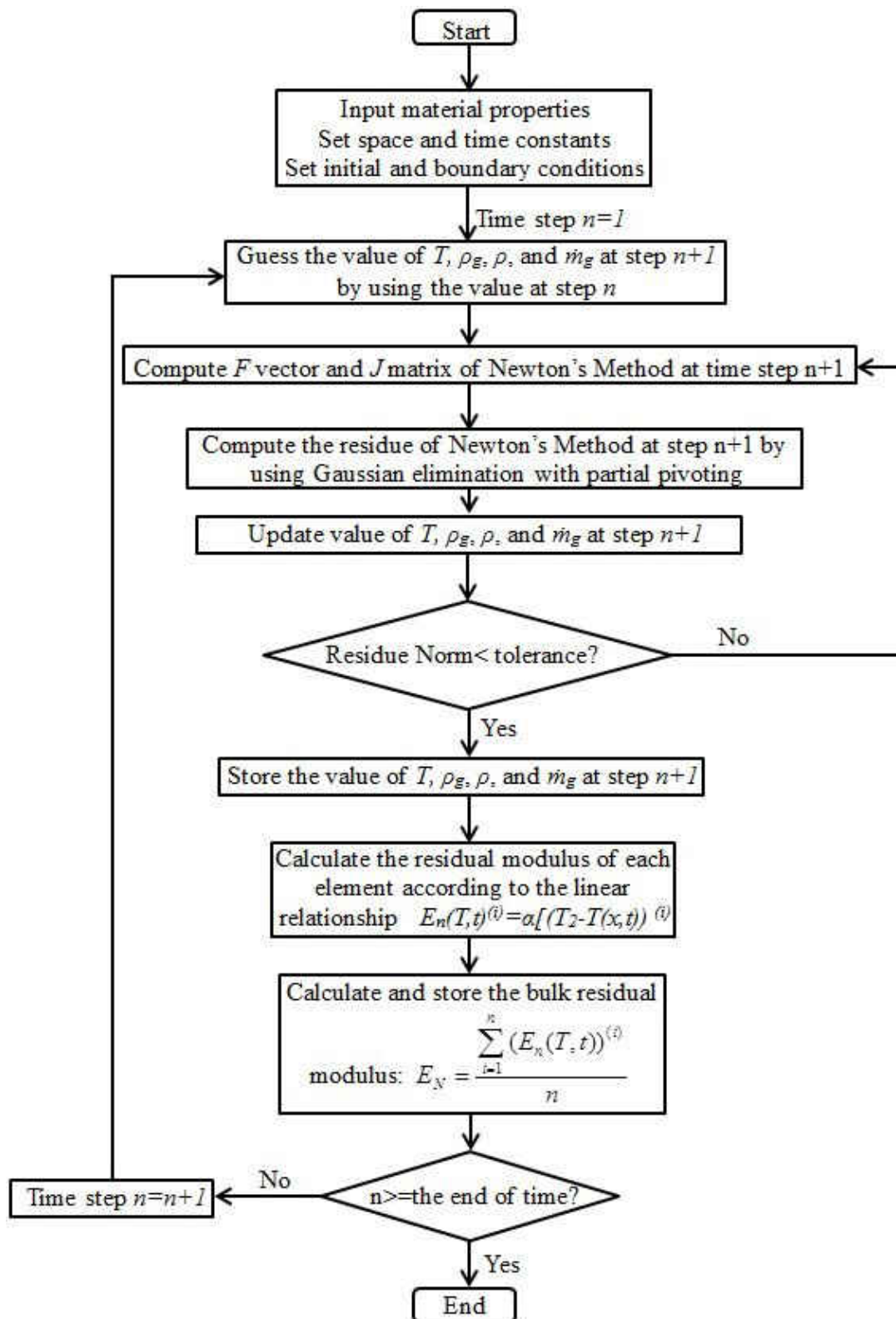


Figure 64 Computational algorithm of the FD model.

6.3. Input Parameters, Initial Conditions, and Boundary Conditions

The accuracy of the model predictions not only depends on the mathematical equations mentioned above, but also on the accuracy of the input parameters. Unfortunately, the material properties such as specific heat and thermal conductivity were assumed to be temperature-independent due to the limited thermo-physical parameters available for the glass fiber reinforced polyester composites in literature. The parameters including specific heat, thermal conductivity, heat of decomposition, and reaction order of the thermal decomposition process were obtained from the research papers of Looyeh *et al* [124] and Krysl *et al* [126]. And the viscosity, molecular weight, and thermal conductivity of the gas of H41N phenolic were used to approximately simulate the decomposed gas from polyester [159]. The porosity and gas permeability of the virgin and char states of laminate were obtained from the recent study presented by Goodrich and Lattimer [137]. Arrhenius kinetic constants were readily determined by fitting the TGA curve and had already been calculated in previous chapter. The coefficient α and the temperature T_2 at which the composites have zero mechanical resistance have also been discussed and determined. The input material properties used in this study were summarized in Table 16.

Table 16 Input parameters of the materials.

Parameters (Definition)	Value (Unit) [Ref.]
A (Pre-exponential factor)	1000 (s ⁻¹) [Chapter 5]
c _{pf} (Specific heat of glass fiber)	760 (J.kg ⁻¹ .K ⁻¹) [125]
c _{pr} (Specific heat of polyester resin)	1600 (J.kg ⁻¹ .K ⁻¹) [125]
c _{pg} (Specific heat of decomposed gas)	2386.5 (J.kg ⁻¹ .K ⁻¹) [125]
E _a (Activation energy)	50000 (J.g ⁻¹ .mole ⁻¹) [Chapter 5]
k _f (Thermal conductivity of glass fiber)	1.04 (J.m ⁻¹ .K ⁻¹ .s ⁻¹) [125]
k _r (Thermal conductivity of polyester resin)	0.20 (J.m ⁻¹ .K ⁻¹ .s ⁻¹) [125]
k _g (Thermal conductivity of gas)	0.03 (J.m ⁻¹ .K ⁻¹ .s ⁻¹) [159]
Q (Heat of decomposition)	-234460 (J.kg ⁻¹) [125]
V _f (Glass fiber volume fraction)	30%
L (Thickness of the composites)	3.5 (mm)
ρ _f (Density of glass fiber)	2694.7 (kg.m ⁻³)
ρ _r (Density of polyester resin)	1102.4 (kg.m ⁻³)
ρ _v (Density of virgin composites)	1580 (kg.m ⁻³)
n (Reaction order)	1 [125]
φ _v (Porosity of the virgin laminate)	0.1 [137]
φ _{ch} (Porosity of the char laminate)	0.68 [137]
μ (viscosity of the gas)	1.48x10 ⁻⁵ (kg.s ⁻¹ .m ⁻¹) [159]
r _v (Gas permeability of the virgin laminate)	1x10 ⁻¹⁷ (m ²) [137]
r _{ch} (Gas permeability of the char laminate)	1x10 ⁻¹⁰ (m ²) [137]
M (molecular weight of the gas)	18.35 (g.gmole ⁻¹) [159]
T ₂ (up limit of the temperature)	573 K [Chapter 5]
α (post-fire flexural moduli coefficient)	1.674 [Chapter 5]

As specified in the sample preparation section, the initial conditions for the four sets of unknowns discussed in the model construction section were set to be:

$$\rho_g=0, T=T_0, \dot{m}_g=0, \rho=\rho_0 \text{ for } 0 \leq x \leq l \text{ at } t=0 \quad (6-12)$$

where T_0 and ρ_0 were equal to the room temperature and virgin density of the composites, respectively.

The surface of the sample was composed of CNF, xGnP, APP, and polyester resin,

therefore the reaction within the surface layer was very complicated. And the coating in this study was modeled as a regulator, imposing the surface temperature which was measured by the thermocouple beneath the nanopaper coating. Therefore, the boundary conditions for the exposed surface were:

$$T_s=T(t); P_s=P_{atm}=10^5 Pa \text{ for } x=0 \text{ when } t>0 \quad (6-13)$$

where P_{atm} was the pressure of atmosphere.

The measured temperature profiles of the surface and their 4th order polynomial ($T(t) = A_1 + A_2t + A_3t^2 + A_4t^3 + A_5t^4$) curve fitting is shown in Figure 65. The coefficients of the fitting equation are summarized in Table 17.

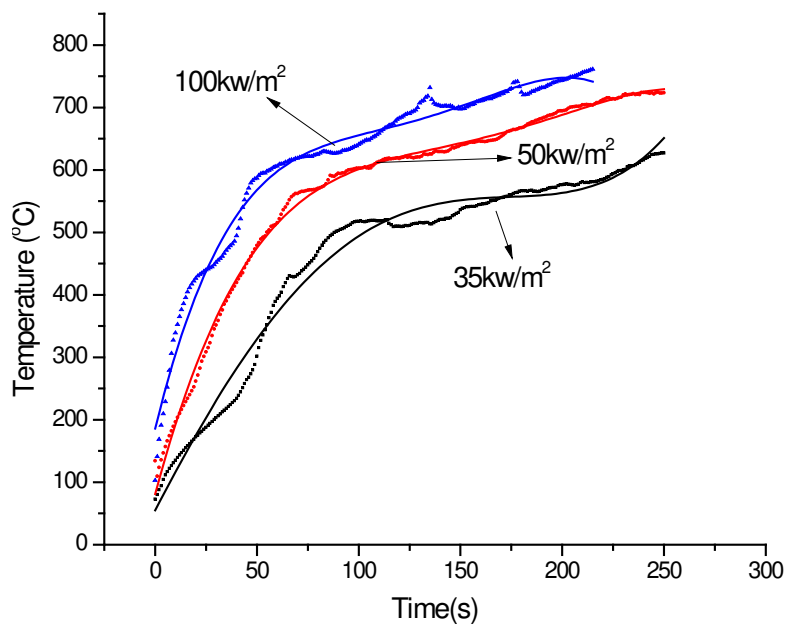


Figure 65 Fourth Order polynomial fitting of the surface boundary conditions.

Table 17 Curve fitting parameters of the surface boundary conditions.

	A1	A2	A3	A4	A5
35 kw/m ²	30.42	8.494	-0.054	1.628e ⁻⁴	-1.82e ⁻⁷
50 kw/m ²	86.9	11.7778	-0.09944	3.873e ⁻⁴	-5.49e ⁻⁷
100 kw/m ²	185.436	13.31945	-0.148	7.592e ⁻⁴	-1.41e ⁻⁶

The boundary conditions for the cold (unexposed) surface, which was thermally and structurally insulated, were:

$$k_g \phi \frac{\partial T}{\partial x} + k(1-\phi) \frac{\partial T}{\partial x} = 0, \dot{m}_g = 0 \text{ for } x=l \text{ when } t>0 \quad (6-14)$$

In addition, for the 1-D finite difference model presented in this study, the solution domain in the thickness direction was divided into 20 elements, each with the same length of 0.175mm. The time step was chosen to be 0.5 seconds and the model was computed until the remaining mass becomes stable, namely, the decomposition process was completed (as the model was valid only when there was decomposition reaction).

6.4. Verification and Discussion

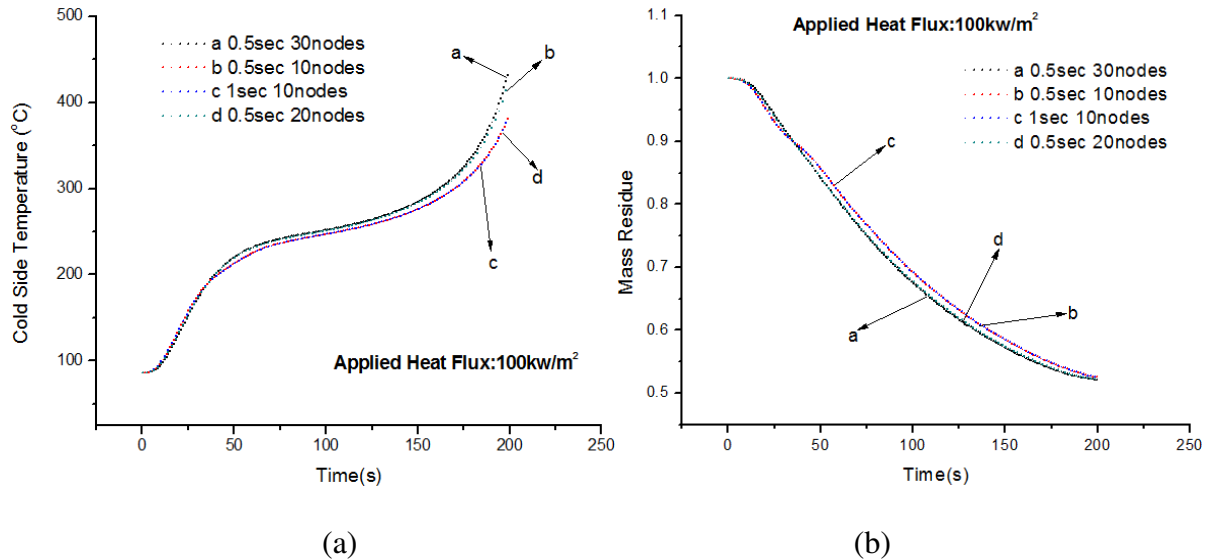


Figure 66 Convergence study of the FD model. (a) cold side temperature prediction; (b) remaining mass prediction.

The convergence study of the FD model presented in this study is shown in Figure 66. As indicated by the figure, the convergence of the model is achieved when the number of nodes increases from 10 nodes to 20 nodes. The predicted results between 20 and 30 nodes model are almost indistinguishable from each other. However, it is interesting to note that the model is relatively insensitive to time, as the predicted results between the 0.5 seconds 10 nodes and 1 second 10 nodes are almost identical.

Figure 67 (a) shows the predicted temperature for those nanopaper coated samples subjected to the 100kw/m^2 heat flux as a function of time and locations. The 3-D plot indicates that the calculated data are in good agreement with the expected physical behavior. Higher temperatures were at the front surface and lower temperatures were at the back

surface. The temperature gradually increases with time. The zero slope, as shown in Figure 67 (b), for the data at the back surface, illustrating the insulated boundary condition. The evolution of porosity of the sample subjected to various heat fluxes is shown in Figure 67 (c). As indicated by the figure, porosity increases with the increase of exposure time and the increase rate is higher at higher heat fluxes.

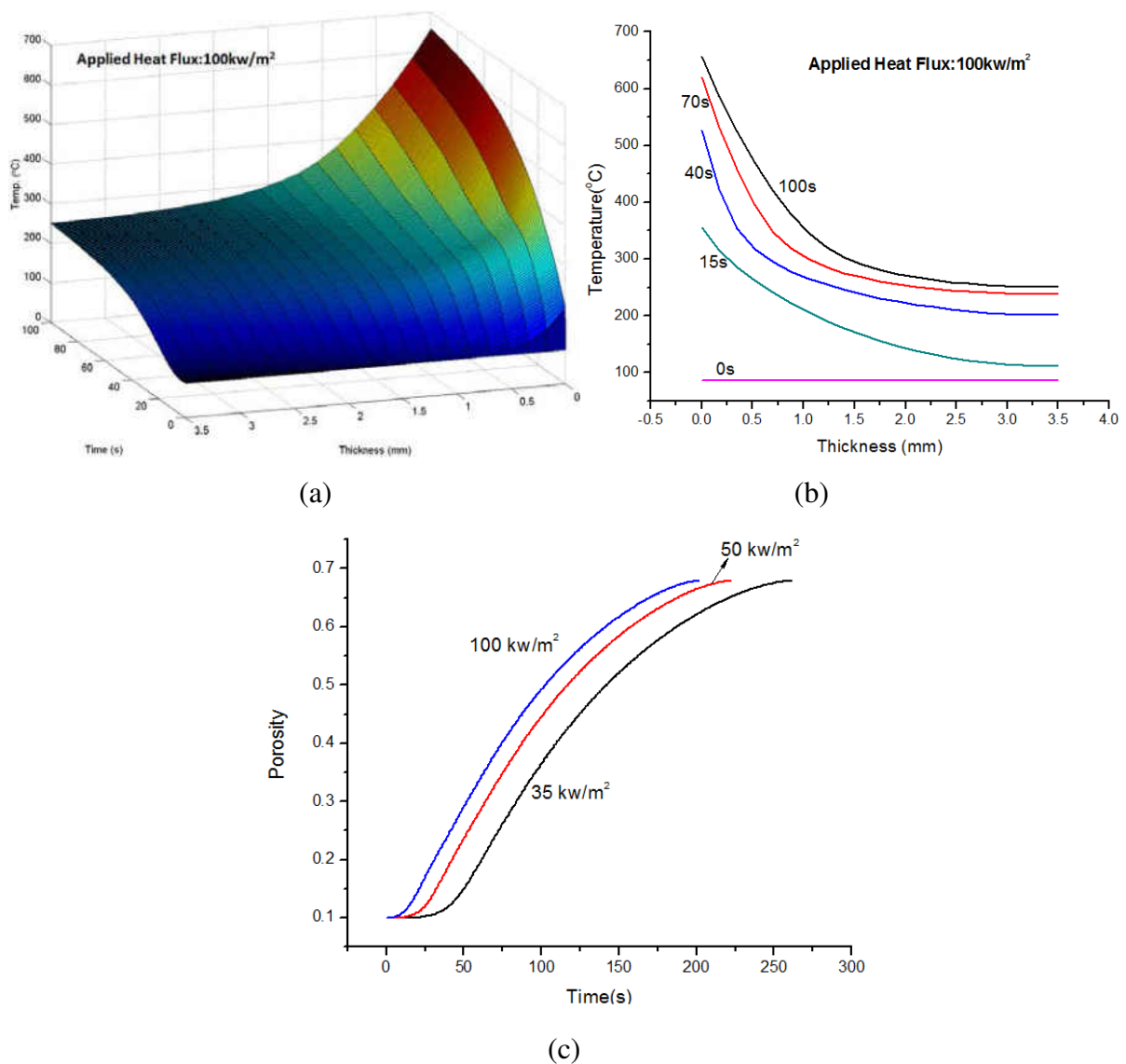
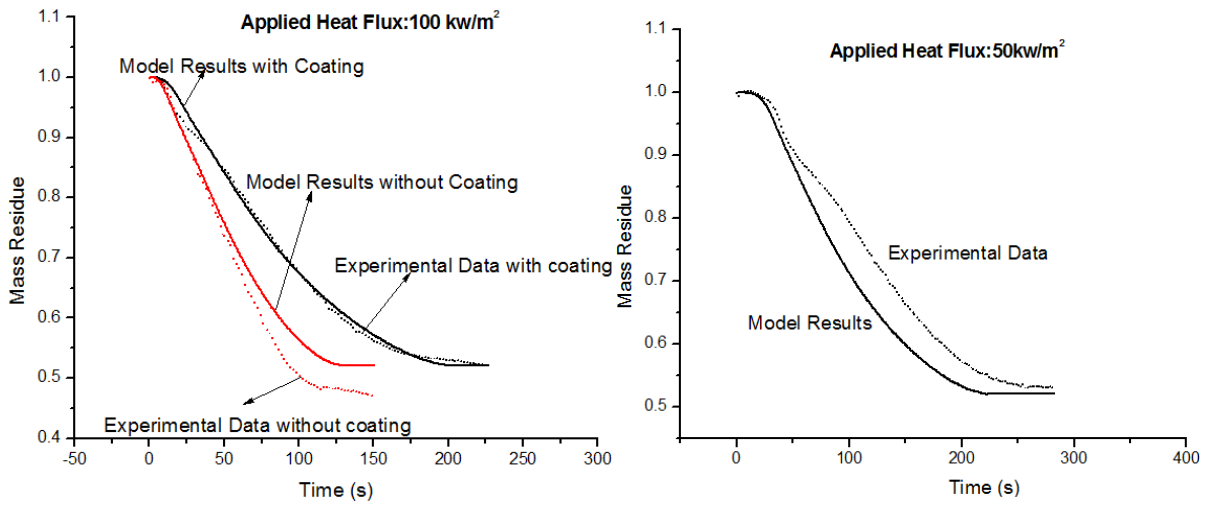
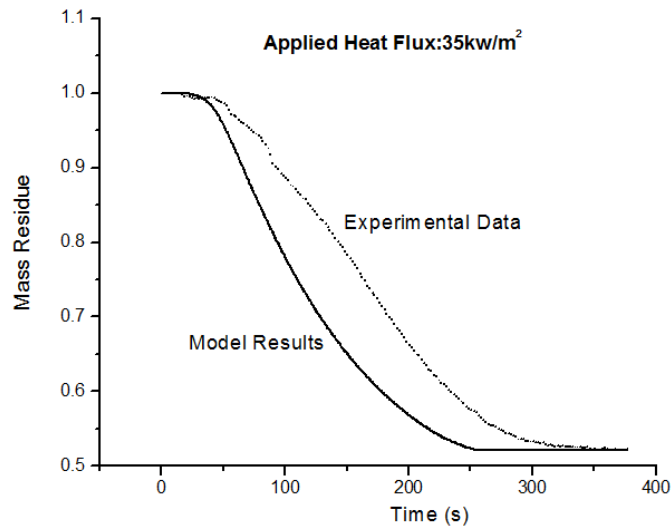


Figure 67 Model results. (a) 3-D Temperature profile as a function of thickness and exposure time; (b) temperature evolution as a function of thickness; (c) porosity evolution as a function of exposure time.



(a)

(b)



(c)

Figure 68 Comparison of experimentally measured ratio of remaining mass with numerical predictions.

The remaining weight ratios are shown in Figure 68. As expected, when the applied heat flux increases, the time where the entire polymer matrix been degraded (there is no change in mass residue) occurs earlier (roughly 190s for 100kw/m², 220s for 50kw/m², and 250s for 35kw/m²). Furthermore, since no glass fiber damage is taken into account in this

model, all of the predicted results show approximately the same 52% of residue, which equals the weight percentage of glass fiber within the composites. The comparison of the model predictions, as well as the experimental data between nanopaper coated and uncoated samples shown in Figure 68 (a), suggests that the coating has effectively slowed down the rate of mass loss. This is very important to the structural integrity of the composites, with a lower mass loss rate meaning a smaller amount of fuel supply to the flame. This leads to the lower rate of structural temperature increase, and thus better structural integrity of the composites. For the case of the composite samples without nanopaper protection, the experimental remaining mass data is lower than the calculated value at the end of degradation process due to the possible damage of upper layer glass fiber mats (Figure 47.), where the temperature could reach upwards of 950°C, much higher than the softening temperature (about 830°C) of the glass fiber. However, this phenomenon does not occur for the nanopaper coated samples, indicating the efficiency of the nanopaper protection.

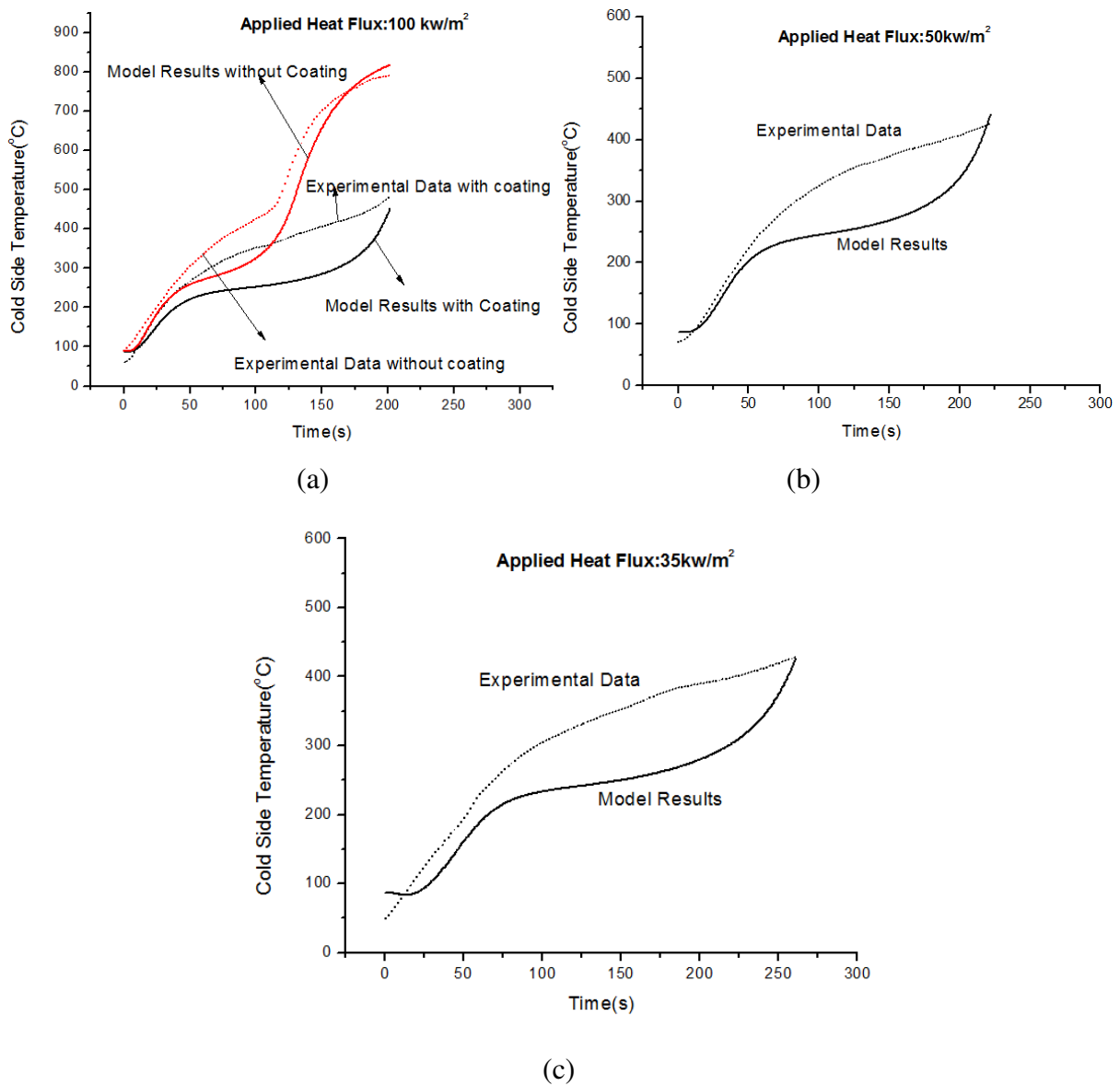
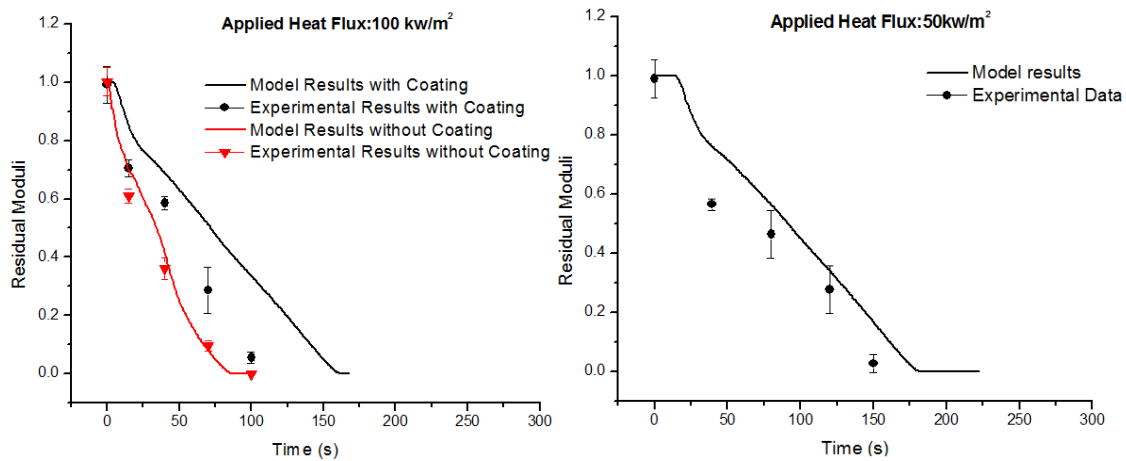


Figure 69 Comparison of experimentally measured temperature with numerical predictions.

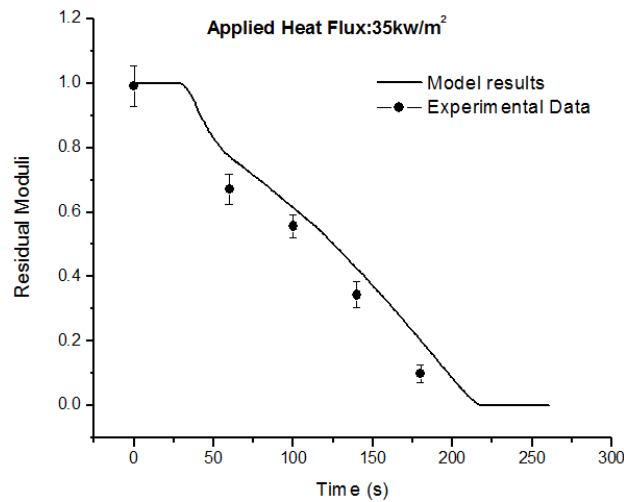
As the model is valid only for the decomposition process of the composites, the calculation of temperature stops when the remaining mass does not change, namely, no more degradation is taking place. Figure 69 shows the comparison of temperature between the predicted results and experimentally measured back side temperature data. As shown in

Figure 69 (a), nanopaper coated sample exhibited lower rate of mass loss (thus less fuel supply to the flame) than that of the control sample, both the experimental data and model prediction show that the cold side temperature of the nanopaper coated samples is higher than that of the control sample. However, all the predicted results showed lower temperature than the experimental data. The errors arising from the input material parameters aside, another possible reason associated with the imbedding of the thermocouples as discussed in the last chapter. Considering these factors, a higher cold side temperature might be recorded. Nevertheless, the behavior of the cold side temperature predicted by the model agrees well with the experimental data. Initial fast increase in temperature when the thermal response is dominated by heat conduction, followed by slow increase in temperature when dramatic endothermic reaction take place, and then followed by fast increase in temperature when most of the polymer matrix has been decomposed and the thermal response is again dominated by heat conduction. Considering the complicated nature of the decomposition process, which includes not only the decomposition of the polymer matrix, but also the chemical reaction within the coating layer that is composed by APP, xGnP, CNF, and polyester, the overall results of the model prediction are reasonable. However, the accuracy of the model can be further improved by providing more accurate input parameters and with refined coating layer model.



(a)

(b)



(c)

Figure 70 Comparison of experimentally measured flexural moduli with numerical predictions.

Figure 70 shows the comparison of residual flexural moduli between the value predicted by the model and experimental data. As discussed previously that the nanopaper coated samples experienced slower rate of mass loss than that the control samples, therefore, as shown in Figure 70 (a), the former samples also have higher post-fire flexural moduli than the latter ones. The results indicate that the temperature dependent numerical model

prediction has achieved acceptable accuracy for the samples subjected to 35 and 50kw/m² of heat flux, while the prediction for the 100kw/m² case is not as accurate as the former two cases. The possible reason may be attributed to the fact that parameters T_2 and α were inversely derived in the case of 35kw/m², even though the parameters worked well as heat flux independent in the model discussed in Chapter 5, where no nanopaper was introduced, they are not accurate enough to describe the post-fire flexural moduli of the composites samples coated with nanopapers and subjected to 100kw/m², suggesting the parameters are not only temperature-dependent, but also temperature increase rate dependent. Therefore, the accuracy of the post-fire mechanical model probably could be improved by including the influence of temperature increase rate.

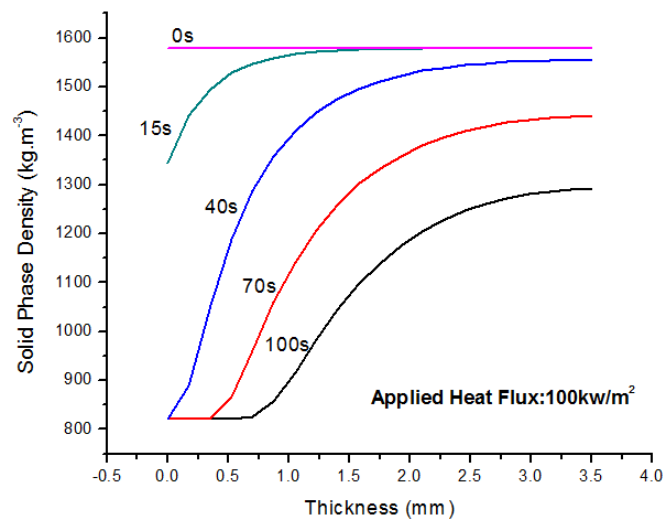


Figure 71 Model results of solid phase density.

Figure 71 shows the evolution of the solid phase density of the composite material subjected to heat. As expected, the density gradually decreases as the exposure time increases

and the upper layers of the sample first reach a stable value as the polymer matrix has been completely decomposed, leaving behind only the more thermally stable reinforced glass fiber.

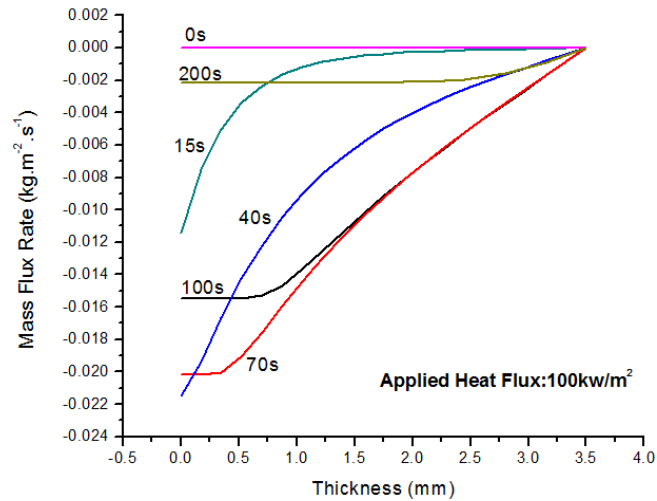


Figure 72 Model results of mass flux rate.

Figure 72 depicts the mass flux rate through the material. The model results clearly indicate that the decomposed gases flow toward the heat exposed surface and the unexposed bottom surface experiences no gas flow because the surface is insulated. In addition, the figure also indicates that the value of mass flow gradually increases to a peak and then drops back. This is the expected behavior since the decomposition reaction of the polymer matrix will become more dramatic as the reaction proceed and the matrix will eventually be decomposed completely, resulting the decrease of the reaction rate. Furthermore, compared to the solid state density, the value of mass flow is relatively small, indicating its impact on the thermal response of the material should be limited.

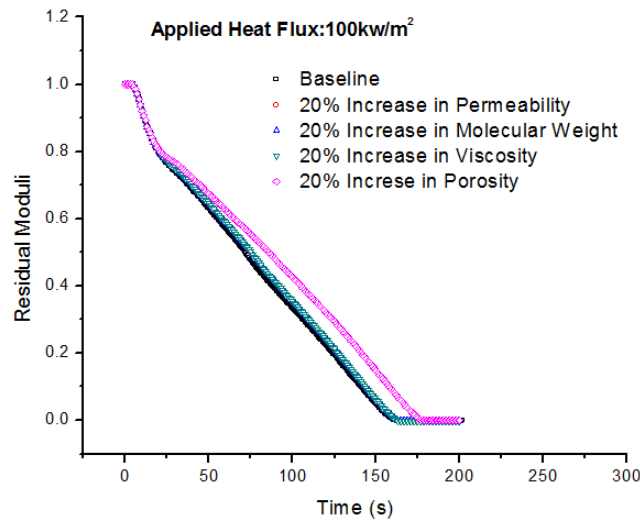


Figure 73 Impact of the input parameters on the residual moduli predictions.

In order to verify the above statement, a parametric study was carried out. As suggested by equation (6-6), the mass flux rate is determined by the permeability of the material, viscosity of the decomposed gas, and the molecular weight of the decomposed gas. As shown in Figure 73, when all of these parameters are increased by 20% separately, the difference in the predicted residual moduli with the baseline results is very small. However, the impact of porosity on the residual moduli is more profound than that of the former parameters. The porosity of the material not only influences the mass flux rate (as suggested by equation 6-4), but also directly governs the energy equation (equation 6-3). As a result, when the porosity is increased by 20%, the residual moduli also have clear increment. This result agrees with the expected physical behavior, since the increase in porosity will decrease the thermal conductivity of the structure, and the temperature increase rate within the structure will be reduced, leading to the improved structure integrity.

6.5. Conclusions

A thermal response FD model of the composites coated with the nanopaper subjecting heat flux was developed. This model has taken the permeability and porosity of the composites into account. Additionally, the thermal response model was coupled with the temperature-dependent residual modulus. In general, the results predicted by the model showed reasonable agreement with the experimental data and the expected physical behaviors. It was suggested that the nanopaper coating considered as the regulator to impose the surface boundary condition had successfully reduced the mass loss of the material in fire scenario. Specifically, the reduction in mass loss has led to the decrease in cold side temperature, resulting in an improved post-fire mechanical property of the composites structure. In addition, the parametric study of the model suggests that the porosity of the material has profound influence in the residual moduli of the composites, thus also in the thermal response, and therefore has to be taken into account. Nevertheless, the accuracy of the model can be further improved if more precise material parameters were provided and if the diameter of the thermal couples could be neglected when compared to the thickness of the composites samples.

CHAPTER 7 CONCLUSIONS AND FUTURE WORK

7.1. Conclusions

This dissertation presents the experimental and computational study of PMCs subject to heat flux. The contributions of this work can be summarized as:

1. Various types of nanopaper have been developed and coated onto the PMCs, which can improve the fire retardant performance of PMCs up to 100%. The flammability results show that CNF/xGnP/APP hybrid nanopaper revealed better performance under higher level of heat flux, indicating its potential for the ablation applications. The fire retardant mechanism, namely, the hybrid nanopaper, which successfully inhibits the diffusion of decomposed gases and the heat transfer process, has been studied.
2. The FE and FD models have been developed and have the capability of defining the relative impact of parameters (*e.g.* thermal decomposition of polymer, flow of gas, and porosity and permeability of the composite structure) on the thermo-mechanical degradation of materials. Compared to the existing post-fire mechanical models, the accuracy of the predictions by the temperature dependent post-fire mechanical models in this work has been improved by more than 100%. From the point of view of material design, the models indicate that the thickness and porosity of the composite have a profound impact on its thermo-mechanical

response.

7.2. Fire Retardant Hybrid Nanopaper Design and Optimization

7.2.1. Improving the expansion rate of hybrid nanopaper

The assumption presented in this study is that if one could manage to create a “pre-existing char layer” (which would otherwise form slowly during the combustion process on the surface of the composites) that has proper permeability and thermal properties to retard polymer mass loss and heat conduction under fire conditions, the goal of flame retardancy could possibly be accomplished. A designated “pre-existing char layer”, namely, the carbon nanofiber-based hybrid paper was designed. As the name might imply, the major element of the nanopaper was CNFs. They could structurally support the nanopaper, therefore making it easier to handle. Simultaneously, the CNFs were expected to stimulate the pyrolysis of flame retardants, spurring the formation of char due to their high thermal conductivity and heat absorption. In addition, the CNFs themselves were thermally stable materials, which indeed made the paper behave as a “pre-existing char layer”. Ammonium polyphosphate (APP), a traditional intumescent flame retardant, had been incorporate into the nanopaper. Ideally, the APP particles (the gas source as described in Chapter 2) should expand when subjected to heat, which should thicken the nanopaper, resulting in a reduction in through-thickness thermal conductivity, thereby enhancing the thermal shielding effects of the char layer. Furthermore, APP particles (also the carbon and acid source) are believed to produce and promote char formation when exposed to heat. Unfortunately, the type of APP used in this

study tends to be hydrophilic. It was found that the APP powders ran the risk of decomposing into smaller particles during sonication, potentially preventing their inclusion in the nanopaper during filtration. As a result, instead of directly mixing them with CNFs in the sonication process, they were mixed into the polymer matrix using a mechanical shear mixer, and then the paste was brushed onto the back surface of the dry paper. Even though the weight ratio of the paste for APP and resin was carefully controlled (in order to balance the viscosity of the paste and the amount of resin being used) and a 250psi pressure was used to carry out the RTM process, the amount and dispersion of APP into the nanopaper must not have reached the desirable level, which resulted in deteriorated flame retardant efficiency. In fact, by observing the cone calorimeter tests, it was found that the expansion ratio of the nanopaper under heat condition was limited. Therefore, in order to maximize the contribution of APP in the fire retardant system, the direct mixing of APP, CNFs, and other nanoparticles when fabricating hybrid nanopaper is probably a better approach and a hydrophobic type of APP is highly desirable in this case. In fact, Weil had indicated that there were many variations on APP, including low molecular weight, water-soluble and high molecular weight, water-insoluble versions. The former version was used primarily for non-durable cellulosic flame-retardant textile finishes. The latter version, sometimes called Phase II APP (there is a Phase I APP which is water-insoluble but relatively hydrolysable and is used in coatings where water resistance is not needed), was preferred for use in coatings. And this type of APP should be used in the hybrid nanopaper system in future research [101].

7.2.2. Optimizing the heat transfer property of hybrid nanopaper

Within the nanopaper, the planar-structured particles-xGnP were also introduced, aimed at lowering its permeability and convoluting the path for the decomposed polymer (fuel), which inhibited the mass loss from the polymer degradation. The inclusion of xGnP particles was also to take advantage of their anisotropic thermal conductivity ($K_{\parallel}=3000\text{W/m}$, $K_{\perp}=6\text{W/m}$), so it was expected that the heat could be easily dissipated transversely during the heat transfer process in fire, with less heat penetrating through the coating. It was clear that this expectation was based on the assumption that the xGnP particles should be laid in a parallel position within the nanopaper. Unfortunately, due to limited resources, this assumption has not been confirmed. Therefore, in future research, the structure of the nanopaper should be characterized more carefully, particularly the lay-up details of the xGnP particles. However, if the morphology examination had failed to provide the evidence for the assumption, it would be desirable to design and carry out necessary experiments to align the xGnPs and, if possible, CNFs. The outcome of the alignment should maximize the anisotropic thermal conductivity of the nanopaper. There have been numerous studies trying to align the CNTs, which might inspire the alignment of xGnPs and CNFs:

(a) Ex situ alignment

The term “ex situ” refers to the alignment of CNTs that has already been achieved before fabricating CNT/polymer nanocomposites. This method is adopted by the in situ polymerization process, during which, the placements of CNTs will not be disturbed.

Therefore, the challenge is aligning the CNTs beforehand. One can obtain aligned CNTs by filtration process, during which, the CNTs are first dispersed within solutions such as water, ethanol, and acetone. Then, they are aligned by high pressure filtration through a selected medium [160-161]. Another method is by using the so called plasma-enhanced chemical vapor deposition process. In this process, the CNTs are synthesized in an aligned direction [162-163]. One can also align CNTs by manipulating the template used in the chemical vapor deposition (CVD) process. In many cases, porous substrates are required and CNTs are grown within the pores [164-165]. Nevertheless, Yanagi *et al* reported self-oriented short SWCNTs were deposited on highly oriented pyrolytic graphite (HOPG) that served as a template [166].

(b) Induced alignment

There are many ways to induce the alignment of CNTs. One of which is align CNTs in a force field such as a field of shear force. Ajayan *et al* developed a simple method to align CNTs through flow-induced anisotropy (the nature of rheology in composite media). However, their approach is only suitable for fabricating thin film because the alignment effect becomes less pronounced with increasing the thickness of composite slices [167]. Vigolo *et al* were able to fabricate meter-long ribbons by injecting low viscous SWCNT solution into a high viscous PVA solution using a syringe [168]. Because of the difference in viscosity, shear force was induced and SWCNTs were rapidly stacked together as they were injected out from the syringe needle. Other processes for shear force induced alignment can be achieved

through stretching or extrusion [169].

Another approach to induce the alignment of CNTs can be achieved by a magnetic field. The degree of the alignment can be customized by controlling the intensity of the magnetic field. Kimura *et al* were the first to utilize a high magnetic field to prepare anisotropic CNT/polymer nanocomposites [169]. In their research, a constant magnetic field of 10T was applied to MWCNTs/unsaturated polyester solution. Then the solution was polymerized under the magnetic field such that the aligned MWCNTs were freezed within the polyester matrix. Similar to the principal of the magnetic field induced alignment, CNTs can also be aligned by electrospinning. In this method, there is a high direct current voltage been generated between a negatively charged CNT/polymer fluid and a positive metallic fiber collector. The CNTs are, initially, randomly oriented. Because of the “sink-like” flow that been generated in a wedge-like electrospun jet, the CNTs are gradually aligned along the streamlines [170].

Besides the force induced alignment, CNTs can also be aligned by the geometric constraints (created by a liquid crystalline phase). Due to the unique properties of the liquid crystals, their geometries can be easily modified by the force, magnetic and electric field. This principal was adopted by Lynch *et al*. They aligned MWCNTs by using a liquid crystal matrix that had been oriented in an electric field [171].

In addition to that, the in plane and through thickness thermal conductivity of the nanopaper should be determined. This is necessary to confirm whether the thermal

conductivity anisotropy of the nanopaper is so remarkable that the in plane heat dissipation has a major contribution to the flame retardancy. It is also recommended to carry out medium scale fire response tests, where the composites should be exposed to localized heat, and the ignition time should be recorded. If the ignition time of the composites coated with the nanopaper was delayed compared to the control samples, then the in-plane heat dissipation of the coating was demonstrated.

7.3. Thermo-mechanical Degradation Model Improvement

7.3.1. Improving the accuracy of the input material parameters

The thermo-mechanical degradation model was numerically solved with FEM in Chapter 5 and FDM in Chapter 6. Compared to the model in Chapter 5, where no structural properties of the composites were taken into account, the model was improved in Chapter 6. However, there are still many aspects need to be refined. The accuracy of the model predictions not only depends on the mathematical equations, but also the accuracy of the input parameters. Unfortunately, due to limited thermo-physical parameters available for the glass fiber reinforced polyester composites in open literature, the material properties such as the specific heat and thermal conductivity were assumed to be temperature-independent. The parameters of the composites during the degradation process were calculated by the rule of mixture. In the model presented in Chapter 6, the viscosity, molecular weight, and thermal conductivity of the gas of H41N phenolic were used to approximately model the decomposed gas from polyester. All these, more or less, compromise the accuracy of the model predictions.

Therefore, many refined work could be done in terms of estimating the material parameters. For example, for the E-glass vinyl ester laminates, Lua *et al* had improved the Henderson's model by introducing the temperature and mass dependent material parameters [128]. And the morphology, porosity, and gas permeability of the composite laminates during the thermal degradation process were carefully analyzed by Goodrich and Lattimer [137]. The similar work could be done to estimate the material parameters for the 30vol% E-glass fiber reinforced polyester composites used in this dissertation.

For the prediction of the flexural modulus, the temperature dependent model has proved to be superior to that of the two-layer model as discussed in Chapter 5. It was found that the parameters T_2 and α may also be temperature increment rate dependent. Therefore, even though the parameters worked well as heat-flux-independent in the model discussed in Chapter 5, where no nanopapers were introduced, they were not accurate enough to describe the post-fire flexural moduli of the composites samples coated with nanopapers and were exposed to 100kw/m^2 of heat flux. As suggested in Chapter 6, the accuracy of the post-fire mechanical model could be improved by including the influence of the temperature increase rate.

Besides the material parameters, the reliability of measured results to verify the model prediction in this dissertation could also be improved in future study. As noted previously, for the type of the thermocouples used in this study, one notable shortcoming is that their diameters are about 0.51mm, while the total thickness of a nanocomposites sample is only

about 3.5mm. Considering these factors, a higher cold side temperature might be recorded. In fact, numerical study in Chapter 5 showed that the thickness would greatly affect the temperature distribution. A better way to conduct this experiment in future is using thicker composites panels or thermocouples with smaller diameter, such that the impact of the thermocouple's diameter in the temperature measurement could be neglected.

7.3.2. Refining the thermal response model

The thermal degradation model of PMCs coated with nanopaper presented in Chapter 6 treated the nanopaper coating as a regulator to impose a temperature boundary condition. And the temperature was measured by thermocouples located beneath the nanopaper. However, by doing so, the thermal responses and interactions of the nanoparticles within the coating layer was neglected. This information could be important for the coating design. Therefore, the detailed model should be developed to simulate the thermal response of the coating layer. While there have been numerous research papers that deal with the thermal response modeling of a composites panel coated with an intumescent coating [130-136], the modeling of the nanopaper that composed by APPs, CNFs, xGnPs, and polyester resin should be different and could be challenging. However, those studies could provide useful guidelines. If allowable, a molecular dynamic simulation package could be very helpful.

REFERENCES

- [1] P.K. Mallick. Fiber-reinforced composites: materials, manufacturing, and design. Third edition. CRC Press. 2007.
- [2] J. Hale. Boeing 787 from the Ground Up. *Aero*. 2006; 4: 17-24.
- [3] F. Mutel. Global Market Scenario: Dynamics of the composites industry. JEC Composites. 2009.
- [4] M.J. Karter. Fire loss in the united states during 2009. National fire protection association. Quincy, MA, August 2010.
- [5] I. Glassman, R. A. Yetter. Combustion, Forth Edition. Academic Press. Burlington. 2008.
- [6] J. Troitzsch. International Plastics Flammability Handbook, 2nd Ed. Hanser Publishing. New York. 1990.
- [7] Fire-safe polymers. http://en.wikipedia.org/wiki/Fire-safe_polymers.
- [8] M.P. Stevens. Polymer Chemistry: An Introduction. Oxford University Press. Oxford. New York. 1999.
- [9] G. Camino, L. Costa, M. P. Luda di Cortemiglia. Overview of fire retardant mechanisms. *Polymer Degradation and Stability*. 1991; 33: 131-154.
- [10] Q. Wu, W. Zhu, C. Zhang, Z. Liang, B.Wang. Study of fire retardant behavior of carbon nanotube membranes and carbon nanofiber paper in carbon fiber reinforced epoxy composites. *Carbon*. 2010; 48: 1799-1860.

- [11] Y. Lind, P.O. Darnerud, S. Atuma, M. Aune, W. Becher, R. Bjerselius, S. Cnattingius, A. Glynn. Polybrominated diphenyl ethers in breast milk from Uppasla County, Sweden. *Environmental Research*. 2003; 93(2): 186-194.
- [12] K.S. Betts. New Thinking on Flame Retardants. *Environmental Health Perspectives*. 2008; 116: 210-213.
- [13] K.L. Kimbrough, W.E. Johnson, G.G. Lauenstein, J.D. Christensen, D.A. Apeti. An Assessment of Polybrominated Diphenyl Ethers (PBDEs) in Sediments and Bivalves of the U.S. Coastal Zone. Silver Spring, Maryland, 2009.
- [14] L.A. Norris, W.L. Webb. Effects of Fire Retardant on Water Quality. USDA Forest Service Gen. Tech. Rep. PSW-109. 1989; 79-86.
- [15] G. Beyer. Nanocomposites: a new class of flame retardants for polymer. *Plastics, Additives and Compounding*. 2002; 4: 22-28.
- [16] D. Porter, E. Metcalfe, M.J.K. Thomas. Nanocomposite Fire Retardants - A Review. *Fire Mater*. 2000; 24: 45-52.
- [17] S. Bourbigot, S. Duquesne, C. Jama. Polymer Nanocomposites: How to Reach Low Flammability. *Macromol. Symp*. 2006; 233: 180-190.
- [18] New Thinking on Flame Retardants. *Environmental Health Perspectives*. 2008; 5: 116.
- [19] T. Kashiwagi *et al*. Nanoparticle networks reduced the flammability of polymer nanocomposites. *Nature Materials*. 2005; 4: 928-933.
- [20] T. Kashiwagi *et al*. Relationship between dispersion metric and properties of

- PMMA/SWNT nanocomposites. *Polymer*. 2007; 48: 4855-4866.
- [21] B. H. Cipiriano, T. Kashiwagi *et al.* Effects of aspect ratio of MWNT on the flammability properties of polymer nanocomposites. *Polymer*. 2007; 48: 6086-6096.
- [22] T. Kashiwagi *et al.* Thermal and flammability properties of polypropylene/carbon nanotube nanocomposites. *Polymer*. 2004; 45: 4227-4239.
- [23] T. Kashiwagi. Flammability properties of polymer nanocomposites with single-walled carbon nanotubes: effects of nanotube dispersion and concentration. *Polymer*. 2005; 46: 471-481.
- [24] S.S. Ray, M. Okamoto. Polymer/layered silicate nanocomposites: a review from preparation to processing. *Progress In Polymer Science*. 2003; 28: 1539.
- [25] P.K. Mallick. Fiber-reinforced composites: materials, manufacturing, and design, 3rd ed. CRC Press. 2007; 559.
- [26] L. Jin, C. Bower, O. Zhou. Alignment of carbon nanotubes in a polymer matrix by mechanical stretching. *Applied Physics Letter*. 1998; 73: 1197.
- [27] A. Yasmin, J. Luo, I.M. Daniel. Processing of expanded graphite reinforced polymer nanocomposites. *Composites Science and Technology*. 2006; 66: 1182.
- [28] J.W. Gilman, T. Kashiwagi. Polymer-layered silicate nanocomposites with conventional flame retardant. In: *Polymer-clay nanocomposites*, edited by T. J. Pinnavaia & G.W. Beall. John Wiley & Sons, Inc, 2000; 193.
- [29] Y. Rao, J.M. Pochan. *Mechanics of Polymer-Clay Nanocomposites*. *Macromolecules*.

2007; 40: 290.

- [30] J.N. Coleman, U. Khan, W.J. Blau, Y.K. Gun'ko. Small but strong: A review of the mechanical properties of carbon nanotube-polymer composites. *Carbon*. 2006; 44: 1624.
- [31] K. Yano *et al.* Synthesis and Properties of Polyimide-Clay Hybrid. *Journal of Polymer Science Part A: Polymer Chemistry* . 1993; 31:2493.
- [32] C. Zeng, L.J. Lee. Poly(methyl methacrylate) and Polystyrene/Clay Nanocomposites Prepared by in-Situ Polymerization. *Macromolecules*. 2001; 34: 4098.
- [33] J. Kim, S.M. Hong, S. Kwak, and Y. Seo. Physical properties of nanocomposites prepared by in situ polymerization of high-density polyethylene on multiwalled carbon nanotubes. *Physical Chemistry Chemical Physics*. 2009; 11: 10851.
- [34] F. Yang, Y. Ou, and Z. Yu. Polyamide 6/Silica Nanocomposites Prepared by In Situ Polymerization. *Journal of Applied Polymer Science*. 1997;69: 355.
- [35] J.W. Cho, D.R. Paul. Nylon 6 nanocomposites by melt compounding. *Polymer*. 2001; 42:1083.
- [36] E.T. Thostenson, T.W. Chou. Aligned multi-walled carbon nanotube-reinforced composites: processing and mechanical characterization. *Journal of Physics D: Applied Physics*. 2002; 35: L77.
- [37] <<http://www.sonifier.com>>, sonifier products, Branson ultrasonics corp.
- [38] K. Mukhopadhyay, C.D. Dwivedi, and G.N. Mathur. Conversion of carbon nanotubes to carbon nanofibers by sonication. *Carbon*. 2002; 40: 1373.

- [39] P.C. Ma, N.A. Siddiqui, G. Marom, J.K. Kim. Dispersion and functionalization of carbon nanotubes for polymer-based nanocomposites: A review. *Composites: Part A*. 2010; 41: 1345.
- [40] J. Li, P.C. Ma, W.S. Chow, C.K. To, B.Z. Tang, J.K. Kim. Correlations between percolation threshold, dispersion state and aspect ratio of carbon nanotube. *Advanced Functional Materials*. 2007; 17: 3207.
- [41] X.L. Xie, Y.W. Mai, X.P. Zhou. Dispersion and alignment of carbon nanotubes in polymer matrix: A review. *Materials Science and Engineering R*. 2005; 49: 89-112.
- [42] C. Huggett. Estimation of rate of heat release by means of oxygen consumption measurements. *Fire and Materials*. 1980; 4: 41-65.
- [43] C. J. Hilado. *Flammability handbook for plastic fourth edition*. Technomic Publishing. Lancaster, Pennsylvania. 1990.
- [44] G.G. Tibbetts. *et al.* A review of the fabrication and properties of vapor-grown carbon Nanofiber/polymer composites. *Composites Science and Technology*. 2007; 67; 1709-1718.
- [45] J. W. Gilman. Flame retardant mechanism of polymer-clay nanocomposites. In: *Flame Retardant Polymer Nanocomposites*, edited by A.B. Morgan and C.A. Wilkie. John Wiley & Sons, Inc. 2007. 67-87
- [46] J. H. Koo. *Polymer Nanocomposites: Processing, Characterization, and Applications*. McGraw-Hill Nanoscience and Technology Series. 2006

- [47] J.W. Gilman & T. Kashiwagi. Polymer-layered silicate nanocomposites with conventional flame retardant. In: Polymer-clay nanocomposites, edited by T. J. Pinnavaia & G.W. Beall. John Wiley & Sons, Inc. 2000.193-206
- [48] J. Zhu, C.A. Wilkie. Thermal and fire studies on polystyrene-clay nanocomposites. Polym. Int.. 2000; 49: 1185.
- [49] J. Zhu *et al.* Fire properties of polystyrene-clay nanocomposites. Chem. Mater. 2001;13: 3774.
- [50] J. W. Gilman *et al.* Flammability properties of polymer-layerd-silicate nanocomposites. Polypropylene and polystyrene nanocomposites. Chem. Mater. 2000; 12: 1866.
- [51] A.B. Morgan *et al.* Flammability of polystyrene layered silicate clay nanocomposites: carbonaceous char formation. Fire and Materials. 2000; 26: 247.
- [52] A.B. Morgan *et al.* Abstract of Papers-American Chemical Society. 2000 220th PMSE-064.
- [53] A.B. Morgan *et al.* Flammability properties of polymer-clay nanocomposites: polyamide-6 and polypropylene clay nanocomposites. ACS Symp. Series. 797 Fire and polymers. 2001.
- [54] S. Wang *et al.* Preparation and flammability properties of polyethylene/clay nanocomposites by melt intercalation method from Na⁺ montmorillonite. Mater. Lett. 2003; 57: 2675.
- [55] J.Zhu *et al.* Thermal stability and flame retardancy of polymethyl methacrylate-clay

- nanocomposites. *Polym. Degrad. Stab.* 2002; 77: 253.
- [56] D. Wang, C.A. Wilkie. Preparation of PVC-clay nanocomposites. *J. Vinyl Add. Tech.* 2002; 8: 238.
- [57] D. Wang *et al.* Melt blending preparation of PVC-sodium clay nanocomposites. *J. Vinyl Add. Tech.* 2002; 8: 139.
- [58] D. Wang, C.A. Wilkie. PVC/clay nanocomposites: preparation, thermal and mechanical properties. *J. Vinyl Add. Tech.* 2001; 7: 203.
- [59] M. Zenetii *et al.* Cone calorimeter combustion and gasification studies of polymer layered silicate nanocomposites. *Chem. Mater.* 2002; 14: 881.
- [60] Y. Tang *et al.* Preparation and flammability of ethylene-vinyl acetate copolymer/montmorillonite nanocomposites. *Polym. Degrad. Stab.* 2002; 78: 555.
- [61] J. W. Gilman *et al.* Nanocomposites: a revolutionary new flame retardant approach. *SAMPE J.* 1997; 33: 40.
- [62] A. P. *et al.* Flammability and other characteristics of vinyl ester/clay, vinyl ester/nomex/clay, and vinyl ester/ glass fiber/ clay nanocomposites. *Proc. Int. Conf. On Fire Safety.* 2001; 33: 18.
- [63] J. Lee, E. P. Giannelis. Synthesis and characterization of unsaturated polyester and phenolic resin nanocomposites. *Polym. Prep. Am. Chem. Soc., Div. Polym. Chem.* 1997: 382; 688.
- [64] M.R. Nyden, J.W. Gilman. Molecular dynamics simulations of the thermal degradation

- of nano-confined polypropylene. *Compos. Theor. Polym. Sci.* 1997; 7: 191-198.
- [65] F.W. Uhl *et al.* Polystyrene/graphite nanocomposites: effect on thermal stability. *Polym. Degrad. Stab.* 2002; 76: 111-122.
- [66] F.M. Uhl *et al.* Preparation of nanocomposites from styrene and modified graphite oxides. *Polym. Degrad. Stab.* 2004; 84: 215-226.
- [67] J Zhu *et al.* Thermal and fire studies on polystyrene-clay nanocomposites. *Polym. Int.* 2002; 49: 1158-1163.
- [68] J. Xu *et al.* Thermal analysis of poly (vinyl alcohol)/graphite oxide intercalated composites. *Polym. Degrad. Stab.* 2001; 73: 29-31.
- [69] A. Yasmin *et al.* Mechanical and thermal properties of graphite plated/epoxy composites. *Polymer.* 2004; 45: 8211-8219.
- [70] F.Y. Hshieh *et al.* Flammability testing of flame-retarded epoxy composites and phenolic composites. *Fire Mater.* 1997; 21: 41-49.
- [71] R. Zhang *et al.* Flammability and thermal stability studies of styrene-butyl acrylate copolymer/graphite oxide nanocomposites. *Polym Degrad. Stab.* 2004; 85: 583-588.
- [72] R. Zhang *et al.* Preparation and combustion properties of flame retardant styrene-butyl acrylate copolymer/graphite oxide nanocomposites. *Macromol. Mater. Eng.* 2004; 289: 355-359.
- [73] R. Ding *et al.* Preparation and characterization of polystyrene/graphite oxide nanocomposites by emulsion polymerization. *Polym Degrad. Stab.* 2003; 81: 473-476.

- [74] M. Zanetti *et al.* Cone calorimeter combustion and gasification studies of polymer layered silicate nanocomposites. *Chem. Mater.* 2004; 14: 881-887.
- [75] T. Kashiwagi. Progress in flammability studies of nanocomposites with new types of nanoparticles. In: *Flame Retardant Polymer Nanocomposites*, edited by A.B. Morgan & C.A. Wilkie. John Wiley & Sons, Inc. 285-324.2007
- [76] F.M. Uhl *et al.* Expandable graphite/polyamide-6 nanocomposites. *Polym Degrad. Stab.*2005; 89: 70-84.
- [77] F. M. Uhl *et al.* Formation of nanocomposites of styrene and its copolymers using graphite as the nanomaterial. *Polym. Adv. Technol.* 2005; 16: 533-540.
- [78] S.Iijima, T. Iichashi. Single –shell carbon nanotubes of 1-nm diameter. *Nature.* 1993; 363: 603-605.
- [79] D.S. Bethune *et al.* Cobalt-catalyzed growth of carbon nanotubes with single atomic layer walls. *Nature.* 1993; 363: 605-607.
- [80] T.W. Odom, J. Huang, P. Kim and C.M. Lieber. Structure and electronic properties of carbon nanotubes. *J. Phys. Chem. B.* 2000; 104: 2794-2809.
- [81] E.W. Wong, P.E. Sheehan and C.M. Lieber. Nanobeam mechanics:Elasticity, strength, and toughness of nanorods and nanotubes. *Science.* 1997; 277: 1971.
- [82] M.M.J. Treacy *et al.* Exceptionally high Young's modulus observed for individual nanotubes. *Nature.* 1996; 381: 678.
- [83] R. Saito *et al.* Electronic structure of chiral graphene tubules. *Applied Physics Letters.*

1992; 60: 2204.

- [84] M.S. Dresselhaus *et al.* Carbon nanotubes: synthesis, structure, properties and applications. Springer Verlag, 1st edition.
- [85] Cherng-shii Yeh. A study of nanostructure and properties of mixed nanotube buckypaper materials: fabrication, process modeling characterization, and property modeling. Phd dissertation. FSU. 2007
- [86] A.B. Morgan *et al.* Flammability of polystyrene layered silicate (clay) nanocomposites: carbonaceous char formation. *Fire Mater.* 2002; 26: 247-253.
- [87] R.A. Mantz *et al.* Thermolysis of polyhedral oligomeric silsesquioxane (POSS) macromers and POSS-siloxane copolymers. *Chem. Mater.* 1996; 8: 1250-1259.
- [88] J.J. Schwab *et al.* Polyhedral oligomeric silsesquioxane (POSS)-based polymers. *Appl. Organomet. Chem.* 1998; 12: 707-713.
- [89] Y. Ni *et al.* A novel photocrosslinkable polyhedral oligomeric silsesquioxane and its nanocomposites with poly(vinyl cinnamate). *Chem. Mater.* 2004; 16: 5141-5148.
- [90] R.A. Mantz *et al.* Thermolysis of Polyhedral Oligomeric Silsesquioxane (POSS) Macromers and POSS-Siloxane Copolymers. *Chem. Mater.* 1996; 8: 1250-1259.
- [91] J.C. Huang *et al.* Polyimide/POSS nanocomposites: interfacial, interaction, thermal properties and mechanical properties. *Polymer.* 2004; 44: 4491-4499.
- [92] L. Zheng *et al.* Synthesis and thermal properties of hybrid copolymers of syndiotactic polystyrene and polyhedral oligomeric silsesquioxane. *J. Polym. Sci. A, Polym. Chem.*

2002; 40: 885-891.

[93] S.K. Gupta *et al.* Polyhedral oligomeric silsesquioxane reinforced fire retarding epoxy vinyl ester resins. Int. SAMPE symp. Exhib. 2002; 47: 1517.

[94] E. Devaux *et al.* Polyurethane/clay and polyurethane/POSS nanocomposites as flame retarded coating for polyester and cotton fabrics. Fire Mater. 2002; 26: 149-154.

[95] M. Okoshi, H. Nishizawa. Flame retardancy of nanocomposites. Fire Mater. 2004; 28: 423-429.

[96] J. Zhu, C. A. Wilkie. Flammability Properties of Polymer Nanocomposites. In: Polymer Nanocomposites Handbook, edited by Rakesh K. Gupta *et al.* CRC Press. 2008.

[97] T. Kashiwagi, J.W. Gilman. Silicon-based flame retardants. In: Fire Retardancy of Polymeric Materials, edited by A.F. Grand & C.A. Wilkie. Marcel Dekker. New York. 2000

[98] P. Jash, C.A. Wilike. Effects of surfactants on the thermal and fire properties of poly(methyl methacrylate)/clay nanocomposites. Polym. Degrad. Stab. 2005; 88: 401-406.

[99] J. Hao, W.K. Chow. A brief review of intumescent fire retardant coatings. Architectural Science Review. 2003; 46: 89-95.

[100] F. Liu, W. Zhou. Fire retardant intumescent coating for lignocellulosic materials. U.S. Patent 5968669

[101] E.D. Weil. Fire-protective and flame-retardant coatings-a state of the art review. Journal

- of Fire Sciences. 2011; 29: 259-296.
- [102] U. Sorathia, T. Gracik, J. Ness, A. Durkin, F. Williams, M. Hunstad, F. Berry.
Evaluation of Intumescent Coating for Shipboard Fire Protection. *Journal of Fire Science*.
2003; 21: 423-450.
- [103] U. Sorathia, G. Long, T. Gracik, M. Blum, J. Ness. Screening Tests for Fire Safety of
Composites for Marine Applications. *Fire and Materials*. 2001; 25: 215-222.
- [104] Di Blasi C. Modelling and simulation of combustion processes of charring and
non-charring solid fuels. *Progress in Energy and Combustion Science*. 1993; 19: 71-104.
- [105] J. Staggs. Mathematical Modelling. In: *Fire retardant materials*. Edited by A.R.
Horrocks and D. Price. CRC press. 2001.
- [106] Y. Bai, T. Keller, T. Vallee. Modeling of stiffness of FRP composites under elevated and
high temperatures. *Composites Science and Technology*. 2008; 68: 3099-3106.
- [107] R.J. Asaro, P. Krysal, B. Zhu, W.T. Ramroth. Rate dependent constitutive modeling of
laminated FRP composites degraded by fire. *Composite Structure*. 2005; 68: 399-408.
- [108] R.J. Asaro, B. Lattimer, W.T. Ramroth. Structural response of FRP composites during
fire. *Composite Structure*. 2009; 87: 382-393.
- [109] A.G. Giboson, Y.S. Wu, J.T. Evans, A.P. Mouritz. Laminate theory analysis of
composites under load in fire. *Journal of Composite Materials*. 2006; 40: 639-658.
- [110] S. Feih, A.P. Mouritz, Z. Mathy, A.G. Gibson. Tensile strength modeling of glass
fiber-polymer composites in fire. *Journal of Composite Materials*. 2007; 41: 2387-2410.

- [111] S. Feih, Z. Mathys, A.G. Gibson, A.P. Mouritz. Modelling the tension and compression strengths of polymer laminates in fire. *Composites Science and Technology*. 2007; 67: 551-564.
- [112] S. Feih, Z. Mathys, A.G. Gibson, A.P. Mouritz. Modelling the compression strength of polymer laminates in fire. *Composites Part A; applied science and manufacturing*. 2007; 38: 2354-2365.
- [113] E. Kandare, B.K. Kandola, P. Myler, A.R. Horrocks, G. Edwards. Thermo-mechanical responses of fibre-reinforced epoxy composites exposed to high temperature environment: I. Experimental data acquisition. *Journal of Composite Structures*. 2010; 26: 3093-3114.
- [114] U. Sorathia, C. Beck, T. Dapp. Residual strength of composites during and after fire exposure. *Journal of Fire Sciences*. 1993; 11: 255-269.
- [115] A.P. Mouritz, Z. Mathys. Post-fire mechanical properties of marine polymer composites. *Composite Structure*. 1999; 47: 643-653.
- [116] A.P. Mouritz, Z. Mathys. Post-fire mechanical properties of glass-reinforced polyester composites. *Composites Science and Technology*. 2001; 6: 475-490.
- [117] A.P. Mouritz, S. Feih, E.Kandare, Z. Mathys, A.G. Gibson, P.E.D. Jardin, S.W. Case, B.Y. Lattimer. Review of fire structural modeling of polymer composites. *Composites Part A*. 2009; 40:1800-1814.
- [118] A.G. Gibson, P.N.H. Wright, Y.S. Wu, A.P. Mouritz, Z. Mathys, C.P. Gardiner.

- Modelling residual mechanical properties of polymer composites after fire. *Plastics, Rubber and Composites*. 2003; 32: 81-90.
- [119] T. Keller, C. Tracy, A. Zhou. Structural response of liquid-cooled GFRP slabs subjected to fire-Part I; Material and post-fire modeling. *Composites Part A: applied science and manufacturing*. 2006; 37: 1286-1295.
- [120] Y. Keller, C. Tracy, A. Zhou. Structural response of liquid-cooled GFRP slabs subjected to fire-Part II; Thermo-chemical and thermo-mechanical modeling. *Composites Part A: applied science and manufacturing*. 2006; 37: 1296-1308.
- [121] Y. Ba, T. Keller. Modeling of post-fire stiffness of E-galss fiber-reinforced polyester composites. *Composites Part A: applied science and manufacturing*. 2007; 38: 2142-2153.
- [122] J.B. Henderson, J.A. Wiebelt, M.R. Tant. A model for the thermal response of polymer composite materials with experimental verification. *Journal of Composite Materials*. 1985; 19: 579-585.
- [123] A.G. Gibson, Y.S. Wu, H.W. Chandler, J.A.D. Wilcox, P. Bettess. A model for the thermal performance of thick composite laminates in hydrocarbon fires. *Revue De L'institut Francais Du Petrole*. 1995; 50: 69-74.
- [124] M.R.E. Looyeh, P. Bettess, A.G. Gibson. A one-dimensional finite element simulation for the fire-performance of GRP panels for offshore structures. *International Journal of Numerical Methods for Heat & Fluid Flow*. 1997; 7: 609-625.

- [125] M.R.E. Looyeh, P. Bettess. A finite element model for the fire-performance of GRP panels including variable thermal properties. *Finite Elements in Analysis and Design*. 1998; 30: 313-324.
- [126] P. Krysl, W.T. Ramroth, L.K. Stewart, R.J. Asaro. Finite element modeling of fibre reinforced polymer sandwich panels exposed to heat. *International Journal for Numerical Methods in Engineering*. 2004; 61: 49-68.
- [127] B.Y. Lattimer, J. Ouellette. Properties of composite materials for thermal analysis involving fires. *Composites Part A; applied science and manufacturing*. 2006; 37: 1068-1081.
- [128] J. Lua, J.O' Brien, C.T. Key, Y. Wu, B.Y. Lattimer. A temperature and mass dependent thermal model for fire response prediction of marine composites. *Composites Part A: applied science and manufacturing*. 2006; 37: 1024-1039.
- [129] J.E.J. Staggs. Heat and mass transport in developing chars. *Polymer Degradation and Stability*. 2003; 82: 297-307.
- [130] C.E. Anderson, D.K. Wauters. A Thermodynamic Heat Transfer Model for Intumescent Systems. *International Journal of Engineering Science*. 1984; 22: 881-889.
- [131] A. Bhargava, G.J. Griffin. A two dimensional model of heat transfer across a fire retardant epoxy coating subjected to an impinging flame. *Journal of Fire Sciences*. 1999; 17:188-208.
- [132] Y.C. Shih, F.B. Cheung, J.H. Koo. Theoretical Modeling of Intumescent Fire-retardant

- Materials. *Journal of Fire Sciences*. 1998; 16: 46-71.
- [133] G.J. Griffin. The modeling of heat transfer across intumescent polymer coatings. *Journal of Fire Sciences*. 2009; 28: 247-277.
- [134] S. Feih, A.P. Mouritz, Z. Mathys, A.G. Gibson. Fire Structural Modeling of Polymer composites with passive thermal barrier. *Journal of Fire Science*. 2010; 28: 141-160.
- [135] R.J. Asaro, B. Lattimer, C. Mealy, G. Steele. Thermo-physical performance of a fire protective coating for naval ship structures. *Composites: Part A*. 2009; 40: 11-18.
- [136] A. Kandare, G.J. Griffin, S. Feih, A.G. Gibson, B.Y. Lattimer, A.P. Mouritz. Fire structural modeling of fibre-polymer laminates protected with an intumescent coating. *Composites: Part A*. doi: 10.1016/j.compositesa.2011.05.012.
- [137] T.W. Goodrich, B.Y. Lattimer. Fire decomposition effects on sandwich composite materials. *Composites: Part A*. doi:10.1016/j.compositesa.2011.03.007.
- [138] J.L. Jurs. Development and testing of flame retardant additives and polymers. FAA report. Springfield, Virginia. 2007; 5-6.
- [139] Q. Wu, W. Zhu, C. Zhang, Z. Liang, B. Wang. Study of fire retardant behavior of carbon nanotube membranes and carbon nanofiber paper in carbon fiber reinforced epoxy composites. *Carbon*. 2010; 48: 1799-1860.
- [140] B. Scharrel, T.R. Hull. Development of fire-retarded materials-Interpretation of cone calorimeter data. *Fire and Materials*. 2007; 31: 327-354.
- [141] A.E. Elmughrabi, M. Robinson, A.G. Gibson. Effect of stress on the fire reaction

- properties of polymer composite laminates. *Polymer Degradation and Stability*. 2008; 93: 1877-1883.
- [142] L.T. Drzal, H. Fukushima, I. Do. Exfoliated graphite nano platelets (xGnP): A carbon nanotube alternative for modifying the properties of polymers and composites. *XG Sciences*. 2006.
- [143] J.W. Gilman, R.H. Harris Jr, J.R. Shields, T. Kashiwagi, A.B. Morgan. A study of the flammability reduction mechanism of polystyrene-layered silicate nanocomposites: layered silicate reinforced carbonaceous char. *Polymers for Advanced Technologies*. 2006; 17: 263-271.
- [144] J.W. Gilman. Flammability and thermal stability studies of polymer layered-silicate (clay) nanocomposites. *Applied Clay Science*. 1999; 15: 31-49.
- [145] S. Bourbigot, S. Duquesne. Intumescence and nanocomposites: a novel route for flame-retarding polymeric materials. In: *Flame Retardant Polymer Nanocomposites*, edited by A.B. Morgan & C.A. Wilkie. John Wiley & Sons, Inc: NJ. 2007; 131-157.
- [146] J. Zhu, F. Uhl, C.A. Wilkie. Recent studies on thermal stability and flame retardancy of polystyrene-nanocomposites. In: *Fire and Polymers: Materials and Solutions for Hazard Prevention*, edited by G.L. Nelson & C.A. Wilkie. American Chemical Society. Washington DC. 2001; 24-33.
- [147] T. Kashiwagi, F. Du, J.F. Douglas, K.I. Winey, R.H. Harris Jr, J.H. Shields. Nanoparticle networks reduce the flammability of polymer nanocomposites. *Nature*

- Materials. 2005; 4: 928-933.
- [148] ASTM D790-10 Standard test methods for flexural properties of unreinforced and reinforced plastics and electrical insulating materials.
- [149] A.B. Morgan, C.A. Wilkie. Flame retardant polymer nanocomposites. Wiley-Interscience. Hoboken. 2007.
- [150] Y. Tang, J. Zhuge, J. Lawrence, J. Mckee, J. Gou, C. Ibeh, Y. Hu. Flame retardancy of carbon nanofiber/intumescent hybrid paper based fiber reinforced polymer composites. Polymer Degradation and Stability. 2011; 5: 760-770.
- [151] B.Y. Lattimer, J. Ouellette, J.T relles. Measuring properties for material decomposition modeling. Fire and Materials. 2011; 35: 1-17.
- [152] J.M. Ferreira, O.A. Z.Errajhi, M.O.W. Richardson. Thermogravimetric analysis of aluminized E-glass fibre reinforced unsaturated polyester composites. Polymer Testing. 2006; 25(8):1091-1094.
- [153] A.B. Morgan, W.D. Liu. Flammability of thermoplastic carbon nanofiber nanocomposites. Fire and Materials. 2011; 35: 43-60.
- [154] E. Kandare, A.K. Chukwunonso, B.K. Kandola. The effect of fire-retardant additives and a surface insulative fabric on fire performance and mechanical property retention of polyester composites. Fire and Materials. 2011; 35: 143-155.
- [155] Y.A. Cengel. Heat Transfer: a practical approach. 2nd Ed. McGraw. New York. 2003.
- [156] J.E.J. Staggs. Modeling thermal degradation of polymers using single-step first-order

- kinetics. *Fire and Safety Journal*. 1999; 32: 17-34
- [157] G.L. Nelson, C.A. Wilkie. *Fire Retardancy in 2001*. In *Fire and Polymer: Materials and Solutions for Hazard Prevent*. Edited by Nelson GL, Wilkie CA. ACS. 2001.
- [158] P.T. Summers. *Predicting Compression Failure of Fiber-reinforced Polymer Laminates during Fire*. Masters Thesis. Virginia Tech. 2010.
- [159] J.B. Henderson, T.E. Wiecek. A mathematical model to predict the thermal response of decomposing, expanding polymer composites. *Journal of Composite Materials*. 1987; 21: 373-393.
- [160] W.A. de Heer, W.S. Bacsá, A. Chatelain, T. Gerfin, R.H. Baker, L. Forro, D. Ugarte. *Aligned Nanotube Films: Production and Optical and Electronic Properties*. *Science*. 1995; 269: 845.
- [161] D.A. Walters, M.J. Casavant, X.C. Qin, C.B. Huffman, P.J. Boul, L.M. Ericson, E.H. Haroz, M.J.O' Connell, K. Smith, D.T. Colbert, R.E. Smalley. In-plane-aligned membranes of carbon nanotubes. *Chemical Physics Letter*. 2001; 338: 14.
- [162] Z.F. Ren, Z.P. Huang, D.Z. Wang, J.G. Wen, J.W. Xu, J.H. Wang, L.E. Calvet, J. Chen, J.F. Klemic, M.A. Reed. Growth of a single free standing multiwall carbon nanotube on each nanonickel dot. *Applied Physics Letter*. 1999; 75: 1086.
- [163] H. Cui, O. Zhou, W. Zhu, B.R. Stoner. Deposition of aligned bamboo-like carbon nanotubes via microwave plasma enhanced chemical vapor deposition. *Journal of Applied Physics*. 2000; 88: 6072.

- [164] W.Z. Li, S.S. Xie, L.X. Qian, B.H. Chang, B.S. Zhou, W.Y. Zhou, R.A. Zhao, G. Wang. Large-Scale Synthesis of Aligned Carbon Nanotubes. *Science*. 1996; 272: 1701.
- [165] R.P. Schlittler, J.W. Seo, J.K. Gimzewski, C. Durkan, M.S. M.Saifullan, M.E. Welland. Single Crystals of Single-Walled Carbon Nanotubes Formed by Self-Assembly. *Science*. 2001; 292: 1136.
- [166] H. Yanagi, E. Sawada, A. Manivannan, L. Nagahara. Self-orientation of short single-walled carbon nanotubes deposited on graphite. *Applied Physics Letter*. 2001; 78: 1355.
- [167] P.M. Ajayan, O. Stephen, C. Colliex, D. Trauth. Aligned Carbon Nanotube Arrays Formed by Cutting a Polymer Resin—Nanotube Composite. *Science*. 1994; 265:1212.
- [168] B. Vigolo, A. Penicaud, C. Coulon, C. Sauder, R. Pailler, C. Journet, P. Bernier, P. Poulin. Macroscopic Fibers and Ribbons of Oriented Carbon Nanotubes. *Science*. 2000; 290: 1331.
- [169] T. Kimura, H. Ago, M. Tobita, S. Ohshima, M. Kyotani, M. Yumura. Polymer Composites of Carbon Nanotubes Aligned by a Magnetic Field. *Advanced Materials*. 2002; 62: 1380.
- [170] Y. Dror, W. Salalha, R.L. Khalfin, Y. Cohen, A.L. Yarin, E. Zussman. Carbon Nanotubes Embedded in Oriented Polymer Nanofibers by Electrospinning. *Langmuir*. 2003; 19: 7012.
- [171] M.D. Lynch, D.L. Patrick. Organizing Carbon Nanotubes with Liquid Crystals. *Nano Letters*. 2002; 2: 1197.